THE UNIVERSITY OF
MELBOURNE

Structure of Dark Matter in Galaxies

Cathryn Margaret Trott

Submitted in total fulfilment of the requirements
of the degree of Doctor of Philosophy

December 2004

School of Physics
The University of Melbourne

Abstract

In all things of nature there is something of the marvellous.
Aristotle

The origin, nature and distribution of dark matter in the universe form some of the biggest questions in modern astrophysics. Dark matter is distributed on a wide range of scales in the universe. This thesis concentrates on galactic scales, attempting to lower the veil and probe the structure of dark matter in galaxies.

The mass distribution of the lensing galaxy 2237+0305 is studied and a combination of photometric, lensing and kinematic data used to constrain the contribution of the luminous and dark mass components to the system. The galaxy is best-fitted with a softened isothermal-like halo (inner logarithmic slope $\sim$0, outer slope $\sim$–2.5), and a sub-maximal disk. The kinematic model requires further improvement for this result to be rigorous, however the density profiles produced in N-body simulations are not preferred over a halo with a constant density core ($r_c \sim 1$ kpc). The results suggest that the combination of lensing, kinematic and photometric data provides the strongest constraints on the distribution of dark matter in galaxies.

Subhalos of dark matter, orbiting within the potential of our Galaxy, will interact gravitationally with the stars in the disk if they pass within their region of influence. Subhalos can be detected by signatures in the phase-space distribution of the stellar disk. Such signatures and their magnitudes are calculated for subhalos with mass and distribution expected from N-body simulations. The capabilities of the ESA satellite GAIA are used as

the potential detection thresholds. Uncertainties in the distances to stars combined with the expected steep mass function of dark matter subhalos and the rareness of their passage through the stellar disk, make their detection unlikely with the GAIA satellite.

The statistical mechanics of self-gravitating systems provide interesting insights into their behaviour. A spherically symmetric, static dark matter halo is studied using a statistical mechanical approach. The gravitational potential is artificially softened to mimic the conditions under which N-body simulations are performed, and the behaviour of the system compared with that for a purely gravitational potential. The system exhibits a low temperature phase, not accessible with pure gravity, which exists at energies probed by many simulations. Consequently, there is no obvious reason to expect agreement between simulated and observed profiles unless the gravitational potential is appreciably softened in nature.

Declaration

This is to certify that
(i) the thesis comprises only my original work towards the PhD except where indicated in the Preface,
(ii) due acknowledgement has been made in the text to all other material used,
(iii) the thesis is less than 100,000 words in length, exclusive of tables, maps, bibliographies and appendices.

Cathryn Margaret Trott

Preface

Sections of two chapters have been published in refereed journals:

- The original work on the mass distribution of 2237+0305, presented as part of Chapter 2, was published in the Monthly Notices of the Royal Astronomical Society as, Trott, C.M., Webster, R.L., 2002, *MNRAS*, 621, 334;
- The work in Chapter 6 has been published in the Astrophysical Journal as Trott, C.M., Melatos, A., 2005, *ApJ*, 618, 38.

Except where explicitly mentioned in the text, this thesis comprises my own work.

Acknowledgements

Without friends no one would choose
to live, though he had all other goods.
Aristotle

Thank-you to Rachel Webster for her ten years of mentoring and her attitude toward sending her students overseas. The many conferences, observatories and institutions I was able to visit because of her generosity have allowed me to experience many aspects of the field of astronomy and meet many amazing people that just doing a PhD can't provide. Thanks also to Andrew Melatos for his supervision, his excitement for doing real physics research and his physical knowledge and understanding, some of which I was privileged to gain. Thanks also to Eric Agol for taking me as a visiting student at UW, and Tommaso Treu and Leon Koopmans for sharing their Keck data with me! For data reduction help, to Martin Zwaan for painstakingly teaching me AIPS and helping me flag my 420 baselines of data.

Thank-you to my fellow Physics students for all of their help and friendship. In particular, to Jamie for his computer and LaTex help, Emma, Arna and Kathie for being great office-mates and for many room 306 gossip sessions, and Meryl for her good humour and eccentricities. Also, to James, Gaby and Vic for the many morning coffees, camping, film nights, Catan and for being such great friends and amazing people. You are all very special.

During my time in Seattle, I met a lot of great people who made my time there fantastic. In particular, I'd like to thank Vandana Desai, Nicole Eichinger, Mark Haggerty, Mark Claire, Amy Kimball, John Bochanski,

Greg Stinson, Julianne Dalcanton, Andrew West and Fabio Governato for their friendship and willingness to share their lives and country with me.

This journey would not have been possible without my family, who have been very tolerant and extremely supportive of my ambitions for as long as I can remember, and I appreciate everything they have taught and given me. From very young they introduced us to the beauty and wonder of Nature and sparked my love of knowledge, learning and the universe.

A big thanks to the great caffeine god for providing mental stimulation, and to the great people who visited the coffee temples with me over the years.

Finally, to my husband Ran, who has given me more than words can describe (as well as being my resident guru on everything lensing). Your belief in me, support and companionship have made these last five years the best of my life.

Contents

List of Figures

List of Tables

CHAPTER 1

Dark Matter in Galaxies and Gravitational Lensing

Something unknown is doing we don't know what.
Sir Arthur Eddington

The universe we observe is dominated by gravitationally bound nebulous structures of stars and gas — galaxies. The name is derived from the Greek word *galactos*, and refers to the ethereal milkiness of the ribbon of light from our own Galaxy, observed by early astronomers.

In modern astrophysics, we now understand many aspects of the formation, evolution and structure of galaxies, but many pieces of knowledge are still required to put together a complete picture. This thesis aims to elucidate some of these pieces.

The commonly accepted view of structure formation in the universe (the cold dark matter paradigm) holds that in the early universe, Gaussian fluctuations of *dark matter*, the primordial substance (collisionless elementary particles created in the early universe) that forms the basis of the galaxies observed today, were distributed according to an initial power spectrum. As the universe expanded and cooled, dark matter overdensities self-gravitated and collapsed, producing increasingly deeper potential wells for baryons to subsequently fall into. The baryons in the early universe formed out of the cooling radiation from the Big Bang. After $z \sim 1000$, the thermal equilibrium between particles and radiation was lost (the surface of last scattering of photons, now observed as the CMB) and the universe was dark and neu-

tral. Primordial hydrogen fell into potential wells and cooled dissipatively to form the first bound baryonic objects. These objects, whether Population III stars or quasars (accretion disks around black holes), are likely those that first reionised the neutral universe ($z \sim 7$–15).

Baryons cool dissipatively in dark matter potentials through hydrogen line and thermal emission, and clouds of hydrogen coalesce and fragment until their densities can ignite nuclear burning, and form stars. The properties of galaxies observed in the universe today therefore reflect the physics of the early universe.

1.1 The structure of galaxies

Galaxies are observed to have many different shapes and forms (morphological type). Until recently, the evolutionary or other connections between these types have been the matter of much speculation. Images to redshifts approaching that of the dark ages ($6 \lesssim z \lesssim 1000$) with the Hubble Space Telescope (HST), have provided insight into the processes of galaxy formation and evolution. Disk instabilities producing bar structures (Toomre 1977; Sellwood 1981), and galaxy interactions and mergers forming early-type from late-type progenitors (see review by Barnes and Hernquist 1992), are examples of the ways structures can evolve in time.

One of the most enigmatic aspects of galaxies are the dark matter halos the stars and gas are thought to lie within. Dark matter is the dominant gravitational component to the galaxy (kinematic observations show the dark matter to not only contain 90 per cent of the mass of the galaxy, but also to spatially extend up to an order of magnitude further than the stellar disk), but since it is cold (negligible primordial velocity dispersion) and collisionless, it provides no thermal heating to the structure [it can provide dynamical heating however, if it is clumped (see Chapter 5)]. In addition, it has a negligible cross-section to electromagnetic interaction, making it impossible to detect directly (Weakly Interacting Massive Particles, WIMPS, such as the neutralino may self-annihilate to produce gamma rays and this could be used as a direct measure in sufficiently high density regions). Dark matter is therefore a substance that enters the physics of galaxies through gravity. This study exploits this feature, investigating dark matter properties in galaxies through i) gravitational lensing, which probes mass, not

light — dark matter can be studied via its presence rather than requiring its detection, ii) dynamical effects on luminous particles — using the phase-space positions of stars in the Galaxy to infer the presence of dark matter, and, iii) a statistical mechanical analysis of an equilibrium self-gravitating structure.

At the most basic level, a late-type galaxy is comprised of a dark matter halo, a thin ($\sim$ 100–500 pc) stellar disk of younger, bluer stars with some ongoing star formation, a spheroidal bulge component of older, redder stars, and a component of both neutral (e.g. HI, CO) and ionised (e.g. HII, photoionised by stars) gas. In addition, there is often a thick disk of old stars extending kiloparsecs from the thin disk midplane, and instability features such as bars and spiral arms in the thin disk. Early-type galaxies are basically the same as late-types, but with the spheroidal component dominating the disk (also they rarely have much gas). Unlike late-types, which are predominantly rotationally supported, early-type galaxies are mostly pressure supported by a quasi-isotropic stellar distribution.

There have been many papers in recent years discussing the matter distribution in galaxies and, in particular, the relative contributions of the stellar disk and dark matter halo. Any attempt to model the structure of a galaxy with multiple components is limited by the information provided by the light we receive. This introduces degeneracies in the mass distribution when we compare the few constrained parameters with the large number of unknowns.

In particular, the kinematic and photometric information that can be obtained about a galaxy cannot provide all of the data required to uniquely solve for the mass distribution. Besides having to assume that mass follows light (kinematics and light curves trace different properties, and mass-to-light ratios are not well constrained), the lack of knowledge of the mass and structure of the dark matter halo requires that an assumption about this be made. In general, the mass-to-light ratio of the disk component in a rotation curve can be increased and the dark matter contribution decreased, to match the same observed curve. Breaking this degeneracy requires extra information about the system.

One technique that has been used to side-step this problem is to assume a maximal disk (quantified in Sackett 1997), whereby the disk contributes the majority of the rotation (75–95%) at the radius of its maximum circu-

lar speed. This definition takes into account the contribution to the inner rotation curve of a bulge component. Various studies have challenged and supported this view and they will be discussed in Section 2.4.3.

1.2 Dark matter in galaxies

Observations of rotation curves of galaxies gave the first hints of the existence of dark matter. In the 1960s and 70s, extensive studies of the circular rotation of spiral galaxies suggested the need for dark matter to account for the missing dynamical mass (e.g. see Rubin et al. 1962, 1978; Faber and Gallagher 1979). The flatness of rotation curves beyond the optical edge of these spirals contradicted the expected Keplerian fall-off. In the 1980s and 90s, many groups used the distribution of structure in the universe to deduce the expected properties of dark matter particles and applied these to N-body simulations (Peebles 1984; Navarro et al. 1996). The subsequent calculated profiles can be compared with the results of observations for consistency.

The firm determination of a general trend in the features of rotation curves, as distinct from a few abnormal systems, requires the accumulation of data from many galaxies with varying morphological types. Salucci and Burkert (2000) constructed 'universal rotation curves' (URCs) with luminosity as the only free parameter, from observations of $\sim$1100 rotation curves. From these URCs, they were able to subtract constant mass-to-light ratio disks from the surface brightness distributions of observed galaxies, and derive the expected contribution from dark matter. Salucci (2001) found the dark matter halos were required to have large core regions in order to fit the universal curves. Core radii of 3–4 disk scale lengths were found to be consistent with observations for large spiral galaxies. More recently, de Blok et al. (2001b) used Hα kinematics of low surface brightness galaxies and assumed minimal disks to investigate the density profiles of dark matter halos in these dark matter dominated galaxies. They found inner density slopes consistent with constant density cores.

In the 1980s, numerical N-body simulations of collisionless particles were developed to investigate the structures that would be formed using cosmological initial conditions such as a scale free power spectrum (Efstathiou et al. 1985; Davis et al. 1985; White et al. 1987; Efstathiou et al. 1988). The

cores found in real systems, however, are not consistent with the N-body predictions for the density distribution of halos (Navarro et al. 1996), and so further investigation is warranted. There has yet to be a solution explaining both the simulation results and those from observational studies. Hayashi et al. (2004a) and Hayashi et al. (2004b) propose that the discrepancy may lie in the comparison of real galaxy rotation curves with a spherically averaged, and multiple simulation-run averaged, density profile (i.e. the NFW profile), rather than with the anisotropic output of individual simulations — there is a range of profiles found in simulations that average to the NFW profile. In addition, they use smoothed particle hydrodynamic simulations (SPH) to include gas in a dark matter simulation, and observe the dynamics of the system from different angles, to match to the observations of LSB galaxies. This method is certainly a step in the right direction for the direct application of simulation results — use of the full data rather than an average — however the large number of degrees of freedom in the problem (many different simulations used and different angles to find one that fits) allow a solution to be found easily that may not be physical.

Recent N-body results demonstrate that, at the current resolution of simulations, the central power-law exponent does not converge to a universal value (Navarro et al. 2004) and further investigation is required. It seems, however, that numerical simulations that only model the collisionless component of the galaxy cannot reasonably be compared with a real halo that has been dynamically affected by the presence of baryons. In addition to further improving simulations to include collisional components, careful modelling of real systems is our best avenue for determining the distribution of dark matter in galaxies.

This observational avenue also has its difficulties including the beam smearing effect of low resolution data that causes the rotation to appear slower in the inner regions of a system and therefore flatten the implied density profile (Swaters et al. 2003). Obtaining a large amount of high resolution and complementary data for a system is the most robust way to proceed. Gravitational lensing can provide this additional complementary information.

1.3 Gravitational lensing

Gravitational lensing is a consequence of the curvature of spacetime. This curvature due to the presence of the lens mass is calculated in the first post-Newtonian approximation as an effective refractive index and the bending angle of light (the angle through which the light deviates from its background value due to the integrated deflection due to the mass) calculated using standard optics (Schneider et al. 1992).

In practice, one observes the multiple images produced by a strong lens (where the source is sufficiently close to the optic axis to produce multiple images), and assuming some general mass distribution, calculates the original source position. Since the source is the same for all images, such a process can provide information constraining the mass distribution of the lens (such as the total mass enclosed within a given image radius).

If the simplest case of point masses for both lens and source is assumed, the positions of the images observed in the lens plane can be obtained analytically using simple geometry. This geometry is directly generalisable for more complex mass distributions, where extended lenses comprise multiple components. The lens equation linking these can be written easily,

$$\alpha(\theta) = \theta - \beta, \tag{1.1}$$

where

$$\alpha = \frac{D_{\rm ds}}{D_{\rm s}}\hat{\alpha}, \tag{1.2}$$

is the reduced bending angle, θ is the image position, β is the source position, and all distances are angular diameter distances (Narayan and Bartelmann 1999), which are cosmology dependent. Figure 1.1 shows these diagrammatically.

For a circularly symmetric mass distribution, the bending angle scales as $\alpha{\sim}M(<R)/R$, where R is the projected radius. Hence for an isothermal sphere, where $\rho{\sim}r^{-2}$, the bending angle is constant with radius, producing very different effects to the point mass, where $\alpha{\sim}1/R$. The vector bending angle for a general mass distribution, $\hat{\alpha}$, is given by,

$$\hat{\alpha}(\xi) = \frac{4G}{c^2}\int \frac{(\xi-\xi')\Sigma(\xi')}{|\xi-\xi'|^2}\, d^2\xi', \tag{1.3}$$

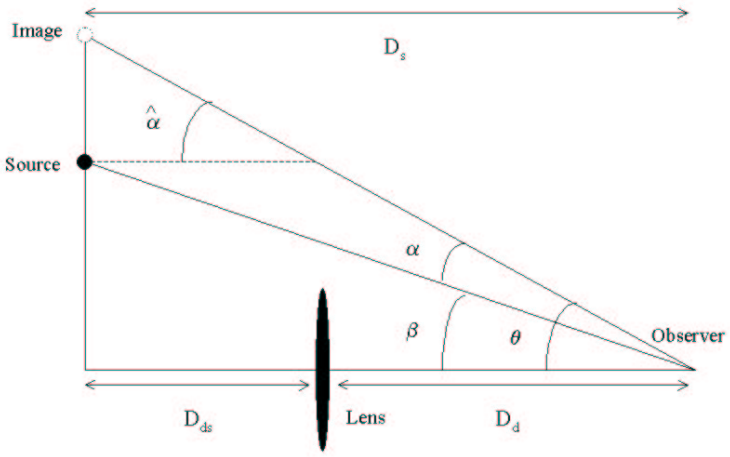

Figure 1.1: Diagram of the important angles involved in strong gravitational lensing. D_s, D_ds and D_d are the angular diameter distances between observer-source, lens-source and observer-lens, respectively. The source is located at angle, β, the image at angle θ and α is the bending angle.

where Σ is the surface mass density and the integral extends over the surface of the distribution (primed co-ordinates). The addition of multiple mass components is trivial with this formalism.

The potential theory of gravitational lensing allows one to characterise the mapping from the source to the image plane via quantities such as the convergence, $\kappa = \Sigma/\Sigma_\mathrm{cr}$, and shear, γ, which quantify the amount of matter and its ellipticity. The lensing potential, ψ, is the angular diameter distance scaled gravitational potential projected onto the plane, and thus represents the potential one should use to calculate light path deviations for a given mass distribution of the lens,

$$\psi(\theta) = \frac{D_\mathrm{ds}}{D_\mathrm{d} D_\mathrm{s}} \frac{2}{c^2} \int \Phi(D_\mathrm{d}\theta, z)\, dz. \tag{1.4}$$

The local area mapping from the source to the lens plane is described by the Jacobian matrix, $\mathcal{A}$, which is a function of the second derivatives of the lensing potential, ψ. (Intuitively, just as the Laplacian of the gravitational potential gives the density, the Laplacian of the lensing potential gives the convergence of the lens, κ, which is the normalised surface mass density). The off-diagonal terms characterise the shape of the lens at orders higher

than the monopole, which describes radial deflection only,

$$\mathcal{A} = \frac{\partial \beta}{\partial \theta} = \left(\delta_{ij} - \frac{\partial^2 \psi(\theta)}{\partial \theta_i \partial \theta_j} \right). \tag{1.5}$$

The shear, γ, is described partly by the off-diagonal terms of the mapping matrix, such that

$$\mathcal{A} = \begin{pmatrix} 1 - \kappa - \gamma_1 & -\gamma_2 \\ -\gamma_2 & 1 - \kappa + \gamma_1 \end{pmatrix}, \tag{1.6}$$

where the subscripts 1 and 2 denote the two orthogonal components of the shear.

Both internal (non-circular lens) and external (influence of other mass along the line-of-sight) shear can be present in a lens system, and they have different characteristics. Internal shear is more likely to produce anisotropic distortions across the different images, whereas external shear can produce an overall distortion across the lens. Shear produces both radial and tangential deflection, and the lower order multipoles, such as the quadrupole, can have significant deflections when compared with that of the monopole, which is purely radial (Kochanek et al. 2004).

Gravitational lensing can occur in both the strong and weak limits. Weak gravitational lensing occurs in low surface density regions (for example, in the outer regions of clusters) where there is insufficient convergence to produce multiple images, but enough to produce statistically identifiable distortion of the wavefront, when many systems are investigated (Tyson et al. 1990; Miralda-Escude 1991). Such analysis is used extensively to determine cosmological parameters, as the amount of distortion clearly depends upon the amount of matter along the line-of-sight (Ω_M, σ_8) and the path length through the matter (Ω_Λ). Strong gravitational lensing occurs through the centres of massive clusters, and for sources closely aligned with the centres of galaxies. In these cases, if the critical surface density for multiple images,

$$\Sigma_{\rm cr} = \frac{c^2}{4\pi G} \frac{D_{\rm s}}{D_{\rm ds} D_{\rm d}}, \tag{1.7}$$

is satisfied somewhere in the lens, multiple images occur (Subramanian and Cowling 1986). Physically, this is because if $\Sigma > \Sigma_{\rm cr}$, $\alpha(\theta) > \theta$, and a light ray can reach the observer from the opposite side of the lens to the source

position. For spherically symmetric systems with density monotonically decreasing from the centre, the central density must exceed this critical value. For elliptical systems, this condition is relaxed since more mass can be contained within a given radius for the same central density.

The distance dependence of gravitational lensing is clear from Equation (1.7). The angular diameter distances shown here are cosmology (e.g. H_0) dependent, suggesting lensing can be used to determine the Hubble constant. This is indeed the case, and this will be discussed later in this chapter. These distances also constrain the redshifts for the lens and source at which one would expect strong lensing to most likely occur. If the lens is too close ($D_{\rm d}$ small), or the lens-source separation too small ($D_{\rm ds}$ small), $\Sigma_{\rm cr}$ will be too large for a galaxy-type mass distribution, and strong lensing will not occur. This is intuitively obvious as a lens cannot focus too close to itself.

The optimum redshifts for the lens and source depend upon these parameters, but also upon the number density of sources as a function of redshift and the cosmology employed. For the currently favoured concordance cosmology ($\Omega_M = 0.27$, $\Omega_\Lambda = 0.73$, Bennett et al. 2003), the angular diameter distance turns over at $z \sim 1.6$, implying that for $z \gtrsim 2$, the ratio, $D_{\rm s}/D_{\rm ds}$ is roughly constant at ∼1.1–2 (for lenses at redshift, z_d ∼0.1–1, Hogg 1999). This would mean that high redshift lenses should be as common as those at $z \sim 2$, however, there are two factors that reduce the number of known high redshift sources to zero — the decrease of apparent magnitude with distance (drops more rapidly with redshift for the concordance model than for an Einstein-de Sitter universe), and drop of number counts of source objects. Most known instances lens a background quasar, mostly because quasars are bright beacons that are more easily detected with magnification than their diffuse host galaxies. Quasar number counts peak at $z \sim 2$, and Wyithe (2004) has recently used the lack of high redshift lenses found in SDSS to constrain the high-redshift quasar luminosity function to be very steep, $dN/dL \sim L^{-3.0}$, for $z \sim 6$, implying that the lensing optical depth to bright quasars is small ($\tau(z_s = 6) = (2.5 \pm 0.25) \times 10^{-3}$ compared with $\tau \sim 0.05$ for all source redshifts and early-type galaxies, Fukugita and Turner 1991).

1.3.1 Magnification

When a source is gravitationally lensed, light ray bundles from it are distorted by gravity. Since surface brightness is conserved for a resolved source (photon number is conserved and specific intensity is constant along photon paths), images are distorted into larger or smaller areas. This ratio of image-to-source solid angle is the magnification of the source. When the source is unresolved, such as for a quasar, there will be a brightening or dimming in each image produced. Since magnification is the ratio of two areas, it follows that the magnification matrix is closely related to the Jacobian of the mapping. It turns out that,

$$\mu = det\mathcal{M} = \frac{1}{det\mathcal{A}}, \tag{1.8}$$

is the magnification of a given image, where $\mathcal{M}$ is the magnification matrix. The flux ratio, or magnification ratio, of two images provide an observational constraint on the mass distribution of the system.

1.3.2 Time delays

Another observational effect of gravitational lensing is the delay in the arrival of photons between different images. The size of this delay depends on the path difference, and has two components: a geometrical delay and a gravitational delay. The time delay for a lens system can be calculated, based upon a given mass model and cosmology (angular diameter distances depend sensitively on Ω_0 and Λ), and compared with the observed delay. In this sense, the time delay is a further constraint on the mass distribution of the lens system.

Photons will take a path which extremises the Fermat Potential, according to Fermat's Principle. This potential is a combination of the geometrical path length difference and the extra path length experienced when traversing a gravitational potential. It is not surprising the potential is another way of writing the lens equation. This time delay function is given by,

$$t(\theta) = \frac{1+z_d}{c}\frac{D_\mathrm{d}D_\mathrm{s}}{D_\mathrm{ds}}\left[\frac{1}{2}(\theta-\beta)^2 - \psi(\theta)\right], \tag{1.9}$$

where the geometrical delay is contained in the first term in parentheses, and the gravitational delay in the second term. Since $D_\mathrm{d} \propto H_0$, hence $t \propto H_0$,

and time delay measurements combined with lens models can be used to determine the Hubble constant (e.g., Treu and Koopmans 2002; Chartas et al. 2002).

1.3.3 Mass-sheet degeneracy

The combination of image positions, flux ratios and time delays appears to place a lot of constraints on the mass distribution of a lensing system. There are, however, other effects that can make determining the mass distribution difficult. One is the mass-sheet degeneracy.

This degeneracy concerns quasi-constant density sheets lying along the line-of-sight which increase convergence but otherwise leave the images unchanged. Consider a small, constant change to the convergence, $\kappa \rightarrow (1 - \lambda) + \lambda\kappa$, $\lambda \sim 1$. Calculations performed with the lens equation produce a shift in the source position ($\beta \rightarrow \beta/\lambda$, in one dimension), which is not detectable since the true source position is unknown. Similarly, the magnification of a particular image changes as $\mu \rightarrow \mu\lambda^2$, but since only flux ratios are measurable, the ratio is unchanged.

Detection of this degeneracy is important when one is using lensing to measure the Hubble Constant, H_0, where the value found will scale linearly with the small shift, λ. One way to break this degeneracy is to include kinematic information in the mass calculation, thereby calibrating the mass scale at the image radius (e.g. Koopmans et al. 2003).

1.3.4 Microlensing

In addition to the mass-sheet degeneracy, image magnifications can be individually affected by microlensing. This is lensing by low mass objects, usually stars in the lensing galaxy, that produce multiple images on the microarcsecond scale, some of which have large magnifications. In a system where the images are located in regions of high stellar density (such as 2237+0305, discussed in this thesis), the optical flux ratios do not always reflect the macro-structure of the lens, but rather a superposition of that and the microlensing magnification. The microlensing signal depends on the local optical depth to microlenses, their velocity relative to the image positions and the angular diameter distances $D_{\rm d}$, $D_{\rm s}$ and $D_{\rm ds}$ (if the characteristic separation between caustics is too high relative to the source size,

the effect will be washed out).

In regions with high microlens optical depth, a solution to this problem is to measure flux ratios in a waveband where the source size exceeds the characteristic caustic separation. This often corresponds to longer wavelengths where the quasar emission region is large ($> 10^{17}$cm in the mid-IR for 2237+0305 at 90 per cent confidence, Wyithe 2004).

1.3.5 Using lensing in galaxies

At the most basic level, gravitational lensing can provide additional information to constrain the mass distribution in a galaxy. Galaxies studied without lensing information suffer from being under-constrained systems. Photometric combined with kinematic information can only provide partial information, since the amount of mass contributed by the observed light (the mass-to-light ratio) is unknown. Without a dark matter halo, the kinematics would directly probe the luminous mass components, and the rotation curve could be decomposed correctly. With a dark matter halo, whose density profile is unknown, the rotation curve cannot be uniquely decomposed. Therefore, a disk-halo degeneracy exists. This is often broken by assuming a 'maximal disk', as mentioned earlier, whereby the disk has the maximum mass possible to fit the rotation curve. There are arguments for and against this approach, but maximality is, nonetheless, an assumption.

Such difficulties can be overcome using gravitational lensing, for a number of reasons. Firstly, and most simply, it provides additional constraints to be placed on the mass model for the system. More importantly, the constraints are different to those provided by kinematics. The mass probed is a projected mass, not spherical, which provides useful information about the structure in the outer regions. The image locations are based upon the total gravitational potential, and therefore are not confused by kinematics.

The amount of extra information is most pronounced in systems where there are extended lensed images. Such systems provide flux information in all independent pixels covering the lens where the image resides. In contrast, point sources provide information at only a few (usually 2–4) positions. This thesis will only deal with point source images. Extended images offer the possibility of characterising the mass distribution of the lens and the source distribution in a more unconstrained way since more information is available and fewer assumptions need to be made. In the absence of kinematic infor-

mation, point source lenses can only provide information about the surface mass density in the image region, as well as the overall structure of the lens at the image radius.

Gravitational lensing has been used recently by Maller et al. (2000) to disassemble a galaxy into its dark and luminous mass components. Their analysis of the doubly imaged system B1600+434 did not have a unique solution for the mass distribution in the system due to the necessity of invoking the Tully–Fisher relation (Tully and Fisher 1977) for rotational information (rotation was assumed rather than measured), the large errors on the position angle of the major components and the perturbing effect of a nearby galaxy. In addition, the constraint of only two images limits the number of known parameters. Their work, however, illustrated the utilisation of lensing to break the disk/halo degeneracy. They found a high probability for a sub-maximal disk, and the need for a constant density core in the centre of the dark matter halo. These results pave the way for the work presented in this thesis as they demonstrate the ability to solve for the mass distribution given a reasonable number of known parameters.

1.4 Thesis outline

This thesis explores aspects of the dark matter population in galaxies, using a range of techniques.

Chapters 2, 3 and 4 discuss the distribution of matter in the lensing galaxy 2237+0305. They include the use of gravitational lensing information combined with photometric and kinematic properties to investigate the importance of each mass component, luminous and dark, to the structure of the galaxy. Additional high resolution kinematic information from the Keck telescope is analysed to improve the results significantly. The final component to this analysis uses this information to constrain both the mass structure and kinematic model of the galaxy.

Chapter 5 then explores the effects of local dark matter by considering the dynamical effects on stars in our own Galaxy through the interaction with dark matter clumps passing through the Galactic disk. Calculations are undertaken to determine whether the GAIA satellite could detect these observational signatures. Observational limits on the mass function of dark matter halos will provide stringent limits on current theories of CDM.

Chapter 6 takes a theoretical approach to the distribution of dark matter in galaxies by considering the problem from a statistical mechanical viewpoint. Following on from previous work in this field, the thermodynamic characteristics of a self-gravitating system are applied to the results of N-body simulations, which predict the density profiles of halos. Results from simulations are shown to depend on the necessary, but artificial, numerical constraints used in simulations. Most importantly, the use of a softened potential for gravity in simulations leads to an additional phase in collisionless simulations becoming accessible, that is not accessible in true gravity.

Chapter 7 concludes the thesis and offers suggestions for future work.

Throughout, we have assumed an Einstein-de Sitter universe with a Hubble constant of $H_0 = 70$ kms^{-1}Mpc^{-1}. This produces a 2 per cent change in the combination $D_{\rm ds}/D_{\rm s}$ compared with a concordance cosmology ($\Omega_M = 0.3, \Omega_\Lambda = 0.7$) for 2237+0305, and therefore does not strongly affect the bending angles.

CHAPTER 2

2237+0305: Introduction

The galaxy 2237+0305, which gravitationally lenses a background quasar into four images, is introduced and previous published studies of its mass distribution reviewed. A comprehensive mass model is developed and galactic properties such as mass-to-light ratios determined, based upon the best-fitting solution to a combination of lensing and photometric data. It is found that a high quality rotation curve is required to break the remaining degeneracies in the system, and to determine the relative contribution of the disk, bulge and dark matter halo to the support of the galaxy and lensing of the system. Efforts to measure a rotation curve in both the optical and radio are presented. A full rotation curve for this system would allow the most comprehensive analysis of the mass distribution of any lens galaxy.

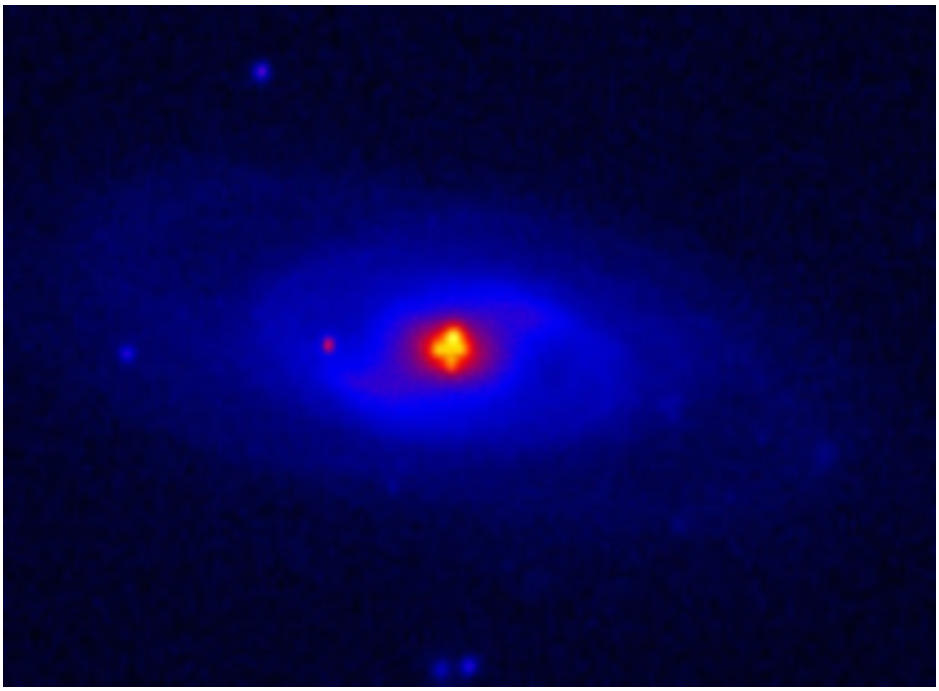

Figure 2.1: 15 second false colour image of 2237+0305 (taken with the Gemini acquisition camera, Randall Wayth, priv. comm.). The four centrally located images are barely resolved as yellow points. The red region is the centre of the bulge and the bar is observed at a different position angle to the disk, with its outer regions joining the spiral arms. This image is $\sim 1'$ across corresponding to $\sim$45 kpc at the galaxy redshift.

2.1 2237+0305: A barred spiral galaxy

2237+0305, a barred spiral Sab type galaxy at a redshift of z=0.0394 was first discovered by Huchra et al. (1985), but the lensed images were first seen by Yee (1988). Almost collinear with the centre of the galaxy (the optic axis) is a background quasar at z=1.695. The geometric conditions of this system are favourable to macrolensing of the quasar through the bulge of the galaxy.

Huchra's lens, as it is often termed, has been studied extensively over the past fifteen years, mainly due to its proximity to us, and the ability to image the galaxy with ground-based telescopes. For this reason, it is the ideal laboratory in which to study lensing and, more importantly for this work, the structure of the lensing galaxy.

Galaxy 2237+0305 is improbably close to the line-of-sight to the source (probability of occurrence $\sim 10^{-4}$, Schneider et al. 1988). The four, almost symmetric images of the background quasar straddle the central nucleus, placing constraints on the structure of the inner-most regions of the galaxy. Traditionally, it has been difficult to obtain information in these regions of any galaxy due to the degeneracy introduced by multiple mass components and smearing of spectroscopic data from non-circular stellar and gas motions. Lying at low redshift, the lens galaxy displays a visibly extended spiral disk, allowing a detailed investigation of its mass distribution beyond the lensing regions. In addition, two points on the rotation curve have been obtained from neutral hydrogen observations (Barnes et al. 1999). The combination of its proximity and its improbable alignment with the background quasar makes this system the ideal laboratory for studying galactic structure.

In addition, since the quasar images are observed through the high stellar density bulge of the galaxy, microlensing of the quasar by bulge stars may be observed. Such measurements have been used to infer that the optical emission region of the quasar is smaller than the characteristic size of the region of high magnification of a bulge star caustic ($< 2\times10^{15}$cm, Wambsganss et al. 1990). More recently, the mid-IR flux ratios and their lack of microlensing contamination have been used to constrain the size of the mid-IR emission region (Wyithe et al. 2002). Wayth et al. (2004a) use highly resolved IFU data of the galactic centre to measure flux ratios for the broad emission lines, CIII] and MgII and nearby continuum wavelengths, between the images. Assuming a macro-lens model for the system, the difference between the magnifications of the line and continuum images can be used to constrain the size of the broad-line region ($\sim$0.1pc). These measurements are critical for constructing a model for the structure of QSOs.

The lens has a visible central bulge, a stellar disk and a perturbing bar. The four images straddle the nucleus in an Einstein Cross configuration and their positions have been measured accurately (Crane et al. 1991). The major axis of the disk and bulge have been measured by Yee at a position angle of 77° (East from North), and the images at an angle of 67°. The rotation of the images away from the major axis of the galaxy is due to the torqueing effect of the bar at a position angle of 39°. Schmidt et al. (1998) modelled the mass distribution in the bar and its effect on the positions of

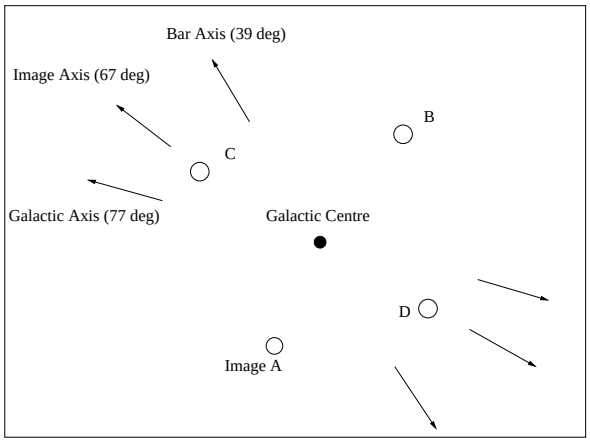

Figure 2.2: Locations of the four lensed images as measured by Crane et al. (1991) and the major axes of the principal galactic components as measured by Yee (1988).

the images. The angular positions of the major components of the galaxy are displayed in Figure 2.2.

The scale lengths of the luminous components of the galaxy have been measured from HST light profiles by Schmidt (1996), and their ellipticities by Racine (1991) and Irwin et al. (1989), and thus many of the galactic parameters have been measured previously.

Qualitatively, the majority of the convergence will be provided by the central bulge (in the absence of a cuspy dark matter halo) as it dominates in the region of strong lensing. The disk will contribute both globally and add significant convergence to the inner regions. The bar will add little convergence for the lensing, but will provide shear through its rotated position angle. In addition, the inclination of the disk and flattening of the bulge will also contribute to the twisting of the image positions. The presence of a dark matter component to the galaxy will add convergence and, if non-spherical, shear. Given the highly elliptical nature of the visible components already discussed, the halo will initially be assumed to be spherical, since the other components can account for any internal quadrupole.

In this work a mass model for the galaxy 2237+0305 will be constructed

based upon a combination of lensing and photometric information. Section 2.2 reviews previous work undertaken on this galaxy. Section 2.3 then presents the parametric mass models used in the study and discusses their applicability. The results are then presented in Section 2.4, including the best-fitting source position, rotation curve and mass-to-light ratios. An improved method is then discussed in Section 2.5, and the implications for the structure of the dark matter halo presented in Section 2.6. Attempts to measure kinematic information for the galaxy are described in Section 2.7 and then conclusions drawn in Section 2.8.

2.2 Constraints and previous work

High resolution imaging and detailed modelling of Huchra's Lens has provided us with many of the model parameters required for fitting a mass distribution. Schmidt (1996) used I-band *HST* imaging to measure the disk and bulge scale lengths, as well as to determine their ellipticities. These results updated values from previous studies by Yee (1988) and Huchra et al. (1985). These data leave the disk and bulge mass-to-light ratios as the only parameters to be fitted for these components. The bar has a measured ellipticity, position angle and major axis, and within uncertainties in the mass-to-light ratio, is completely determined by Schmidt.

Schmidt deconvolved the *HST* light distribution using two different bulge models — an exponential and a de Vaucouleurs surface mass profile. Results from the literature show that one or other of these profiles usually fits a bulge well. Carollo et al. (2001) show from *HST* observations that the form of the bulge mass profile is mildly morphologically dependent. For Sa-Sb galaxies, such as 2237+0305, both types are observed and thus an exploration of both models is prudent.

One further constraint and one check will be applied to the final rotation curve. Neutral hydrogen observations by Barnes et al. (1999) at the VLA provide two rotation points in the outer regions of the galaxy. In these regions, the visible matter has fallen below observational levels and the HI is acting as a tracer of the dark matter distribution. Unfortunately, the data are not of high enough angular resolution to probe the rotation in the inner regions of the galaxy. An additional piece of information is provided by gravitational lensing, where the position of the images in combination with

the geometry of the source-lens-observer system gives the projected mass enclosed within the images (Rix et al. 1992; Wambsganss and Paczynski 1994). The consistency of this value with the mass distribution found will act as a check on the result. The image radius is defined as the average of the radii of the four images from the centre of the galaxy. This corresponds to $r_{\rm im} = 0.9$ arcsec $\equiv 670 h_{70}^{-1}$ parsecs. The shape of the halo is completely unconstrained observationally. Both the scale length and the halo total mass will be fitted.

There are therefore seven parameters for which a fit is required — four mass-to-light ratios, one core radius and two co-ordinates of the source position. As constraints, there are eight co-ordinates of image positions and two rotation points. These observational constraints are given in Table 2.1. Thus, there are three degrees of freedom.

The galaxy has been previously modelled by many groups. Huchra et al. (1985) undertook the initial work on the system, measuring ellipticities and scale lengths and providing a rudimentary lensing analysis by modelling the galaxy with a single circularly symmetric component. Note that their observations did not resolve individual images. They showed that the inferred mass-to-light ratio is within current values for nearby galaxies. Kent and Falco (1988) approximated the galaxy as an oblate spheroid, citing the bulge and the bar as the two primary lensing components. Their analysis attempted to fit the observed quasar fluxes to their model and was reasonably successful, although the fluxes of two of the images were not reproduced. Contemporaneously, Schneider et al. (1988) used a single, elliptical de Vaucouleurs bulge to model the galaxy mass distribution. They fitted two free parameters, the mass-to-light ratio (assumed to be constant) and the source position, given the image positions, by minimising the deviation of predicted positions from those observed. Unfortunately, they were limited by imaging taken with large PSFs and by the simplicity of their modelling. Both Kent and Falco (1988), and (Schneider et al. 1988) find different positions for the background source, as does Schmidt (1996) in his analysis, which included the bar. Schmidt combines the disk and bulge into a single component with the ellipticity Racine (1991) measured for the bulge alone. The bar was then studied in detail using high resolution *HST (WF/PC-1)* I-band imaging and the source position again back-mapped from the measured image positions. This is the first study to include the dark matter halo in the modelling.

Quantity	*Value*	*Source*
Halo		
No constraints		
Bulge		
Position angle	77°	Yee (1988)
Ellipticity (=1−b/a)	0.31	Racine (1991)
dV		
Scale length	4.1±0.4″ (3.1kpc)	Schmidt (1996)
Exp		
Scale length	0.59±0.03″ (0.45kpc)	Schmidt (1996)
Disk		
Position angle	77°	Yee (1988)
Inclin. angle	60°	Irwin et al. (1989)
dV		
Scale length	11.3±1.2″ (8.6kpc)	Schmidt (1996)
Exp		
Scale length	5.6±0.4″ (4.27kpc)	Schmidt (1996)
Bar		
Position angle	39°	Yee (1988)
dV		
Sfc. Brightness	I_0=20.4±0.2	Schmidt (1996)
Ellipticity	0.64	
Exp		
Sfc. Brightness	I_0=19.9±0.2	Schmidt (1996)
Ellipticity	0.89	
Images		
Mass Enclosed	(1.48±0.01) h_{75}^{-1}	WP (1994)
($\times 10^{10} M_\odot$)	= (1.59±0.01) h_{70}^{-1}	
Positions (")	ΔRA ΔDec.	Crane et al. (1991)
Image A	0.093 -0.936	
Image B	0.579 0.737	
Image C	-0.719 0.266	
Image D	0.761 -0.419	
Rotation:v_{circ}		
22 ± 1 kpc	310±15 kms^{-1}	Barnes et al. (1999)
29 ± 1 kpc	295±15 kms^{-1}	

Table 2.1: Assumed values for the mass distributions from previous work. Image positions are relative to the galactic centre, and have positional uncertainties of ±5mas. WP (1994) denotes Wambsganss and Paczynski (1994), and the central I-band magnitudes (I_0) are measured in mag./arcsec^2. **dV** and **Exp** denote models with a de Vaucouleurs and an exponential bulge, respectively.

In order to have a reasonable chance of understanding the complex structure of this lens, and hence its lensing characteristics, one needs to model each component of the lens carefully. With the accumulation of data on this galaxy over the past fifteen years, this is now possible.

2.3 Current mass model

Prior to the measurement of a high-quality optical rotation curve, the most comprehensive models for the mass distribution of 2237+0305 were published in Trott and Webster (2002) and Trott and Webster (2004), the results and models of which are now discussed.

2.3.1 Mass profiles

Models will be constructed for the mass distributions of the bulge, disk, bar and dark matter halo using parameters from previous studies, and map light rays from the measured image positions to the source plane. Varying the contribution of each component will vary the convergence and shear within the images and shift their positions in the source plane once mapped from the lens plane via the lens equation ('back-mapped'). A potential solution is obtained when a particular addition of the four components produces a common source position. Clearly, the four images originate from the same point in the source plane. The actual position of the source quasar is unknown. The position of the centre of the galaxy will be considered fixed given the relatively few degrees of freedom.

Rotation curves for candidate solutions will be produced and compared with neutral hydrogen rotation measurements and the measured mass lying within the images. The combination of both lensing and kinematic constraints increases the number of constrained parameters and consequently reduces the number of unknowns.

The models used for the mass distributions of the four principal galactic components are standard profiles from the literature, tailored to suit this galaxy.

The bulge is modelled as both a modified de Vaucouleurs surface mass distribution (de Vaucouleurs 1948, 1959), where it is assumed the mass follows the light (constant mass-to-light ratio) and an exponential surface mass profile, as in the models of Schmidt (1996). The modification to both allows

the introduction of an ellipticity, e, such that for the de Vaucouleurs profile,

$$\log \Sigma(x,y) = \log \Sigma_0 - 3.33 \left[\left(\frac{x^2 + \frac{y^2}{(1-e)^2}}{r_b} \right)^{\frac{1}{4}} - 1 \right], \tag{2.1}$$

where Σ is the value of the surface mass density at that position, r_b is the characteristic scale length of the bulge, and e is defined by,

$$e = 1 - \frac{b}{a}, \tag{2.2}$$

where a and b are the semi-major and minor axes respectively. The central surface density ($\Sigma_0 \times 10^{3.33}$) is denoted $\Sigma_{\rm bg}$. The exponential profile is modelled simply by introducing the ellipticity (assumed to be a projection effect),

$$\Sigma(x,y) = \Sigma_{\rm bg} e^{-f(x,y)/r_b}, \tag{2.3}$$

$$f(x,y) = \sqrt{x^2 + \frac{y^2}{(1-e)^2}} \tag{2.4}$$

and again $\Sigma_{\rm bg}$ is the central surface mass density.

The disk surface density is modelled with an exponential function. Unlike the bulge which is treated with the ellipticity as measured, the disk is rotated to its measured inclination of i=60°. This involves projecting the volume to a surface mass density by rotating the z-axis and redefining co-ordinates. If the disk is assumed to be uniformly distributed in the z direction, then one can simply write,

$$\rho(x,y,z) \propto e^{-\sqrt{x^2+y^2}/r_d}, \tag{2.5}$$

where the proportionality includes a factor reflecting the thickness of the disk, assumed to be constant, and r_d is the characteristic disk scale length. The more complicated, but often employed, *sech* profile for the disk thickness is not used in this simplistic analysis. Later work with a thin disk shows that the results are not dependent upon this choice. Upon rotation about the x-axis (such that it becomes the major axis of the ellipse) by the inclination angle, i=60°, the surface mass density is the integral through the rotated

axis, z',

$$\Sigma(x',y') = \frac{\Sigma_{\rm dk}}{\Delta z} \int_{z'_{min}}^{z'_{max}} e^{-\sqrt{x'^2+((z'-z'_{min})\sin i+\frac{y'}{\cos i})^2}/r_d}\, dz', \tag{2.6}$$

where the limits of integration bound the original constant disk thickness at the inclination angle (taken as Δz=500pc), the primed co-ordinates represent the new, observed Cartesian system and $\Sigma_{\rm dk}$ denotes the central surface mass density.

The bar has been extensively modelled by Schmidt (1996) and his surface mass distribution and position angle will be used. Schmidt uses a Ferrers model with an ellipticity, e,

$$\Sigma(x,y) = \Sigma_{\rm br}\left(1-\frac{x^2}{a^2}-\frac{y^2}{b^2}\right)^{\lambda}, \tag{2.7}$$

where $\Sigma_{\rm br}$ is the central surface density, λ is the Ferrers exponent, and the (x,y) co-ordinates lie in the rotated frame of the bar. Schmidt finds different exponents, ellipticities and scale lengths depending on the profiles used to fit to the light distribution. For an exponential bulge and disk, he finds λ=2, e=0.89 and b=1.0±0.3 arcsec fit the observations best. For a de Vaucouleurs bulge and exponential disk, he finds λ=0.5, e=0.64 and b=3.1±0.9 arcsec. In this analysis, the central surface density remains a free parameter. Here $\Sigma_{\rm cr}$ is the critical surface density [Equation (1.7)].

The profile of the dark matter halo is controversial. Conventional theories where ΛCDM is the preferred cosmology have been very successful in explaining the observed large scale structure of the universe (e.g. Peebles 1984). Navarro et al. (1996, hereafter NFW) used N-body simulations to derive a density profile for such a cosmology. One feature of the NFW profile is a cuspy central region with $\alpha \sim -1$ where $\rho \sim r^{\alpha}$. This steepens to $\alpha \sim -3$ for $r \gg r_h$, where r_h is the characteristic scale length of the halo. More accurate simulations have pushed the cuspiness at $r \sim 0$ to $\alpha \sim -1.5$ (e.g. Moore et al. 1999b). Recently, higher resolution simulations showed that at the best resolution currently attainable, there is no convergence to a particular power-law inner slope (Navarro et al. 2004), but most simulations lie in the range $[-1.5,-1]$. Observational work by de Blok et al. (2001a) on low surface brightness galaxies has shown the need for a core in the dark

matter halos, using optical rotation curves and fitting minimal disks. LSB galaxies are expected to be dark matter dominated and some studies have attempted to reconcile these results by including the effects of baryons on the distribution of dark matter (Athanassoula 2004; Sellwood 2003; Weinberg and Katz 2002). Other observational studies have found similar results. Bolatto et al. (2002) modelled the mass structure of NGC 4605 using CO and Hα rotation curves and found the inner regions to be shallower than those of CDM simulations ($\rho \sim r^{-0.65}$ for the steepest inner slope). Simon et al. (2003) performed a similar analysis with the dwarf spiral NGC 2976 and found a shallower slope ($\rho \sim r^{-0.17} - r^{-0.01}$).

The amount by which the baryons can disperse the dark matter from the central regions via heating or draw it in via adiabatic cooling is still a matter for debate. The ability of N-body simulations to correctly reproduce the structures of collisionless dark matter has recently also come under scrutiny (e.g. see Trott and Melatos 2005). Simulations employ a softened gravitational potential, for numerical reasons, which may introduce an unphysical phase in which the system can reside.

CDM has been challenged further by the missing satellite (Moore et al. 1999a) and angular momentum problems (Sommer-Larsen and Dolgov 2001, for a recent discussion). The former concerns the small number of satellite galaxies observed in orbit around our Galaxy compared with that predicted by the theory, and the latter refers to the predictions of CDM of too much angular momentum loss to support observed disk galaxies (simulations show that the disk will transfer much more angular momentum to the dark matter halo, and hence be smaller, than observations can accommodate). The angular momentum discrepancy occurs if one assumes that the dark matter particles and baryons have the same angular momentum distribution. If this is not the case, as discussed by Vitvitska et al. (2002) and Primack (2003), and the dissipative processes undergone by the baryons affect the distribution, this problem may be solved. The missing satellite problem can be partially overcome by assuming that many low mass subhalos do not form stars or form so few that they have extremely low surface brightness and are below observational limits (Bullock et al. 2000).

Since there is no general agreement, the model for the dark matter halo

is chosen as a softened isothermal sphere (Kormann et al. 1994),

$$\Sigma(r) = \frac{\sigma_v^2}{2G} \frac{1}{\sqrt{r^2 + r_c^2}}, \tag{2.8}$$

where σ_v is the velocity dispersion and r_c is the core or break radius. There are several reasons for this choice of profile. Firstly, it has one less parameter than an NFW+core profile (no scale length apart from the core length). This is useful given the few degrees of freedom. Secondly, the profile naturally asymptotes to a flat rotation curve for $r \gg r_c$. Finally, recent studies have found that the two models are indistinguishable when the remaining mass components are taken into account — Weiner et al. (2001) modelled NGC 4123 with both profiles and found their shape had a minor effect on the results. In addition to this, the choice of a spherical halo is a simplification in that it precludes the need to introduce another parameter. This choice is partially justified by the ellipticities in the other components. They are adequate to produce the required ellipticity. Furthermore, recent results from Ibata et al. (2001) suggest our Galaxy's dark matter halo is spherical. They used evidence of the tidal stream from the Sagittarius dwarf galaxy to show that the halo potential cannot be flatter than $q < 0.7$ and probably has $q > 0.9$, where q is the axis ratio. Results from collisionless N-body simulations, however, show halos to be triaxial (Katz 1991; Dubinski and Carlberg 1991; Dubinski 1994). More recently, Wayth et al. (2004b) concluded the halo of 0047-2808 was no flatter than $q = 0.85$, based upon a detailed lens mass reconstruction from the optical Einstein ring observed in that system. A spherical halo is therefore an adequate first approximation.

2.4 Results

2.4.1 Source position and rotation curve

The lensing galaxy was constructed as a two-dimensional array of surface mass elements, with an exponential spatial scale. This feature allowed the important central regions to be highly resolved, while keeping the array dimensions computationally tractable. The galaxy was rotated from its position angle to align the x-axis with the galactic major axis, and the image positions rotated to a right-handed co-ordinate system. The four

mass components were constructed and overlaid on the mass array, forming a surface mass distribution for the galaxy. Alterations were made to this array when varying the halo core radius, r_c, or the scale lengths of the bulge and disk. The bending angles for the particular distribution were then calculated.

The bending angles are calculated for particular values of bulge and disk scale length, for a given bulge profile using Equation (1.3). These values for the four components then were summed together varying the mass-to-light ratios of each component. Since the bending angles scale linearly with mass-to-light ratio, variations in the overall scaling parameters can be considered after the angles have been calculated.

Rotation curves were carefully constructed to incorporate the lack of spherical symmetry in the disk and bulge. The functional form for the disk rotation was obtained for an exponential disk from Binney and Tremaine (1987). The de Vaucouleurs bulge was de-projected into an elliptical volume mass density using the profile of Fillmore (1986) and the rotation calculated by equating the centripetal and gravitational accelerations.

The mass measured by Wambsganss and Paczynski (1994) within the images uses the relations of lensing and determines the projected mass in a cylinder bounded by the images and integrated along the line-of-sight. A suitable distribution of mass profiles must satisfy this constraint. The consistency between this mass and a solution that reproduces the correct image positions does not provide a completely independent constraint as the image positions ensure this mass is correct — it only demonstrates the true convergence and shear that has already been accounted for in the source finding program. As such, the consistency of these points provides a check that the source finding program is reconstructing the correct shear and convergence.

The process of deciding which distributions adequately fit all of the constraints reduces to the minimisation of the χ^2 statistic. For a particular set of profiles for the luminous mass components (as given in Table 2.1), a search through five dimensional parameter space (four mass-to-light ratios and one core radius) was performed. For each model providing a suitable mass enclosed within the images, the eight image positions and the two points at the pertinent positions on the rotation curve, were calculated. These were used to calculate the χ^2 statistic and the minimum found. In addition to the variation of the mass profiles [de Vaucouleurs (dV) versus exponential (Exp)

bulge, and subsequent changes in disk and bar profiles], the scale lengths of the disk and bulge were varied to their 1σ observational limits in order to obtain a more complete coverage of parameter space.

The incomplete Gamma Function provides the goodness-of-fit for a system with n degrees of freedom (d.o.f.) and a χ^2 statistic. For a system with three d.o.f., a solution with the probability to 1σ (68%) of occurring not by chance, is given by solving,

$$1 - F(n/2; \chi^2/2) = 0.68 \tag{2.9}$$

where $F(\alpha; \beta)$ is the incomplete Gamma Function (Press et al. 1992). The solution for n=3 is $\chi^2_{\rm max}$=1.5. No model was found to be statistically acceptable according to the criterion of Equation (2.9). This is most likely due to the idealised mass models used. The model corresponding to the minimum value found will be investigated and improvements to the model discussed. The error analysis for the best fit result will provide information on the sensitivity of the solution to the different parameters. The errors on a parameter will be taken to be the deviation of the parameter value where the χ^2 increases by one, while holding the values of all other parameters constant. This is not a full covariant analysis where all parameters are varied simultaneously, but is suitable for the simple analysis presented here. The results of this section are only intended to be a guide to the information that can be obtained with more data for the system, applied in Chapter 4.

The results for the model with a de Vaucouleurs bulge are shown in Table 2.2, and an exponential bulge in Table 2.3.

These tables clearly demonstrate the superiority of the former over the latter. The χ^2 parameter for the exponential bulge results is evenly distributed between error in the rotation curve points and the image positions. It seems the rotation curve cannot be sufficiently constructed to satisfy the mass enclosed within the image radius as well as the two points measured in the curve. Similarly, the combination of bulge, disk and bar cannot produce the required shear as well as an acceptable rotation curve.

Conversely, the results for the de Vaucouleurs bulge and exponential disk are quite promising. None of the combination of scale lengths produced an acceptable χ^2 ($\leq$1.5), however, the values are of the right order of magnitude. The best result is produced at the 1σ upper limit of the disk scale length

r_b	3.1	3.1	3.1	2.8	3.4
r_d	8.6	9.5	7.7	8.6	8.6
r_c	15.3±0.4	13.4±0.4	14.9±0.5	-	14.5±0.4
σ_v	266±4	233±4	246±4	-	257±4
$\Sigma_{\rm bg}$	9.66±0.04	9.53±0.04	9.47±0.04	-	8.66±0.04
$\Sigma_{\rm dk}$	242±24	506±30	571±38	-	447±35
$\Sigma_{\rm br}$	824±23	821±20	818±20	-	783±22
χ^2	10.95	5.26	6.99	>500	9.81

Table 2.2: Best-fit parameters for a given model, exponential disk and de Vaucouleurs bulge. The scale lengths (r_b, r_d) are given in kpc; σ_v is the velocity dispersion (km/s) of the halo profile; $\Sigma_{\rm bg}$, $\Sigma_{\rm dk}$ and $\Sigma_{\rm br}$ are the central densities ($M_\odot pc^{-2}$) for the bulge, disk and bar respectively. The bulge values shown are divided by 10^5.

r_b	0.45	0.45	0.45	0.43	0.47
r_d	4.27	4.58	3.97	4.27	4.27
r_c	15.2	15.2	15.2	15.9	15.7
σ_v	243	243	243	262	239
$\Sigma_{\rm bg}$	3.0×10^4	3.0×10^4	3.0×10^4	3.2×10^4	2.9×10^4
$\Sigma_{\rm dk}$	0.0	0.0	0.0	3.6	0.0
$\Sigma_{\rm br}$	924	924	924	934	894
χ^2	140	140	140	106	210

Table 2.3: Same as for Table 2.2 except for an exponential disk and bulge. Symbols have the same meaning, but the bulge scaling is correct. Uncertainties were not calculated due to the large χ^2 values.

as measured by Schmidt. Without a continuum of solutions between these scale lengths, it is difficult to predict if an acceptable solution occurs within the measured limits. Without the added accuracy of further rotation points, this solution will be taken to be acceptable and the analysis based upon it. The χ^2 for this result is distributed evenly between error in the rotation points and the image positions.

Figure 2.3 shows the rotation curve produced from this solution and the components used to construct it. The total rotation curve is still rising at the edge of the plot due to the influence of the halo. Here, the three luminous components are falling away, particularly the bulge and bar which are essentially contributing no mass. This rise could pose a problem in that rotation curves are observed to be flat or falling. Simply scaling down the halo core size would alleviate this problem, however it would also affect the

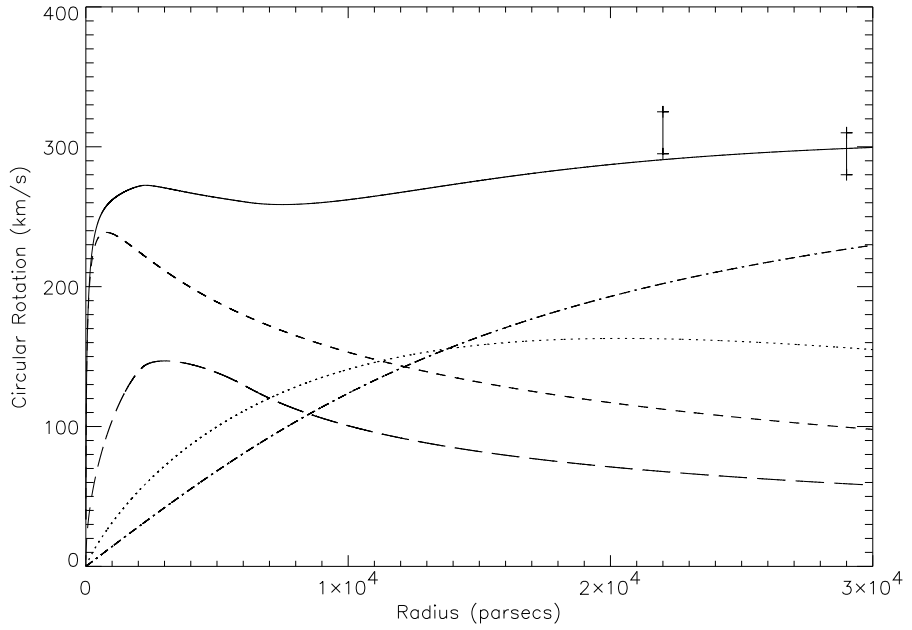

Figure 2.3: Rotation curve for the best solution (r_b=3.1kpc, r_d=9.5kpc, r_c=13.4kpc, σ_v=233km/s, $\Sigma_{\rm bg}$=9.53×10^{5}M$_\odot$/pc^2, $\Sigma_{\rm dk}$=506M$_\odot$/pc^2, $\Sigma_{\rm br}$=821M$_\odot$/pc^2) as in Table 2.2. The curves are total (solid), halo (dash-dot), disk (dotted), bulge (short dashed) and bar (long dashed). The two vertical lines denote the rotation points from HI measurements and their 1σ uncertainties.

convergence at the image positions. Although the halo does not contribute significant mass within the images, losing this would require a scaling up of another component. As all of the other modelled components contribute shear, this would affect the overall image positions and increase the χ^2. Another halo profile may provide a better fit.

As mentioned above, it is pertinent to calculate the projected mass of each of the components within the images. This involves the integration of mass within a cylinder out to the image radius and through the line-of-sight. Table 2.4 displays the results. The bulge clearly dominates the convergence within the image region. Variations in the overall scalings of the halo, disk and bar components will make less difference to the lensing than a change in the bulge value. These results demonstrate the nature of stacking these mass components. An increase in the halo mass (for example, due to a

Component	*Mass Enclosed* ($\times 10^8 M_\odot$)
Halo	6.8±0.2
Bulge	130.3±0.5
Disk	7.1±0.4
Bar	11.8±0.3
Total	156.0±1.4

Table 2.4: Projected mass within the image radius divided into the four mass components for the best fit solution of Table 2.2.

Group	ΔN *(arcsec)*	ΔE *(arcsec)*
1. Kent and Falco (1988)	-0.02±0.01	-0.08±0.02
2. Schneider et al. (1988)	0.015±0.005	-0.004±0.005
3. Schmidt et al. (1998)	$-0.014^{-0.003}_{+0.001}$	$-0.063^{-0.010}_{+0.009}$
4. This work	-0.014±0.001	-0.072±0.001

Table 2.5: Mean and standard deviation of the source position for different groups, as measured from the centre of the galaxy. ΔN and ΔE refer to the offset from the centre of the galaxy in the north and east directions.

small core region) would necessitate a decrease in the bulge. For this to be an adequate solution, however, the halo cannot be too large, otherwise it contributes too much rotation at the HI points, and the loss in shear from the bulge must be compensated for in another elliptical component. Thus, the combination of requiring correct convergence *and* shear is able to break the disk/halo degeneracy, removing the need to consider both maximal and minimal disks (Maller et al. 2000), is one assumes a spherical halo.

In addition to finding the best-fitting bulge and disk contributions to the rotation curve, one can perform a similar analysis on the source position for each potential solution. The results of this analysis are shown in Table 2.5, compared with those from previous groups. The source position for a given configuration was found by averaging the back-mapped positions of the four images. The results fit well with those of Schmidt et al. (1998) and Kent and Falco (1988), but not with Schneider et al. (1988). The consistency of three of the results is encouraging.

The image positions reproduced with this model are broadly consistent with observations. Figure 2.4 displays the model and real image positions, as well as the location of the source.

The total mass of each of the galactic components can be calculated. The optical disk extends out to $r \sim$ 25-30 kpc (Yee 1988) and the dark matter

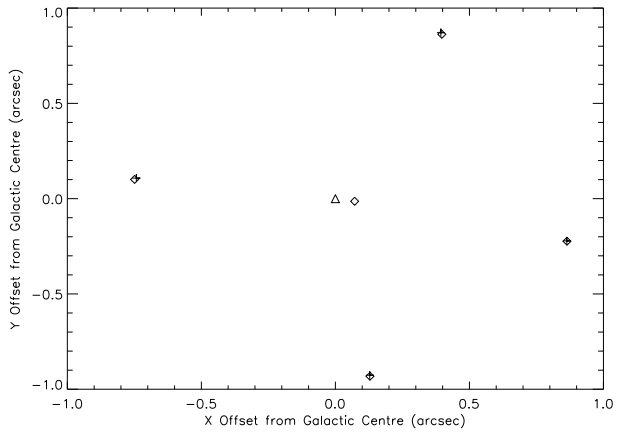

Figure 2.4: Comparison of the model and measured image positions for the best-fit solution. The crosses denote the model positions, the adjacent diamonds the measured, the triangle is the assumed galactic centre, and the isolated diamond is the source position. The 1σ uncertainties on the measured image positions correspond approximately to the size of the diamonds. The positions are labelled A, C, B, D clockwise from the bottom using the Yee (1988) convention.

halo will presumably continue far beyond this radius. As such, the masses calculated will be those enclosed within a sphere with radius $r = 30$ kpc, centred on the galactic nucleus. The results are displayed in Table 2.6. These values are consistent in their order of magnitude with the nominal mass ranges measured for galactic components. The dark matter halo contributes $\sim$60 per cent of the dynamical mass of the galaxy within the optically visible region. If the halo could be probed to larger radius, where, according to its rotation curve, it clearly extends, it would contribute much more to the overall galactic mass.

The surface mass distribution of the four components combined can be represented on a log-log plot to study the slope as a function of radius. This information is displayed in Figure 2.5. The dashed lines are normalised fits to $\Sigma \propto r^{-0.3}$ (short-dashed) and $\Sigma \propto r^{-1}$ (long-dashed). The central slope overall is reasonably steep given the large influence of the bulge. The dark matter halo has zero slope in the inner regions given its large core radius. The transition to $\rho \sim r^{-2}$ is expected given the dominance of the halo in the outer regions.

Component	*Mass (<30 kpc)* $h_{70}^{-1} M_{\odot}$
Halo	$(3.7 \pm 0.1) \times 10^{11}$
Bulge	$(6.7 \pm 0.1) \times 10^{10}$
Disk	$(1.7 \pm 0.1) \times 10^{11}$
Bar	$(2.3 \pm 0.1) \times 10^{10}$
Total	$(6.2 \pm 0.2) \times 10^{11}$

Table 2.6: Masses of the four galactic components from the potential solutions of Table 2.2. The values given are total mass within a radius of 30 kpc in solar masses. The range of halo values demonstrate the variation in total halo mass for the potential solutions.

2.4.2 Bulge and disk mass-to-light ratios

In order to analyse the bar in 2237+0305, Robert Schmidt decomposed light profiles by taking cuts along the major and minor galactic axes. These profiles can be used to investigate the mass-to-light ratio of the bulge and disk in the I-band (Schmidt, private communication). A deviation from a constant mass-to-light ratio across an individual component could either indicate the non-applicability of the mass profiles to this galaxy, or an intrinsic colour variation. Such a failure of the light to trace the mass would have implications for analyses of galactic disks where the assumption of constant mass-to-light ratio is often made.

The major axis light profile, once calibrated to units of solar luminosity, clearly displays the addition of two distinct components. The central region is dominated by a steeply falling bulge region, which flattens to a more gradually decreasing disk. The luminosity was calculated assuming a solar absolute magnitude in the V-band and correcting it to the I-band using the Vilnius spectral shifts of Bessell (1990).

The mass-to-light ratio for the disk is calculated, initially, by simply dividing the best fit mass profile by the luminosity profile (see Figure 2.6). The location of a probable spiral arm is visible as a dip at a radius of $\sim$13 kpc. The plot is not flat, as one would expect if the disk light followed a perfect exponential with the scale length used. Instead, there is a noticeable gradient to the ratio. This is possibly an indication of further structure beyond the simple models used. An additional minor difference between the models presented here and those of Schmidt is the use of a thick disk in this work. Finally, the presence of the bar affects the underlying mass

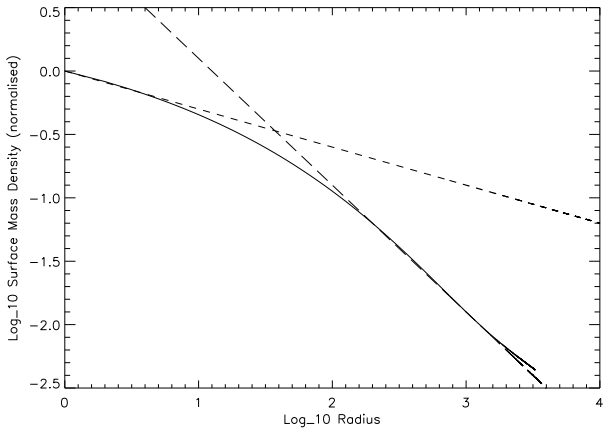

Figure 2.5: Log-log plot of the surface mass density of the inner regions of the best-fit solution (solid line). The short-dashed line indicates the slope of the profile in the central 10pc ($\Sigma \propto r^{-0.3}$). The long-dashed displays the transition to a more isothermal profile ($\Sigma \propto r^{-1}$) outside of the core.

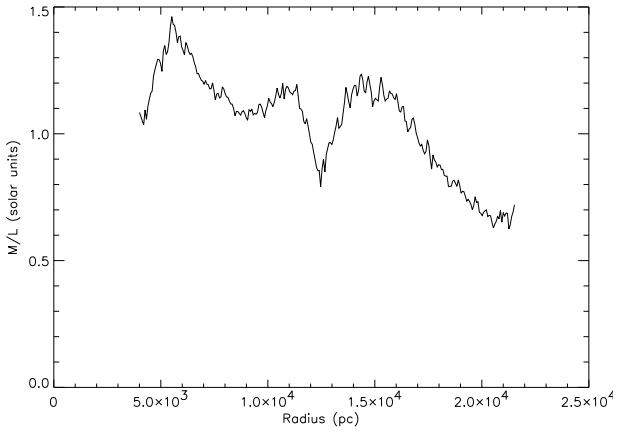

Figure 2.6: Disk I-band mass-to-light ratio as found by dividing the major-axis luminosity profile into the surface mass. The central 4 kpc has been removed to eliminate the effect of the bulge.

distribution. Interestingly, if the disk scale length is increased to $r_{\rm d} \sim$ 12kpc, the gradient virtually disappears. This does, however, neglect the bar influence on the light distribution. As a crude estimate of the value of the ratio, however, one can average the result from the curve to find,

$$(M/L)_{I,d} = 1.1 \pm 0.2h_{70}, \tag{2.10}$$

where I indicates the wavelength band and d denotes the disk.

This value is consistent with those from the literature. Syer et al. (1998) used disk stability arguments to place an upper bound on the I-band mass-to-light ratio, $(\mathrm{M/L})_I \leq 1.9\mathrm{h}_{100} \equiv 1.3\mathrm{h}_{70}$. An independent study using population synthesis models (Boissier and Prantzos 2000) gives $(\mathrm{M/L})_I = 1.0\text{–}1.3\mathrm{h}_{100} \equiv 0.7\text{-}0.9\mathrm{h}_{70}$. Finally, Sommer-Larsen and Dolgov (2001) use the I-band Tully–Fisher relation of Giovanelli et al. (1997) and their warm dark matter simulations to limit the mass-to-light ratio in this band to $(\mathrm{M/L})_I = 0.6\text{–}0.7\mathrm{h}_{60\pm10}$. These independent results fit well with the value found in this analysis.

By fitting an exponential curve to the light profile, outside of the bulge region of influence, the light contribution of the disk can be removed and the bulge mass-to-light ratio calculated. This technique assumes that the disk light follows the exponential decay to the centre of the galaxy and is not disrupted by the other mass components in that region. The light emitted within the image region is ignored, as this is contaminated by quasar light. The final profile for the best-fitting bulge model ($\Sigma_{\rm bg} = 9.53 \times 10^5\ \mathrm{M_\odot pc^{-2}}$) is displayed in Figure 2.7. This profile is reasonably flat over a large range of radii, but increases sharply for $r > 3$ kpc. This is the beginning of the region where both the disk and bulge contribute significantly to the light. Here, the disk exponential profile is a poor fit to the light profile and the disk subtraction removes too much light. This indicates the inadequacy of the two profiles to accurately account for the mass. It is possible the inclusion of the bar would add mass to the inner regions of the bulge area (its effectiveness is negligible beyond $r \sim$3 kpc) and increase the mass-to-light ratio. This could account for the slope at $r > 3$ kpc. Unfortunately, as the bulge and bar occupy the same radial regions, they cannot be deconvolved as the disk can. Taking the data from radii $r = 0.7\text{–}3.3$ kpc, the average

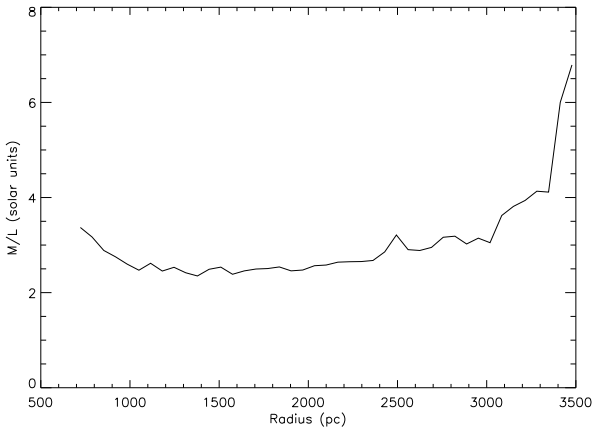

Figure 2.7: I-band mass-to-light ratio profile for the bulge component. The central 700 pc have been omitted to reduce the effect of contaminating quasar light. The sharp rise at $r \sim$3.3 kpc is the region between the disk and bulge where the mass distributions fail to fit the light profile adequately.

mass-to-light ratio is,

$$(M/L)_{I,b} = 2.9 \pm 0.5 h_{70}, \tag{2.11}$$

where b denotes the bulge component. Fukugita et al. (1998) find a value of $(\mathrm{M/L})_{B,b} = 6.5^{+1.8}_{-2.0}$ corresponding to $(\mathrm{M/L})_{I,b} = 5.0^{+1.4}_{-1.5}$ in the I-band using synthesis models and data from other groups. This determination agrees with the results presented here. It is encouraging to note the higher mass-to-light ratio in the older population bulge stars than for the younger disk stars.

2.4.3 Maximality

Maximal disks, whereby the disk contributes the majority of the rotation (75–95%) at the radius of its maximum circular speed, have been used in many studies to investigate the dynamics and structure of galaxies, as a means of deconvolving the disk from the dark matter halo. Physically, maximal disks have been found to be inconsistent with observations of gas motions in spiral galaxies combined with theoretical models (for example, Kranz et al. 2001). Observations of spiral galaxies have challenged the suggestion that disks are maximal owing to the need for a significant dark matter halo

(for example, Bottema 1997). Weiner et al. (2001) used observed velocity dispersions and gas dynamical simulations to reproduce the observed bar and spiral arms of a large spiral galaxy. They found the disk was maximal (80-100%) to high confidence. Conversely, Courteau and Rix (1999) find that their sample HSB galaxies are sub-maximal to high confidence using residuals from the Tully-Fisher relation and adiabatic infall of luminous material into dark matter potentials. Bottema (1993) used stellar velocity dispersions to infer the contribution from stars to the rotation curves in twelve disks. He finds $v_{\rm stars}/v_{\rm total} \sim 63\pm10$ per cent, below maximal according to the definition of Sackett (1997). The wide range of results suggest that there is a continuum of the degree to which the disk contributes to the mass, dependent upon, among other factors, galaxy morphology. The presence of a dominant bulge has also confused the issue somewhat, whereby the bulge is strictly maximal, but the disk may be insignificant.

The small variation in disk contribution to the 2237+0305 rotation curve, as demonstrated in Figure 2.3, provides a good determination of the degree of maximality in this galaxy. The overall rotation curve, although not constrained observationally in the region where this calculation is made (the disk maximum at $r \sim 2.2r_d$), is also reasonably tight given the HI constraints and the profiles used.

The contribution of the disk to the rotation has already been determined by its mean central surface mass density ($\Sigma_{\rm dk} = 506\pm30$ $\rm M_\odot pc^{-2}$). This corresponds to a maximum rotation of $v_{\rm disk}(2.2r_d) = 163\pm5$ $\rm kms^{-1}$. The maximum rotation is calculated to be $v_{\rm total}(2.2r_d) = 288\pm5$ $\rm kms^{-1}$. The percentage contribution of the disk to the rotation, the degree, is therefore,

$$\frac{v_{\rm disk}(2.2r_d)}{v_{\rm total}(2.2r_d)} = 57 \pm 3\% \tag{2.12}$$

This value fits well with those found by Bottema (1993) and Kregel (2003), and is well defined for the solutions presented in this work. This disk is clearly sub-maximal.

2.4.4 Flux ratios

The flux observed from each image in a gravitationally lensed system is a direct measure of the magnification in that region of the lens plane. A comparison between the flux ratios of the images observed in 2237+0305 and

Image	*Flux Ratio (Agol et al.)*	*Flux Ratio (this work)*
A	0.9±0.1	0.7±0.1
B	1.0	1.0
C	0.5±0.1	0.6±0.1
D	0.9±0.1	1.0±0.1

Table 2.7: Infrared flux ratios (relative to the B image) of the A, C and D lensed images, calculated from the fluxes of Agol et al. (2000) and the corresponding results from this work.

those predicted by the solutions can further act as a check on the results.

Observed fluxes in individual images are a combination of magnification due to microlensing, macrolensing and intrinsic variability coupled with time delays. Agol et al. (2000), however, have measured IR fluxes (8.9 & 11.7μm) for the four components and from these the ratio of fluxes can be calculated. In this region of the spectrum, microlensing events are not observed and it is therefore postulated that these observations sample an extended region of the source. In addition, the infrared fluxes are not as sensitive to the dust reddening effects of optical light travelling through the galaxy. Thus the IR fluxes should measure the macro-magnification. These fluxes, relative to the B image, are displayed in Table 2.7.

The flux ratios were calculated from the results by taking the ratio of the magnification for each of the images relative to the B image. The magnification is calculated by taking the ratio of areas of triangles around the images mapped from the image to the source plane. They were calculated from the best-fitting solution of Table 2.2 and are displayed in Table 2.7. These results are consistent with the observations within 1σ uncertainties.

2.5 Technique improvement

The use of a grid to calculate the bending angles is an inferior technique to an analytic expression, whereby the discrete summation over surface area becomes a continuous integral. Keeton (2001) presents a set of such expressions for commonly used surface mass distributions. Many of these require a numerical integral to be performed, however they are useful for two reasons: (i) they easily allow a standardised application of such parameters as ellipticity, which is critical for comparing different results; and, (ii) they are well-defined, removing the discreteness problems associated with summa-

DISK	M/L = free	**BAR**	M/L = free
	$r_d = 11.3 \pm 1.2''$[1]		e = 0.64[1]
	i = 60°[4]		PA = 39°[2]
	PA = 77°[2]		
BULGE	M/L = free	**DM HALO**	M/L = free
	$r_b = 4.1 \pm 0.4''$[1]	SIS	r_c = free
	e = 0.31[3]	eNFW	r_h = free
	PA = 77°[2]		e = free

Table 2.8: Fixed and free parameters and their source for the mass models of the four major components. The label 'free' refers to free parameters in the model and r_c and r_h denote the core radius and scale length respectively. [1]Schmidt 1996, [2]Yee 1988, [3]Racine 1991, [4]Irwin et al. 1989.

tions.

There are two primary differences between the mass models used in the above analysis, and the ones used with this new technique: the disk is modelled as a thin distribution, i.e. with no depth to integrate through; and, a flattened NFW profile is also explored for the dark matter halo mass distribution.

The disk is modelled as a thin structure with an exponential surface density profile, the bulge with a de Vaucouleurs profile and the bar as a Ferrers ellipse, in line with the previous work. The parameters characteristic of these models have been taken from previous observational studies and are presented in Table 2.8.

With the known image positions and rotation curve information, there are ten constraints on the model. For the softened isothermal sphere, there are seven free parameters and for the flattened NFW there are eight.

2.5.1 Inversion method

The unknown parameters are varied to fit both the image positions and rotation curve points using a basic minimisation procedure and the χ^2 statistic. The disk and bulge scale lengths are also allowed to move within their 1σ uncertainties in order to explore the parameter space adequately. The bending angles for each mass component are computed and their relative contributions (mass-to-light ratios) varied to fit the constraints. Solutions with unphysically large or small values for the mass-to-light ratios were dis-

	SIS	eNFW
$M/L_{disk,I}$	0.74±0.09	0.81±0.09
$M/L_{bulge,I}$	1.90±0.09	1.83±0.09
e_{halo}	0.	0.01
Scale	r_c = 1.03±0.02kpc	r_h = 12.0±0.6kpc
χ^2	1.4	1.0
$\chi^2_{\rm accept}$	1.5	0.9

Table 2.9: Best fitting parameter values for the two halo density profiles. Note the similarity between mass-to-light ratio values and the almost spherical NFW halo. The SIS has $e = 0$ by definition. The final row gives the 1σ acceptable χ^2 value.

counted. Since most components contribute shear as well as convergence to the lensing configuration, degeneracies exist between some parameters.

2.5.2 New results

Statistically acceptable solutions were found for both dark matter halo density profiles. The degree of ellipticity required for the flattened NFW profile was very small and consistent with zero. Both solutions provided similar convergence within the image regions and therefore allowed the same combination of the luminous mass components.

For 3 (2) degrees of freedom, an acceptable χ^2 value at 1σ confidence is 1.5 (0.9). Table 2.9 shows the best-fitting parameters for the models. It is evident from the similarity of the mass-to-light ratios and the small NFW flattening that these two halo profiles would contribute comparable convergence and shear to the lensing. Figure 2.8 shows the rotation curve of a galaxy with the best-fitting parameters for the softened isothermal sphere halo and luminous components. The bulge component clearly dominates the centre of the galaxy, providing the majority of the dynamical support within the image region. In the outer regions of the galaxy the dark matter component dominates, as expected from results of previous work deconvolving galactic rotation curves. The best-fitting rotation curve using the flattened NFW dark matter halo is essentially the same.

The disk is clearly sub-maximal according to the definition of Sackett (1997), however the importance of the bulge in this system should not be forgotten. This early-type spiral is not the ideal system for studying the

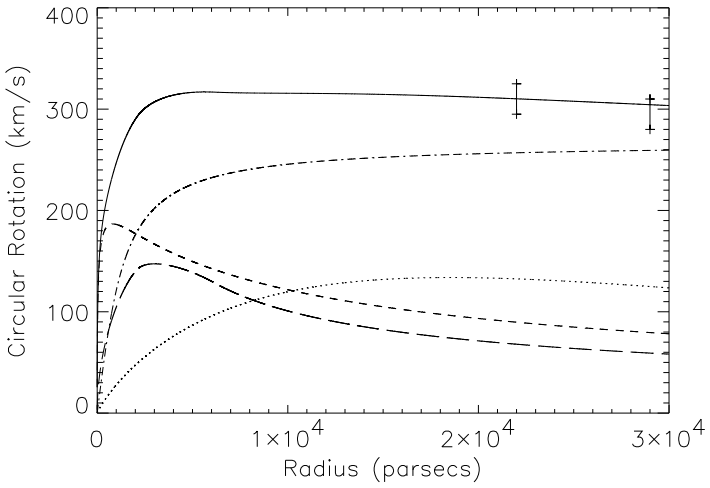

Figure 2.8: Best-fitting rotation curve based upon rotation points from HI observations and image positions for a softened isothermal sphere dark matter halo. The solid line is the total rotation curve, the dash-dotted line is the dark matter halo, the dashed line is the bulge, the dotted is the disk and the long-dashed is the bar.

importance of disk stellar support as the bulge clearly dominates the disk.

Comparison of the flux ratios shows excess flux in one of the images with both profiles for the dark matter. This result is quite robust and suggests an underlying problem in the mass distribution.

The one completely unknown component of the mass is the density profile of the dark matter halo. The best-fitting disk M/L and the bar mass agree with other estimates. If the bulge is too small in the models then it would appear the dark matter distribution would need to be changed to accommodate this. The most likely outcome is a halo with little contribution within the image region but sufficiently flattened as to counteract the increased torque from the bulge. Without further information, this is purely speculation.

Additional kinematic information can help to answer these remaining questions. With only rotation data for the outer galaxy, critical regions of the rotation curve are unknown. Well measured points in the galactic centre will tightly constrain the allowed dynamics in the important image region, as shown in Figure 2.9, which compares the expected observed rotation curve for this galaxy with a maximal bulge and the two different halo profiles. This

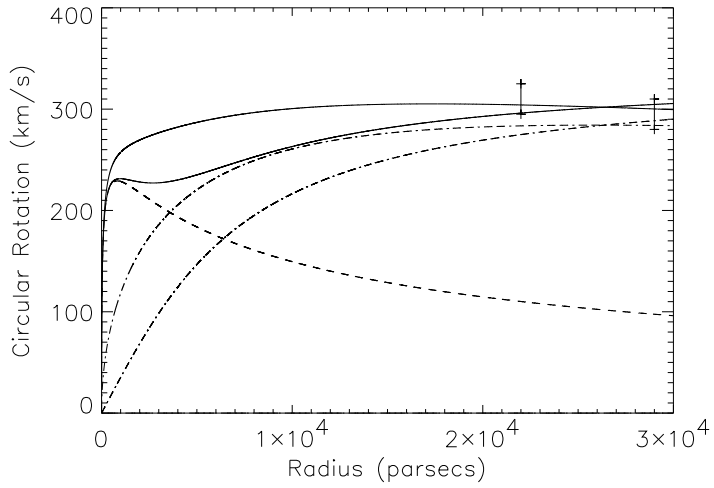

Figure 2.9: Comparison of expected rotation curves for a maximal bulge (M/L_I=3.0) with the two different halo profiles. The lower dash-dotted line shows the contribution of the SIS with r_c=5kpc and the upper, a spherical NFW with r_s=12kpc. The dashed line shows the bulge contribution. The two solid lines are clearly different in the inner regions.

solution does not fit the image positions, but shows the possible difference in the inner rotation curve. It is this splitting of curves that will be probed with spectroscopy of the galaxy from the Keck telescope (Chapters 3 and 4). With this improved analysis, statistically acceptable solutions are obtained, but the flux ratios do not fit.

2.6 Implications for the dark matter halo

The SIS halo model is a generic profile that is analytically simple but disagrees with the results from N-body simulations (it is possible, however, that the simulations may not reflect nature faithfully, Trott and Melatos 2005). It does, however provide a mass profile with varying slope, and this is a useful attribute if one wishes to study the gradient of the mass distribution, and corresponds loosely to the solution for secondary infall onto a spherical perturbation (Bertschinger 1985).

The best-fitting solutions for the mass distribution of this galaxy are not adequate fits — either because the χ^2 is too high, or the flux ratios are not consistent with observations.

The rotation curve is rising at the outer regions instead of falling, and the modelled images are not within the errors of the measured positions. A halo with a smaller core would alleviate the former problem but require a change of the other mass distributions to address the latter. The mass-to-light profile of the disk suggests an increase in the disk scale length. Such a move would change the shear introduced by the disk. The size of the core region is not consistent with the cuspy central regions of CDM profiles from N-body simulations. In order to reduce the χ^2 and find an adequate solution, further rotation data are required. The more kinematic data available, particularly in the image region, the more discriminating power one has between models. Until more data are obtained, it is not worth trying to fine-tune the halo profile to fit the parameters more closely. If the error bars on the HI rotation points are incorrect, the rotation curve may become quite consistent with the observations (the observations by Barnes et al. 1999, were undertaken with the VLA C array, a compact configuration with low angular resolution), but the flux ratios will still not fit. Higher resolution observations will provide tighter constraints on the model.

It is worth remembering that the halo is assumed spherical in this work because not enough information is known about the system to warrant a more complicated model. As discussed before, numerical simulations of purely collisionless particles result in triaxial halos, whereas studies of our own Galaxy show the halo to most likely be close to spherical (Ibata et al. 2001). Flattening the halo allows more projected mass to lie within the image region and therefore reduces the contribution from the visible components. Given that the spherical halo is found to contribute <10 per cent of the mass within the image region, playing with the ellipticity with the amount of information available would not provide any more meaningful information about the galaxy.

How much does one force the galactic mass distribution to be of a given form, by modelling it with parametric models, as opposed to directly investigating the light distribution? Parametric models assume a given structure for a mass component. If this model does not faithfully represent the real structure of the component, systematic errors are introduced into the modelling. These errors can be quantified either by trying many different models and comparing results, or by assuming a constant mass-to-light ratio and calculating the bending angles from the observed light curves alone (this is

only useful for luminous components).

The lensing probes the projected mass enclosed within the images, and the quadrupole moment of the lens. Wambsganss and Paczynski (1994) showed that for a given assumed power-law surface mass density, the index is degenerate with the external shear in the 2237+0305 system. Such degeneracies can be broken with use of the flux ratios of images (which probe the gravitational potential) and time delay measurements. For this system, the time delay is expected to be short [$\Delta t \propto (1+z_{\rm d}) D_{\rm d} D_{\rm ds}/D_{\rm s} b^2$ $\sim$1 day, where $b \sim 1''$ is the characteristic size of the image region] and is unmeasured due to the confusion of microlensing flux variations (the flux ratios are somewhat contentious, as discussed earlier).

In 2237+0305, the lensing probes the mass enclosed within the images extremely well, rather than the slope of the profile in the image region (which is degenerate with external shear). This is because all images effectively lie at the same radius and so the shape of the profile can be changed and the convergence remains the same (Kochanek 2004). In other systems with images at different radii, the dependence on the mass slope is stronger because the locations of two of the images can be used to probe the structure in the annulus between them. In this way, systems with extended images that lie over a large range in lens galaxy radius, can provide information about the mass slope in that region (e.g. 1549+3047, a lensed radio lobe showing images in the radius range $0 < r \lesssim 2''$, Lehar et al. 1993).

The lensing cannot provide information away from the image region, since the photons do not probe these paths. The distribution of matter (i.e. clumpy or smooth) internal to the images (internal shear) is irrelevant to the lensing, except on large scales — the overall potential's shape and depth. Similarly, matter outside of the images (external shear) can affect the image locations, but cannot be characterised by the lensing except for as an overall external shear. Kinematic information is required away from the images.

As most lens galaxies have images lying $\sim$5 kpc ($\sim 1''$, z_d=1) from the galactic centre [most lens galaxies lie within $0 < z_d < 1$ since, for a SIS lens, $\alpha = 1.2'' D_{\rm ds}/D_{\rm s}$ $(\sigma/200{\rm kms}^{-1})^2$ and as $z_d \rightarrow z_s$, $D_{\rm ds} << D_{\rm s}$, making the images unresolvable for higher redshift lens galaxies], the lensing can often probe a region where the light and dark matter have comparable contributions. In the case of 2237+0305, the images primarily probe the stellar bulge, and so can provide most information about it. Only the

lensing combined with well-sampled kinematic information can provide any larger scale information about the galaxy. Mass profiles must always be assumed in point-source lenses, (unlike extended-source lenses, where many lines-of-sight provide significantly more information), but one must be careful when quoting random uncertainties on model parameters to not forget the systematic uncertainties introduced when one uses parametric models. This point is clear in Figure 2.9 where the two different halo profiles, NFW and isothermal sphere, produce equally good fits to the image positions and HI rotation points, because they are able to be tuned to fit at these two different radii. Thus, the use of high quality kinematic data in the modelling can improve the results by providing additional information that is dependent upon the mass structure of the system.

2.7 Rotation curve measurements

Additional kinematic information is required to remove the strict reliance on parametric models of the dark matter halo, and hence to fully explore the different models proposed in the literature. A fuller rotation curve is the first obvious step towards achieving this, and attempts were made to obtain one, as discussed below.

2.7.1 Optical spectrum with the ANU 2.3m

With little spectral information available for the lensing galaxy itself (most previous work concentrated on the quasar spectrum), the availability of spectral features needed confirmation before a rotation curve could be attempted. 2237+0305 is a barred Sa–Sab type galaxy, the spectra of which are characterised by small equivalent widths of the Balmer emission lines, and many absorption features (Kennicutt 1992; Slonim et al. 2001). Given these previous results from this morphological type, one would not expect to find any emission lines in the optical band.

To confirm this, and attempt to identify strong absorption features, the lensing galaxy was observed over two nights with the 2.3m MSSSO telescope at Siding Spring Observatory in 2002 July. The Double Beam Spectrograph was used to obtain both red and blue spectra, and the 1200 lines/mm grating employed for high spectral resolution (second order used for the blue arm).

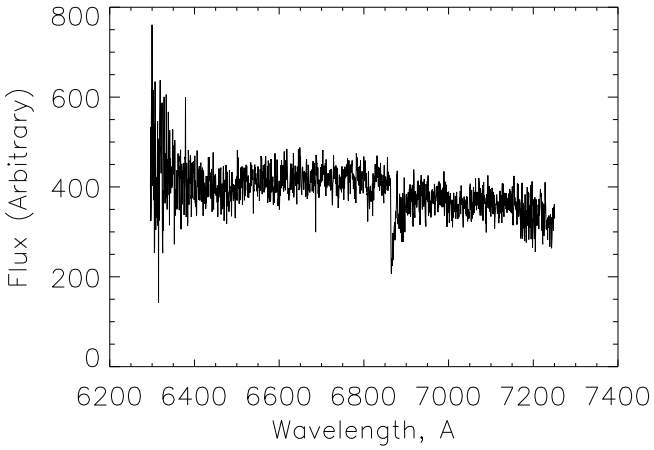

Figure 2.10: 2400s red spectrum of the central arcsecond of the galaxy from the 2.3m telescope using the 1200 lines/mm grating. The feature located at $\sim$ 6850Å is due to sky absorption. There are no directly visible features in this spectrum, although there is possibly Hα absorption at $\sim$ 6820Å. However, this would signal the presence of hotter stars in the bulge than G-type.

Four observations were undertaken of the galaxy in dark time, two with 2400s integration time, and two with 1800s. The seeing was poor ($\sim 2''$) with high humidity in the dome ($\sim$ 95 per cent), making observing difficult. The red arm gave a spectral resolution of $\Delta v = 48$ kms^{-1} ($\Delta\lambda$=950Å), and the blue, $\Delta v = 29$ kms^{-1} ($\Delta\lambda$=440Å), centred upon 6830Å and 5200Å respectively. The spatial resolution comprised 532 pixels over $40''$, with a resolution of $0.07''$/pixel, corresponding to $\sim 70 h_{70}^{-1}$pc at z=0.039, and the slit was set to $1.0''$, balancing maximum signal and optimal resolution, given the poor conditions, with an attempt to retain some degree of good spectral resolution and avoid quasar contamination.

The resulting spectra for the central $1''$ of the galaxy are plotted in Figures 2.10 and 2.11. They are extremely noisy, clearly displaying only the CIII] line from the quasar images. There are hints of possible absorption lines, based upon the expected features for the dominant bulge stars (Giant G, K and M-type). No emission lines are expected for these cool stars (strong Balmer lines are visible in absorption for hot O and A-type stars, but not for cooler stars), but Mg, Ca and Fe features are common (neutral metals,

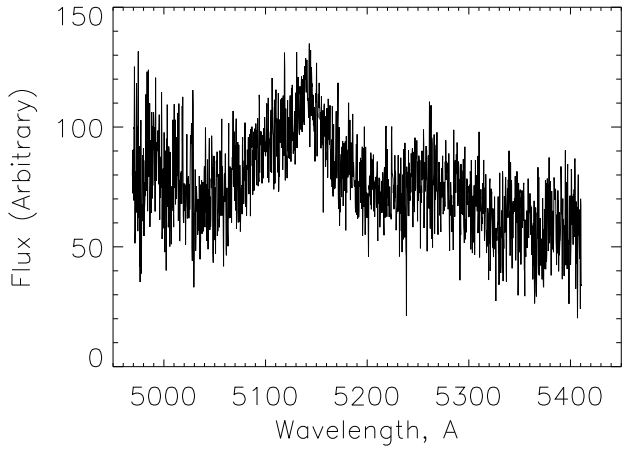

Figure 2.11: 1800s blue spectrum of the central arcsecond of the galaxy from the 2.3m telescope using the 1200 lines/mm grating in second order. The CIII] semi-forbidden line from the quasar images is visible as the peak at $\sim$ 5140Å, but the spectrum is too noisy to identify any galactic absorption features.

Carroll and Ostlie 1996).

Unfortunately, these spectra were not of sufficient quality to calculate a rotation curve, or, more basically, identify with certainty any absorption lines to take to a larger telescope.

2.7.2 Neutral hydrogen rotation curve with GMRT

The data cube presented in Barnes et al. (1999) from the VLA shows the existence of neutral hydrogen in the outer regions of the galaxy. A higher resolution and sensitivity observation of the system should yield much tighter kinematic constraints to better quantify the outer rotation curve. We proposed to use the newly available Giant Metrewave Radio Telescope (GMRT), located close to Pune, India, to undertake spectroscopic observations. Observations were carried out in 2002 April.

GMRT is a 45 element interferometric array comprising 30m dishes in a pattern optimised for good angular resolution and spatial sensitivity. The longest baselines are $\sim$25km, and the central 1km is packed with 29 of the antennae, for excellent sensitivity at low resolution.

2237+0305 was observed at 1370MHz (21cm line at 11695kms^{-1}) for 20 hours, with 128 channels spread over 8MHz, producing 13.2kms^{-1} velocity resolution. These observations were based upon quoted sensitivity levels which would produce an rms noise level of 0.15mJy/beam. Barnes et al. (1999) measured a total integrated line flux of 1.0±0.1 Jykms^{-1} over 550kms^{-1} and with a spatial diameter of 70″ with the VLA-C array. With a synthesised beam of 2″ and 550kms^{-1} velocity width, and using the moment map produced by Barnes to identify the area over which 21cm emission is observed, the expected signal is ∼0.2 mJy/beam/62.5KHz channel. This does not provide sufficient signal-to-noise (∼2), but spatial binning of the spectrum during data reduction will improve results.

The observations were marred by instrumental problems, including power failures that led to more time being allocated to the project. Additionally, most of the long baseline antennae were offline for some or all of the observations, reducing the collecting area by one third. The data were also largely affected by interference, with almost ten per cent of the data discarded.

In addition to these problems, at this time the GMRT was not operating at specified sensitivity, and careful data reduction with the AIPS package was not able to reduce the rms noise below ∼2 mJy/beam, unacceptably high for a galaxy with such low HI emission. As a result, no kinematic information came from these data.

2.8 Conclusions

A study of the structure of galaxy 2237+0305 was undertaken using photometric and gravitational lensing constraints. The combination of these techniques allows the problems related to the disk/halo degeneracy and the question of maximality of the disk to be overcome, provided enough kinematic information is known about the system, and assuming parametric models for the mass components.

The galaxy is adequately modelled with four mass components, a central bar, stellar disk, bulge and dark matter halo. The bulge contributes ∼85 per cent of the projected mass enclosed within the image radius, and is thus the principal component to which the lensing is sensitive. The disk, bulge and bar all contribute shear, while the assumption of sphericity for the dark matter halo seems adequate for this analysis with the observational

information available.

Within the visible radius of the galaxy ($r < 30\mathrm{h}_{70}^{-1}$ kpc), the dark matter halo contributes ∼60 per cent of the total mass. The potential existence of a core region in the softened isothermal sphere halo is suggested by the results, but both a SIS and NFW profile produce equally good fits to the data. The best reconstruction of the source position occurs for a SIS halo with a core radius of 1.03±0.02kpc, or an NFW halo with $e = 0$ and r_h=12.0±0.06kpc.

The disk is found to be sub-maximal to 5σ with an average contribution of 57±3 per cent to the rotation at the maximum of its circular speed. This clearly demonstrates the dominance of the dark matter halo in the galactic mass. The disk and bulge I-band mass-to-light ratios were calculated using the mean and standard deviation of the potential solutions. They were found to be $(\mathrm{M/L})_{I,d} = 0.74\pm0.09\mathrm{h}_{70}$ and $(\mathrm{M/L})_{I,b} = 1.90\pm0.09\mathrm{h}_{70}$, respectively (SIS model). The flux ratios between the quasar images calculated from their magnifications were found to be consistent with mid-infrared data, in all but one image.

The above results rely heavily on the parametric models assumed for the mass components, and therefore further information is required (most readily available as kinematic information) to remove some of the reliance on these models, and more fully probe the galactic mass structure. Consequently, with the addition of rotation curve information, the dark matter profile can potentially be found uniquely. Until such information is available, the system remains ill-constrained and unsolved.

Kinematic information was sought in both the optical and radio wavebands. Optical spectra taken with the Double Beam Spectrograph on the MSSSO 2.3m telescope in 2002 July were not of sufficient quality to identify spectral features worthy of analysis. This was due to a combination of small telescope aperture and bad seeing at the site.

Neutral hydrogen line emission at 21cm from the galaxy was observed at GMRT, India in 2002 April. The combination of loss of one third of available antennae (including most long baselines) and the poorer than expected sensitivity performance of the telescope, led to no useful data being obtained.

CHAPTER 3

2237+0305: Keck Data

The Echelle Spectrograph and Imager (ESI) on the Keck-II telescope is used to measure a high spectral and spatial resolution spectrum of the galaxy 2237+0305 and the lensed quasar images. The data are split into ten echelle orders giving a spectral range of $\lambda = 4000$Å – 10000Å at a velocity resolution of 36.1 kms^{-1}. These data are used to extract a rotation curve and velocity dispersion profile for the galaxy, based upon measurements of the Mgb, FeIb and Nad absorption lines. The results are consistent with previous measurements for the system.

3.1 Introduction and past observations

2237+0305 has been observed many times since its discovery as a candidate lens in 1985. Previous published spectra of 2237+0305 have either concentrated on the quasar spectrum, or only presented a small wavelength range for the galaxy spectrum. The paper presenting the discovery of the system as a lens, Huchra et al. (1985), displayed a quasar spectrum taken with the MMT and featured both the CIV and CIII] broad lines. In addition, they identified the H+K break at ∼4100Å and Mgb absorption (5381Å). This spectrum was not of sufficient quality to identify any further features, but was successful in its primary aim: to confirm the system as a lens. Foltz et al. (1992) observed the galaxy to determine a velocity dispersion for the bulge. They identified Mgb and FeI absorption features to use in their analysis, but presented a spectrum over only a small wavelength range (5100–5550Å). Lewis et al. (1998) concentrated their WHT observations around the quasar emission lines to investigate variations between the four images, thereby inferring microlensing effects (line and continuum regions are expected to behave differently under microlensing conditions because the flux emanates from regions of different source size). Most recently, Rauch et al. (2002) identified absorption lines in the spectrum from intervening (between lens and source) objects using the HIRES spectrograph on Keck. These spectra display high resolution profiles of the absorption lines of the intervening systems and as such do not concentrate on the spectrum of the galaxy as a whole.

As discussed in Chapter 2, a high resolution optical spectrum of 2237+0305 is required for a comprehensive analysis of the mass distribution of the system. The rotation curve needs to be well-sampled, both inside and outside of the image region for the kinematic and lensing information to complement each other. In addition, a large telescope is required with good seeing to obtain this (see discussion in Chapter 2). The ESI instrument on Keck meets these requirements. The site seeing is generally very good (better than $1''$, required for independent rotation curve points within the images) and the large collecting area provides high signal-to-noise in the echelle mode. The high spectral resolution produces kinematic data with small uncertainties, thereby improving the power to discriminate between different mass models.

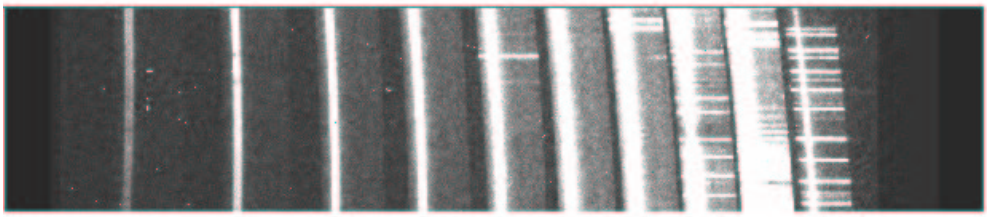

Figure 3.1: Image of the ESI CCD showing the ten wavelength orders (lowest to highest, left to right) for one 1200s exposure along the galactic major axis. Cosmic rays and sky lines are visible across the spectra.

3.2 Observations and data reduction

2237+0305 was observed as part of the Lenses Structure and Dynamics Survey (LSD, e.g. Koopmans and Treu 2002), a project aiming to measure stellar kinematic information in lens galaxies to better model them and break degeneracies in their mass models. The data were taken on 2001 July 21, 23 by Leon Koopmans, Tommaso Treu and Chris Fassnacht with the Keck II telescope on Mauna Kea, Hawaii. The Echelle Spectrograph and Imager (ESI) instrument was used in echelle mode, providing high resolution (R $\sim$ 30000) spectra in the wavelength range $\lambda = 3900 - 10900$Å over ten echelle orders.

The ESI instrument on Keck II provides a constant velocity dispersion across all orders of 11.9 kms^{-1}pixel^{-1}, and a spatial resolution along the slit of 0.154 arcsec/pixel. The spectral resolution varies with wavelength from $\sim$ 0.16 – 0.3 Å/pixel, depending on the order, but is dependent upon the slit width (the galaxy was observed with slit width 1.25″ giving Δv=36.1 kms^{-1}pixel^{-1}).

Figure 3.1 displays the CCD for one 1200s exposure along the major axis, showing the ten curved wavelength orders, as well as cosmic rays (bright points) and sky lines (horizontal emission lines in spectra). Some absorption features are also visible in the spectra, although many are sky absorption rather than galactic. The spectra need to be separated, rectified to remove their curvature, cosmic ray rejected and sky subtracted. The different exposures can then be combined into a single 2D spectrum (wavelength versus position along the slit).

The slit width was set to 1.25″ for greater signal, and the seeing was

Date	Object	Type	PA (°)	Slit Position	Slit Width	Exp. Time (s)
July 21	2237+0305	-	65	5″ offset	1.25″	1200
July 21	″	-	155	5″ offset	1.25	1200
July 21	″	-	155	centred	1.25	1200
July 23	″	-	65	centred	1.25	1800
July 22	HR14	K2III	-	centred	0.3	4
July 22	HR19	K0III	-	centred	0.3	4
July 22	HR224	K5III	-	centred	0.3	1
July 22	HR22	G9III	-	centred	0.3	2
July 22	HR279	G7III	-	centred	0.3	2
July 22	HR40	G0III	-	centred	0.3	4
July 22	HR4	G5III	-	centred	0.3	4
July 22	HR60	G8III	-	centred	0.3	3

Table 3.1: Observational parameters for G2237+0305 and template stellar spectra (Harvard Revised Number, HR). The galaxy spectra were taken ∼10° rotated from the major and minor axes, and two were observed with the galaxy offset 5″ from the slit centre in order to sample the outer regions on one side.

0.6″ on both nights. Bias frames were taken at the beginning and end of each night, as well as Quartz and dome flats on July 21, and sky and dome flats on July 23. Three wavelength calibration arcs were taken and a spectrophotometric standard star observed.

2237+0305 was observed along perpendicular directions, sampling the major and minor axes and the locations of the lensed quasar images. Table 3.1 summarises the key observational data for the galaxy. Note that the galactic major axis is at a position angle of 77° (measured East from North).

In addition to the galactic exposures, template stellar spectra are required to measure the rotation and velocity dispersion of the galactic spectral features. Eight stars of contiguous stellar type were observed and their parameters are also shown in Table 3.1. The bulge of the galaxy is primarily observed in these observations, and so the template spectra are of old, red stars expected in such an environment. The I-band images of 2237+0305 presented in Yee (1988) show the bulge to be dominated by old and red stars with $(g - r)$=0.58 (V – R=0.9, Windhorst et al. 1991) corresponding to Giant K0III–K5III stars.

The ESI observations require some special preparation and calibration before they can be combined and used for kinematic analysis. The calibration process undertaken includes the following steps:

- Bias subtraction — removes any dark current contribution to the sig-

nal,

- Flat fielding — removes response function of CCD to a uniform illumination of incident light,
- Rectification — the curvature of the spectra, seen in Figure 3.1 is removed,
- Cosmic ray rejection — removal of signal spikes due to cosmic rays,
- Sky subtraction — background influence of the sky is subtracted using sky flats.

Many of these steps were performed by the package **EASI2D**, which is developed by the LSD group and David J. Sand (Sand et al. 2004) for easy extraction of echelle orders.

Individual observations were then aligned with the IRAF package **imshift** and combined with **imcombine** (the package **imexam** was used to find the amount by which the spectra should be shifted). The spectra are not flux calibrated (spectrophotometric standards were observed, but flux calibration is not required for the kinematic analysis).

3.3 Optical spectrum of 2237+0305

As displayed in Figure 3.1, the galaxy appears to occupy only the central regions of the slit. Imaging observations (e.g. Yee 1988) show the optical galaxy to extend well beyond $10''$, however the surface brightness rapidly decreases below the sky background, and it is not observable in these high resolution spectral data with a slit aperture reducing the photon counts. As such, only the central regions of the galaxy are available for measurement of stellar kinematics. Figure 3.2 shows a slice through the spectrum (in a continuum region of Order 5) along the slit. The galaxy is prominent in the central few arcseconds, but rapidly disappears below the sky background at a radius of $\sim 3''$, although the slit itself is $20''$ long. The central peak is the galactic nucleus, however there is a feature in each wing of the galaxy profile, corresponding to two of the lensed quasar images. With the large slit width used and the $0.6''$ seeing, one would expect contamination from the quasars in the spectra, as their flux is comparable to that of the galactic centre.

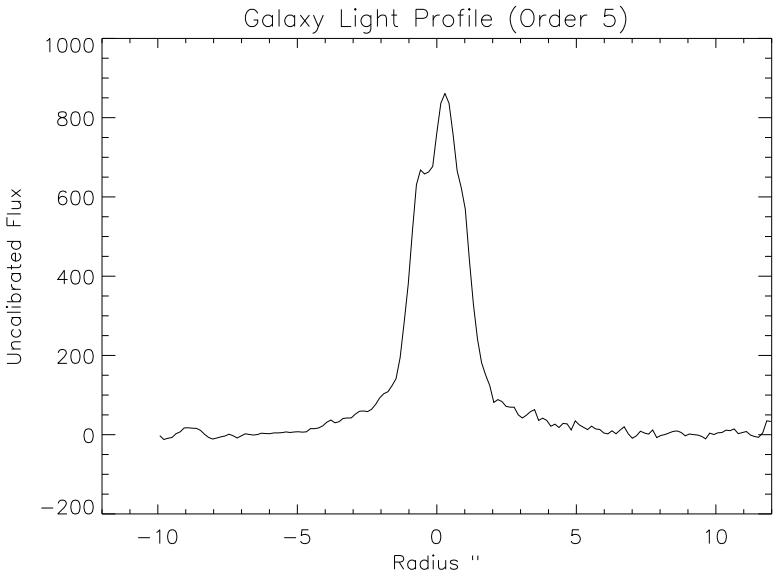

Figure 3.2: Profile of the major axis of the galaxy plus quasar images along the slit for Order 5. The central peak is the galaxy centre, and the two features in the wings correspond to the quasar contamination. Only the central few arcseconds have sufficient signal to be useful for kinematic measurements ($1'' = 0.7$kpc).

From the data reduction performed above, the spectra of each order can be presented and lines identified to measure the stellar kinematics. Figures 3.3–3.12 show the ten spectral orders by averaging the central four arcseconds in order to increase the signal-to-noise ratio. Four arcseconds corresponds approximately to the region over which S/N > 5.

Prominent spectral features are marked on the spectra. The line-of-sight absorption systems, reported in Rauch et al. (2002), between the lens galaxy and background quasar are also confirmed in these spectra. There are no obvious galactic emission lines, as expected from an old stellar population. The Hα line (6821Å observed) is partly obscured by the B-band atmospheric water vapour absorption line in lower resolution spectra (see Section 2.7.1), however our higher resolution observations can separate the two lines and Hα emission is not found to be present. The broad emission lines of the lensed quasar images, CIV (4175Å), CIII] (5145Å) and MgII (7541Å) are prominent, with CIV suffering from sky absorption (see also Huchra et al. 1985). Table 3.2 shows the wavelengths of the lines located in the spectra

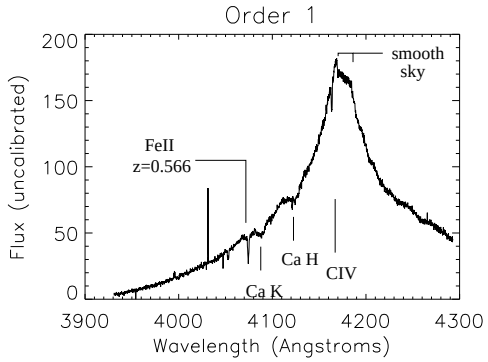

Figure 3.3: Order 1: sky-subtracted 2400s spectrum of 2237+0305 taken at a position angle 12° clockwise from that of the major axis. A defect at ∼4170Å, due to sky lines, has been interpolated. Both the Ca H&K absorption lines are seen here, as well as FeII absorption from a background absorber at z=0.566 (Rauch et al. 2002).

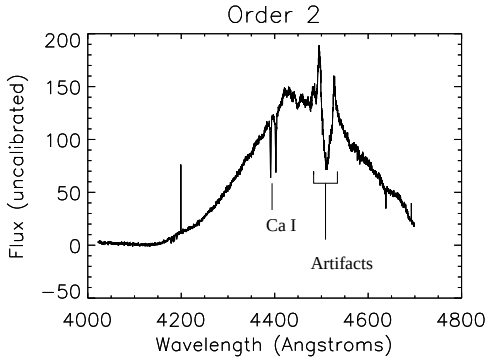

Figure 3.4: Order 2: sky-subtracted 2400s spectrum of 2237+0305 taken at a position angle 12° clockwise from that of the major axis. CaI absorption in the lensing galaxy is shown here. The large feature at 4400–4550Å is an artifact of the rectification process in the **EASI2D** routine.

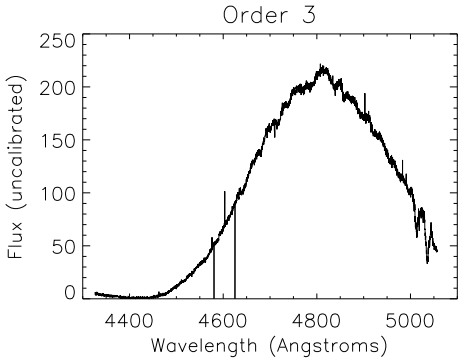

Figure 3.5: Order 3: sky-subtracted 2400s spectrum of 2237+0305 taken at a position angle 12° clockwise from that of the major axis. The two apparent absorption features at 5000-5100Å are again due to incomplete rectification of the echelle orders.

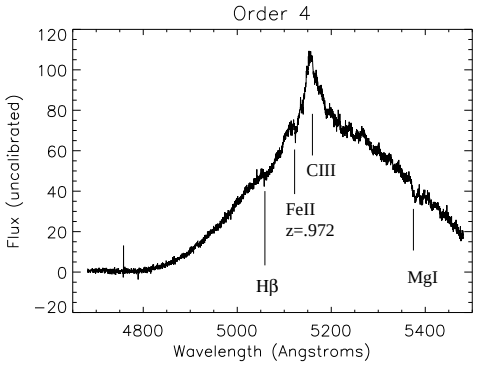

Figure 3.6: Order 4: sky-subtracted 2400s spectrum of 2237+0305 taken at a position angle 12° clockwise from that of the major axis. The quasar CIII] semi-forbidden line is the strong peak in the centre and MgIb and Hβ absorption by the lensing galaxy are visible. The FeII absorption feature is consistent with the z=0.972 absorber proposed by Rauch et al. (2002).

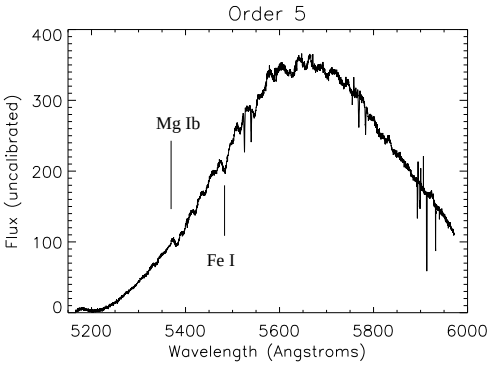

Figure 3.7: Order 5: sky-subtracted 2400s spectrum of 2237+0305 taken at a position angle 12° clockwise from that of the major axis. The FeI and MgIb lines used in the kinematic analysis are shown in this order.

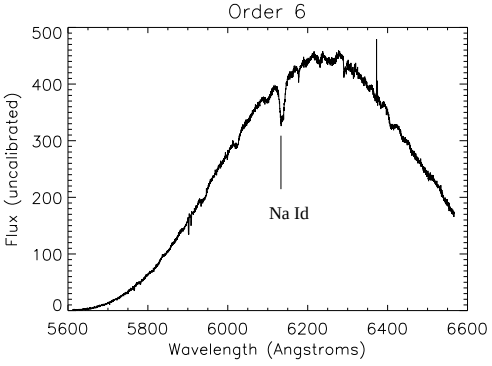

Figure 3.8: Order 6: sky-subtracted 2400s spectrum of 2237+0305 taken at a position angle 12° clockwise from that of the major axis. The strong sodium absorption feature, Nad, is used in the kinematic analysis.

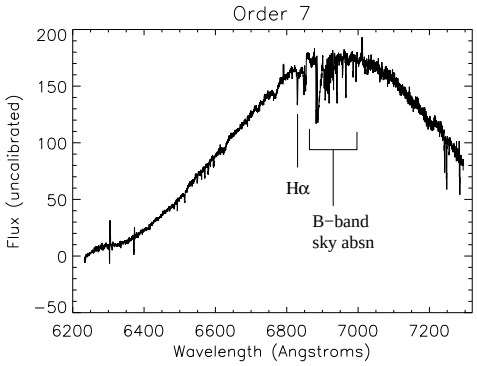

Figure 3.9: Order 7: sky-subtracted 2400s spectrum of 2237+0305 taken at a position angle 12° clockwise from that of the major axis. The expected Hα absorption at 6820Å is partly obscured by sky lines.

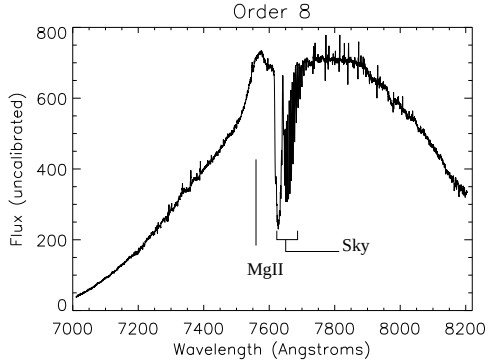

Figure 3.10: Order 8: sky-subtracted 2400s spectrum of 2237+0305 taken at a position angle 12° clockwise from that of the major axis. The red wing of the quasar MgII emission line is partly obscured by sky lines.

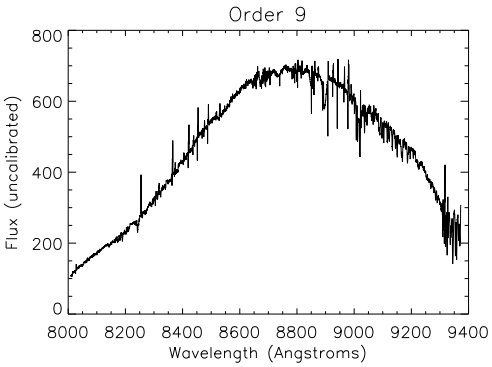

Figure 3.11: Order 9: sky-subtracted 2400s spectrum of 2237+0305 taken at a position angle 12° clockwise from that of the major axis.

Spectral Order	Line	$\lambda_{\rm rest}$ (Å)	$\lambda_{\rm obs}$ (Å)	z
1	FeII	2600	4074.5	0.559
1	Ca K	3933.7	4088.9	0.0394
1	Ca H	3968.5	4121.4	0.0385
1	CIV	1549	4173.8	1.694
2	Ca I	4227	4391.4	0.0389
4	FeII	2600	5136.9	0.976
4	CIII]	1909	5147.6	1.696
4	MgIb	5173	5377.2	0.0394
5	FeI	5268	5483.8	0.0410
6	Nad	5896	6130.5	0.0397
8	MgII	2798	7570.0	1.706

Table 3.2: Derived redshifts based upon Gaussian line centres from the spectra compared with rest values. Rest wavelength values of absorption features from Cox (2000).

(fitted with a Gaussian to find the line centre), calculated at the galaxy centre to determine the emitter/absorber redshift. Most lines are well-fitted to the published galaxy and source quasar redshifts of z=0.0394 and z=1.695, respectively. The high value for the redshift of the MgII emitter is due to the sky lines redward of its centre contaminating the fit. Some of the features identified by Rauch et al. (2002) are also reproduced here. The by-eye identification of both Hα and Hβ absorption in the galaxy (shown in Figures 3.6 and 3.9) seems premature since both exhibit redshifts too large compared with the galaxy (z=0.052, 0.042, respectively). This is also potentially due to inaccurate wavelength calibration of these spectra (although other lines in Order 4 are well-fitted). Importantly, both Mgb and Nad reproduce the

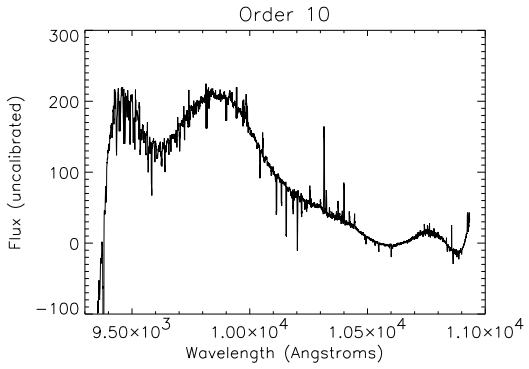

Figure 3.12: Order 10: sky-subtracted 2400s spectrum of 2237+0305 taken at a position angle 12° clockwise from that of the major axis. Poor cosmic ray subtraction produces the narrow features observed here.

galaxy redshift well, although the FeI line produces a redshift that is too high (this is shown later to be due to the crowding of lines in Order 5, and the probable misidentification of the strongest line with FeI absorption).

There are also cases of incomplete rectification by the **EASI2D** reduction routine in the spectra, where flux leaking from the spectrum produce unphysical features in the spectra. These features have been identified in Orders 2 and 3. There is no such problem in the rectification of orders used in the kinematic analysis.

3.4 Data analysis

Given the lack of emission lines in the spectra of the old stellar population, strong absorption features need to be used in the kinematic analysis. The highest signal-to-noise feature in the spectra is the Nad doublet at $\lambda = 5890$, 5896Å rest (6125, 6131Å observed). This feature sits in the middle of Order 6, mostly uncontaminated by sky absorption and away from the edges of the spectrum. In addition, since the spectra are not flux calibrated, it is important that the continuum region around the line can be well characterised for easy removal. This doublet is smeared by the kinematics to appear as one absorption line in the galaxy. In the templates, where the slit was considerably narrower and the spectra were obtained from individual stars, the two lines are distinguishable. When the template spectra are Gaussian smeared

to fit to the galaxy, the lines will combine. Thus, it is reasonable to use a smeared doublet to measure the kinematics. Similarly, the Mgb and FeI absorption lines in Order 5 are well sampled, and consistency between the three leads to more robust kinematic results.

There are suggestions in the literature that the Nad absorption doublet is contaminated by neutral gaseous sodium in the galaxy ISM (Sparks et al. 1997). This contamination manifests itself as narrow features with equivalent widths correlated with the ISM density, and show similar kinematics to the stellar component. If Nad is to be used for the analysis, these narrow lines need to be shown not to contaminate the stellar lines.

Galactic absorption lines are the sum of individual stellar absorption lines, convolved with their spatial distribution (see Appendix A). The first and second order moments of the velocity distribution function (averaged over observing aperture) can be measured by comparing the spectra with template stellar spectra from stars in the Milky Way. By comparing these at a range of radii from the galaxy centre, the line-of-sight rotation curve and velocity dispersion profile can be constructed. One would expect to see both dispersion and rotation in an early-type spiral such as 2237+0305 with prominent bulge and disk components. In an axisymmetric galaxy, the minor axis rotation curve should exhibit significantly less rotation than the major axis since the line-of-sight streaming motion is negligible (rotation occurs in the plane of the sky rather than along the line-of-sight if the minor axis is due to inclination of a disk).

The Gauss-Hermite Pixel Fitting Software of R. P. van der Marel (can be obtained from http://www-int.stsci.edu/∼marel/software/pixfit.html) is employed to determine the kinematic properties along both the major and minor axes. This software and the principles underlying it are presented in Appendix A, including discussion of the preparation of the stellar templates and the galaxy spectra.

3.4.1 Gaussian fitting parameters

The template and galaxy spectra are now able to be compared using the iterative fitting method described in Appendix A. Initially, the spectra will be compared with templates of individual stellar types to identify the dominant stellar species. Subsequently, linear combinations of templates can be used to find the best-fitting solution.

Poly order	$\overline{\chi^2}$	$\sqrt{<(\chi^2)^2>}$
2	743	324
3	574	215
4	545	206

Table 3.3: Average and standard deviation of the χ^2 fit statistic for three continuum polynomial orders (Nad line, HR22 template). Orders three and four both fit well compared with order two, as expected.

Major axis

The Mgb, FeI and Nad absorption features have high signal-to-noise ratios and can be used for kinematic analysis. The variable parameters used to find the best-fitting (lowest χ^2) solution are the order of the polynomial fit to the continuum and the spectral type used as the template, as described in Appendix A. Since the Mgb and FeI lines have different equivalent widths, a separate fit must be made to both, as otherwise the line strength, γ, will balance itself artificially between the two real values.

The rotation curves for both echelle orders were found to be quite robust to parameter variations, however the velocity dispersion profile varies significantly ($> 3\sigma$ in some cases) to warrant a search of parameter space for the best fit. In addition, the fits to the FeI line were found to be contaminated — Figure 3.13 displays the best-fitting profiles and shows their poor quality. The source of the contamination in the line is unknown, but is probably related to the quasar spectrum interfering with the galaxy's spectrum. (Figure 3.21 shows the spectral environment for both the FeI and Mgb lines are filled with other unidentified spectral features. These other features both confuse the fitting routine, and most likely also affect the line edges, thereby altering the measured dispersion.) The FeI line will therefore not be used in the analysis.

Figure 3.14 shows the fits using the Nad line, with the HR22 template and three different polynomial orders — two, three and four. The line centre seems to be accurately measured in all, evident from the robust rotation profile, but inaccuracies in the continuum fitting fail to reproduce the line shape properly. As expected, the order 2 polynomial is not able to produce an acceptable fit due to its shape limitations. Table 3.3 lists the χ^2 for these three fits. Clearly, orders three and four produce the best results. Figure 3.15 displays an example of a fit overlaid with the original data, for

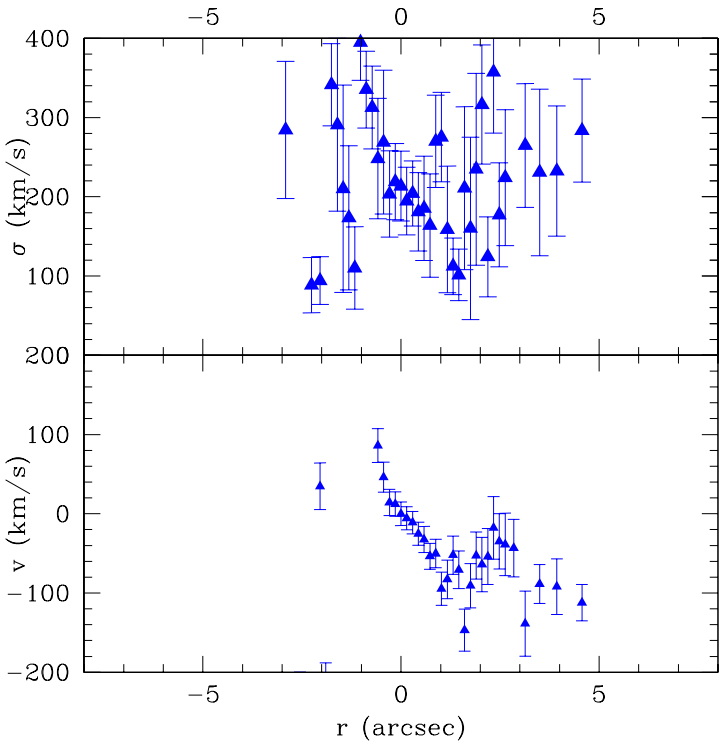

Figure 3.13: Rotation curve and velocity dispersion profile for the FeI line (template HR14) showing the poor quality of the results. The line appears to be contaminated, probably by the quasar spectrum.

polynomial order of four.

Variation of the spectral template also produced varying dispersion profiles. Clearly, the most physically reliable fits will occur for spectral templates that reflect the dominant sources of stellar light in the galaxy — in this case, massive red stars from the bulge. As the templates are drawn from consecutive stellar types, one would expect them all to form a continuum of goodness-of-fit, and for a combination of several to produce the best fits.

Each spectral template will be used to determine the kinematic profiles and their χ^2 statistics compared, before a linear combination of the best-fitting templates is employed to further improve the fit.

Figures 3.16 and 3.17 display the disparity between results for different templates for the Nad and Mgb lines respectively. Again, the rotation curves are quite robust, but the dispersion profiles vary dramatically. Table 3.4 lists the average and standard deviations of the χ^2 for the different

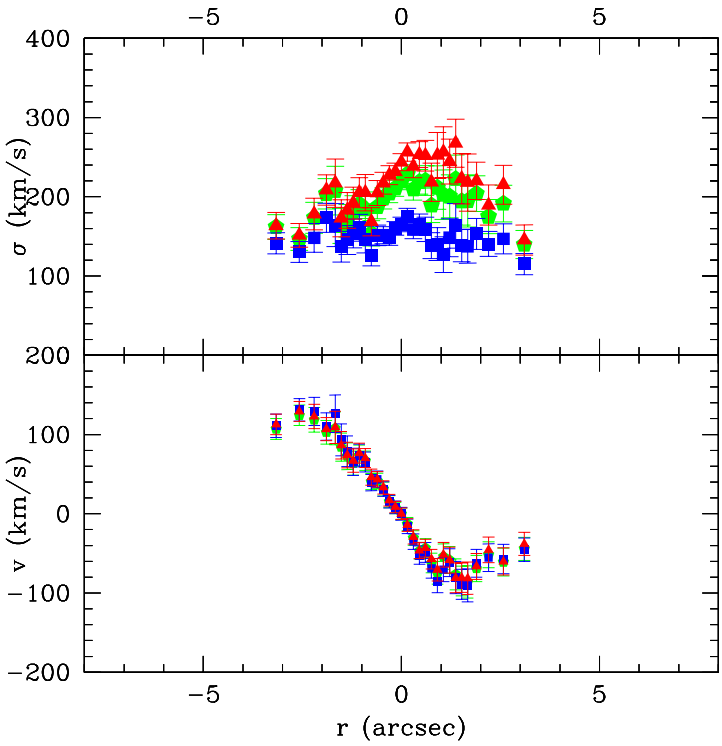

Figure 3.14: Rotation curves and velocity dispersion profiles for the Nad line and the HR22 spectral template for three different continuum polynomial orders (blue squares=2, green pentagons=3, red triangles=4). The rotation curve differs very little, but the dispersion profile changes significantly due to inaccurate reproduction of the line shape.

templates. Each order has a different number of degrees of freedom to compare with the χ^2, as different wavelength ranges were used. In general, N is the number of pixels in the spectrum used for the fit, minus the fitting parameters — three for the continuum polynomial fit, and one each for the overall normalisation, a, and the line strength, γ, (see Eqns [A.1]–[A.2]),

$$N = \Delta\lambda - L - 2, \tag{3.1}$$
$$= 800 - 3 - 2 = 795 \quad \text{(Mgb)}, \tag{3.2}$$
$$= 1200 - 3 - 2 = 1195 \quad \text{(Nad)}, \tag{3.3}$$

where L is the Legendre polynomial order. All of the fits produce reduced

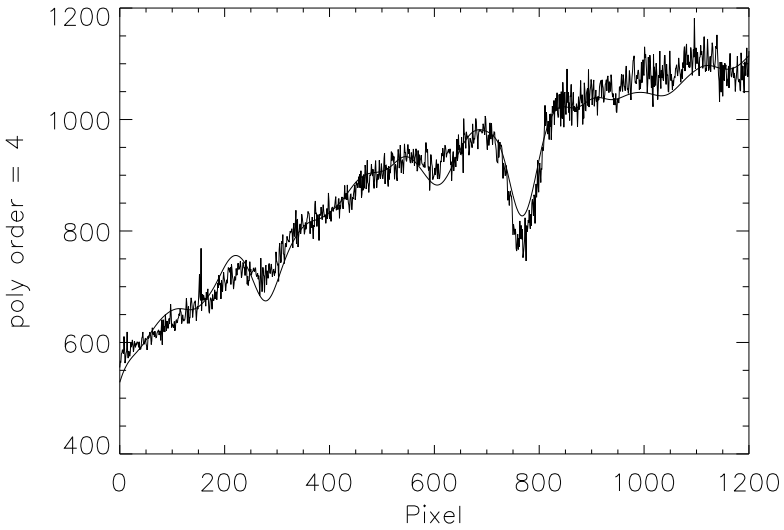

Figure 3.15: Original galaxy data and overlaid spectral template fit for the Nad absorption line for a continuum polynomial order of four and the HR22 template (middle of the range of best-fitting templates). The line shape is not well fitted.

Template	Stellar Type	Mgb $\overline{\chi^2}$	Mgb $\Delta\chi^2$	Nad $\overline{\chi^2}$	Nad $\Delta\chi^2$
HR14	K2III	200	61	504	192
HR19	K0III	209	62	598	227
HR224	K5III	200	61	494	191
HR22	G9III	204	62	574	215
HR279	G7III	210	62	614	235
HR40	G0III	215	63	585	221
HR4	G5III	215	63	613	235
HR60	G8III	226	65	611	234

Table 3.4: Average and standard deviation of χ^2 statistic for each template applied to the two spectral orders, Mgb and Nad.

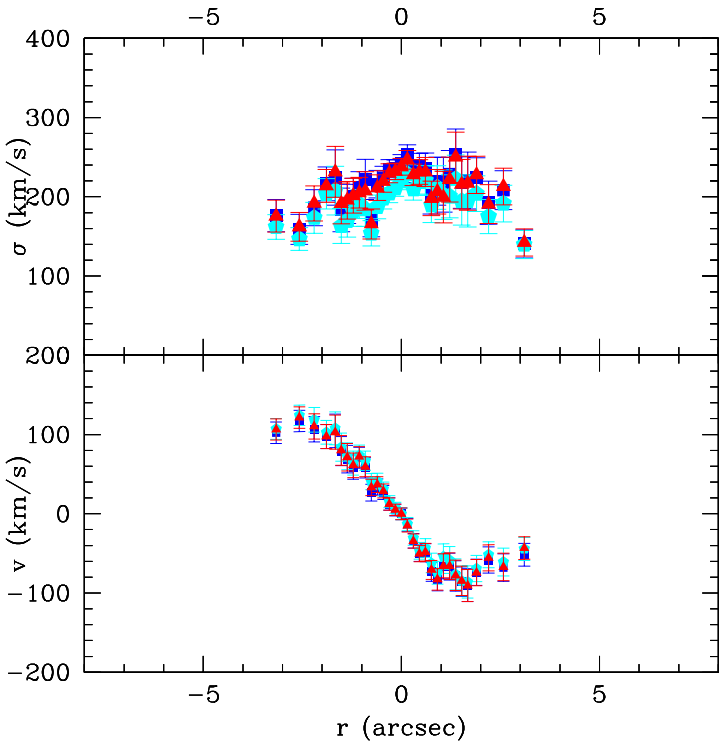

Figure 3.16: Comparison between three stellar templates for results from the Nad line (S/N=5, polynomial order=3). These templates correspond the best-fitting solutions — HR22 (cyan pentagons), HR14 (blue squares), HR224 (red triangles).

χ^2 values less than one. This is not surprising since Equation (3.1) overestimates the degrees of freedom in the system because neighbouring pixels are correlated on the CCD by the Gaussian smoothing applied earlier. As a rough estimate, N should be reduced by $\sim$2.9, since this is the smearing applied to the spectra (see Appendix A). The templates with the same unknown N, however, can be compared with each other, and linear combinations chosen to find the best-fitting profiles.

Two of the solutions for the Nad line fit the data better than the others. Figure 3.18 displays the χ^2 profiles, as a function of galactic radius, for the three best solutions, demonstrating the superiority of the lowest two in reproducing the kinematics in the centre of the galaxy. Reassuringly, these best two also produce the best fits for the Mgb line. A linear combination of the best three is the obvious first choice for attempting a solution that is

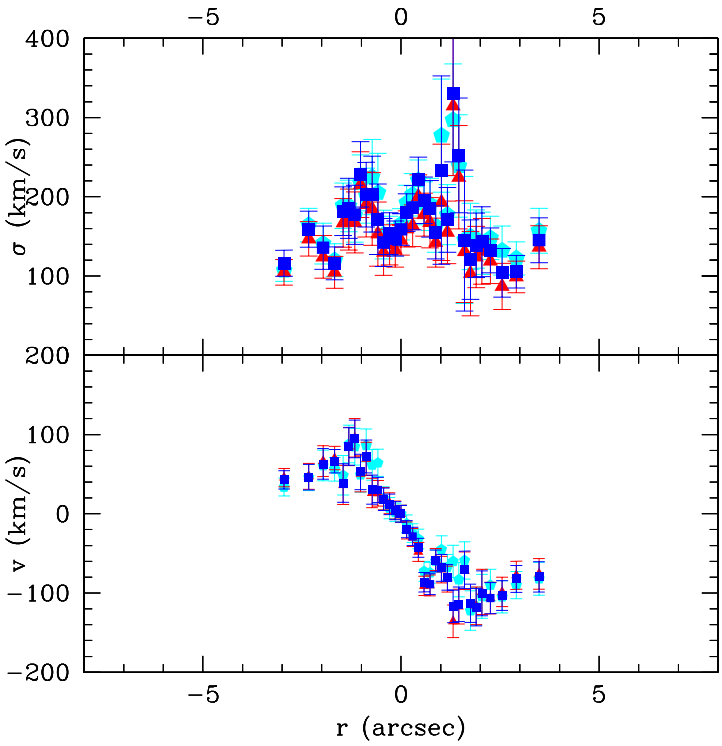

Figure 3.17: Comparison between three stellar templates for results from the Mgb line (S/N=5, polynomial order=3) showing the variation in the dispersion profile (particularly). The templates are HR22 (cyan pentagons), HR14 (blue squares), HR224 (red triangles). The wide dispersion in points at $\sim 1''$ is likely due to contamination from the quasar image.

better again, for both spectral orders. Note that these stellar types are the colder of the eight templates used here, which is expected due to the older stellar population. The worst fitting templates are for hotter stars which are not represented in the bulge of this galaxy.

A combination of the three best-fitting templates are constructed, with equal weightings for each, and profiles fit to them. For both spectral orders the χ^2 is not significantly improved — for the Nad line, it is slightly worsened ($\overline{\chi}^2_{\rm Nad} = 511$, $\overline{\chi}^2_{\rm Mgb} = 312$). A better weighting would promote the importance of the HR14 and HR224 templates, and reduce that of the HR22, however, the range of χ^2 is so small and they all obey $\chi^2/N \leq 1$ that all fits are acceptable and similar (fits where one or more of the points did not converge are not considered satisfactory).

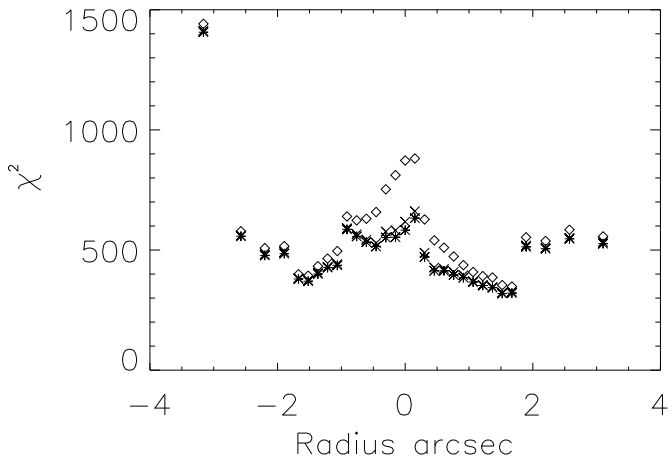

Figure 3.18: Radial profiles of the χ^2 statistic for the three best-fitting solutions for the Nad line, HR14 (K2III, cross), HR224 (K5III, asterisk) and HR22 (G9III, diamond). The best two clearly reproduce the central kinematics better than the others.

For a final comparison, the correct location of the galactic centre must be determined. Until now, the centre has been taken as the pixel containing the maximum of the light profile, but this is only accurate to a few tenths of an arcsecond. Kinematic data from the two sides of the galaxy could be compared for symmetry, but this would assume a symmetric galaxy — unlikely given the complex system 2237+0305 is known to be. Instead, the light profiles (e.g. Figure 3.2) will be fit with Gaussians and the centroid taken as the galactic centre. The values will vary between orders and within orders, as the slit projection on the CCD varies with position.

Figure 3.19 displays the light profile in Order 5 at the wavelength of the Mgb absorption line, and the Gaussian fit to the profile. The central regions are contaminated by quasar light, as discussed earlier, but the outer edges fit well. This feature gives confidence in the fit. The Gaussian centre lies at pixel 68.87, corresponding to a shift of 0.13″ from the assumed centre. Similarly, the Nad shift is –0.10″.

Figure 3.20 compares the shifted rotation curves and dispersion profiles for the Mgb and Nad lines. The rotation curves provide a satisfactory fit to one another, but the dispersion profiles are quite disparate. The Mgb profile

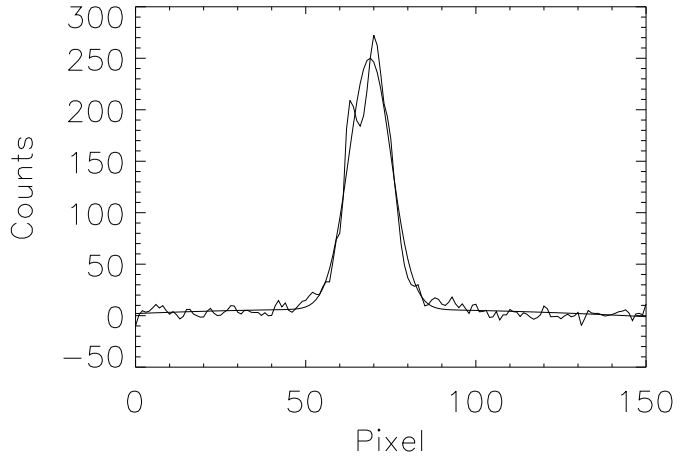

Figure 3.19: Light profile in order 5 at the wavelength of the Mgb absorption line, and the Gaussian fit to the profile. Although the inner regions are contaminated by the lensed images, the outer regions fit well. The centroid lies at pixel 68.87.

shows systematically lower line-of-sight velocity dispersion than the Nad, except at the quasar image locations, where the Mgb is clearly contaminated. The Nad results are more uniform over the radius range, suggesting they are more robust than the Mgb. In addition, the spectral environment of the Mgb line has a concentration of other spectral features that may be contaminating the signal (the Nad line, on the other hand, is located in a smooth part of the spectrum). Like the FeI line, these other features may be affecting the line shape by impinging on the line wings. Figure 3.21 shows an example section of the spectrum ($\sim$40Å wide) and fit for both the FeI (top) and Mgb (bottom) lines, close to the galactic centre. In both spectra, there are other absorption features close to the line to be measured. The fits to both lines are affected by the presence and proximity of the other features and the spectrum in these regions can therefore be classified as suffering from confusion.

The disparity between the results for these two absorption lines, and the poor fit to the line profile shown in Figure 3.15, suggests a better analysis is required. In an attempt to do this, the wavelength range over which the profile is measured will now be limited to only contain the line. This will

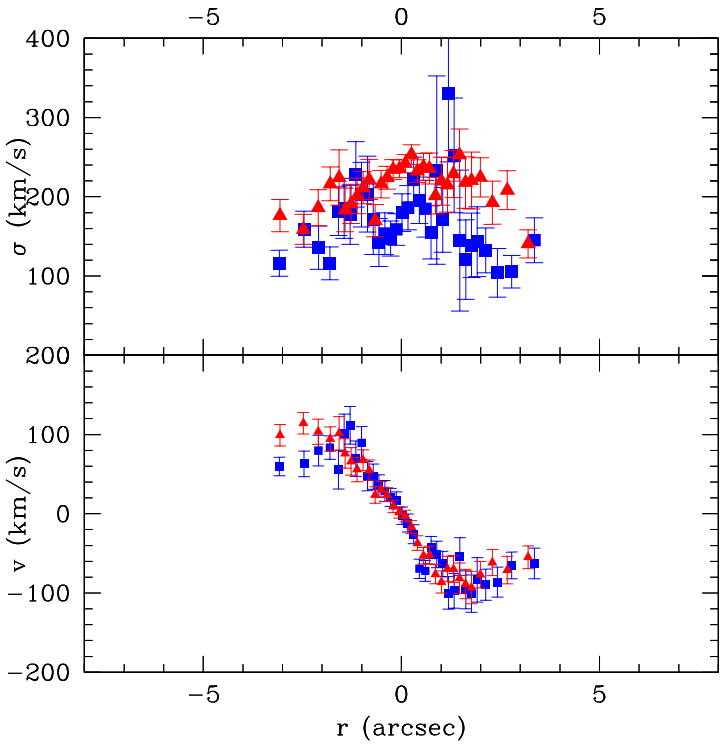

Figure 3.20: Best-fitting rotation curves, shifted to the best-fitting spatial centroid and zeropoint velocity, for the two spectral orders (Order 5 blue squares, Order 6 red triangles). The central rotation curves fit well, but the outer regions are more disparate, possibly reflecting some contamination in one or both of the absorption lines. The dispersion profile has similar attributes.

remove any contamination in the surrounding continuum. In addition, since the Nad line has the best signal-to-noise ratio, has thus far produced more stable results, and does not lie in a section of the spectrum with confusion, it will be concentrated on alone.

A first order polynomial is fit to the continuum since it is effectively linear over this region (300 pixels, $\lambda = 6110 - 6180$Å). The radius range is also extended beyond the region where the galaxy signal is obvious in order to include as much information as can be obtained from the data.

Only the four best-fitting templates are fitted to the spectrum, since these clearly represent the bulk of the stellar emission, and bin the data radially to $0.6''$ bins, in order for the points to be statistically independent

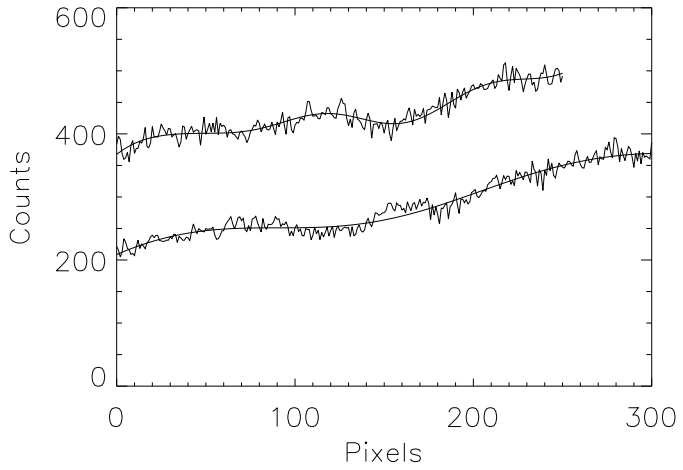

Figure 3.21: Spectra and fits to the FeI (top) and Mgb (bottom) lines within a few hundred pixels (∼40Å) of the line centres. In these regions, the location and shapes of both lines are confused by other spectral features in close proximity.

($0.6''$ is the resolution of the observations). Figure 3.22 displays the χ^2 statistic as a function of radius for the four templates. Clearly the outer points do not produce good fits — beyond $r{\sim}4''$, the galaxy signal is lost in the noise. The four templates produce almost equally good fits in the central regions of the galaxy. Similarly, a by-eye inspection of the fit to the absorption line (Figure 3.23, HR22 template) shows its clear improvement over the earlier results (Figure 3.15). The stability and accuracy of the kinematic results have improved — all templates produce similar fits and, more qualitatively, the fits look to the eye to be reproducing the line shape faithfully. Limiting the wavelength range to include only the absorption line has removed any features in the surrounding continuum that did not have kinematics matching the stellar motions (e.g. quasar lines).

The rotation curve and dispersion profile for the constrained wavelength range, after correction for the position of the galactic centre, can be plotted for each template. Figure 3.24 shows these curves, and demonstrates the equivalence of the templates — their results are consistent with each other (note that the radius axis range has increased from previous plots). Within the region where the galaxy has reasonable signal ($r < 4''$), the rotation

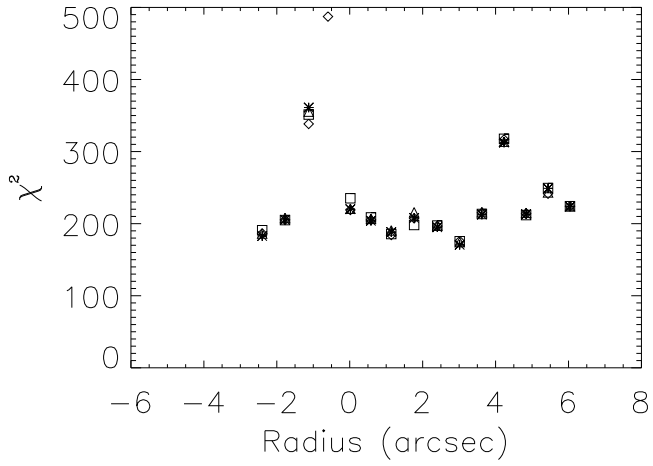

Figure 3.22: χ^2 distribution for fits of the four best-fitting templates to the Nad line for the major axis. All four templates appear to produce equally good fits. The symbols denote the HR22 template (diamond), HR224 (asterisk), HR14 (triangle), HR19 (square).

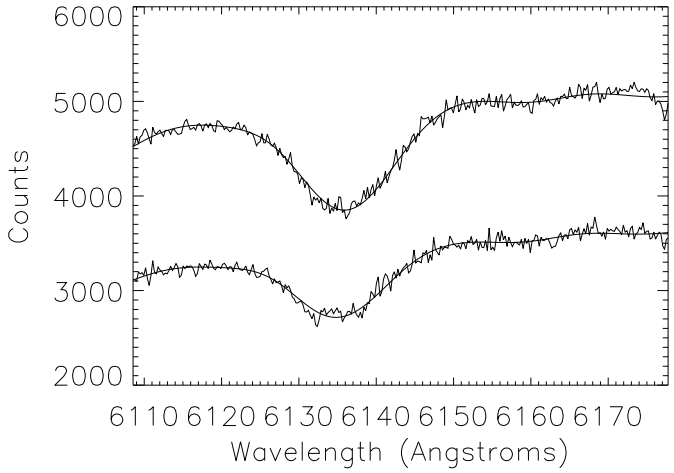

Figure 3.23: Data and fits to the Nad line using the HR22 template for two of the highest signal-to-noise radial bins. The fits clearly reproduce the line shape more accurately than the earlier results, shown in Figure 3.15.

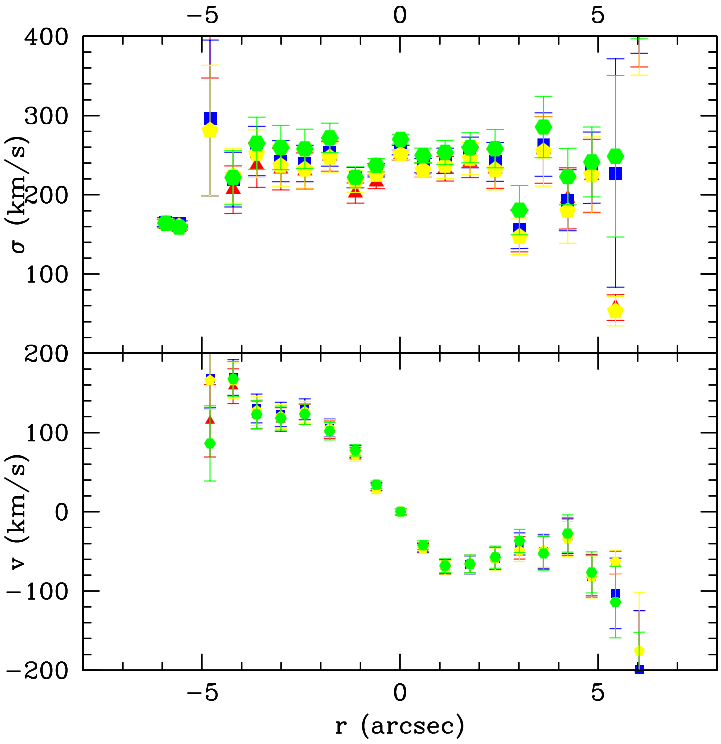

Figure 3.24: Major axis kinematic results for the four best-fitting templates and with the wavelength range constrained to sample only the Nad absorption line. The templates produce consistent results for the region where there is adequate signal and large errors otherwise. The flatness of the dispersion profile is encouraging. The symbols denote the templates HR22 (red triangle), HR224 (blue square), HR14 (yellow pentagon), HR19 (green circle).

curves and dispersion profiles are consistent, within errors. In addition, the dispersion profile is roughly flat, suggesting the true kinematics are being reproduced accurately (the points are now independent) — physically, the dispersion profile does not need to be flat, but the fact that it is suggests that the kinematics for the independent points are being faithfully reproduced. The rotation curves are symmetric within errors. These four curves will be averaged to produce the final major axis results.

Relying on the Nad line exclusively is potentially dangerous, given the possible contamination discussed in Section 3.4. However, given the consistency with past results (Foltz et al. 1992) for the central velocity dispersion,

the smoothness of the spectral feature, the small wavelength range used to minimise contamination, and the quality of the fit using a Gaussian alone, there does not appear to be cause for concern.

Minor axis

The analysis of the minor axis data is similar to that performed for the major axis. In this case, one would expect less rotation to be present, but a reasonably similar dispersion profile. Some rotation is expected since the slit is placed 12° off of the minor axis, the slit is sufficiently wide as to include stars on many parts of their (assumed) circular orbits (disk), and the bulge component is expected to have more isotropic orbits.

The same wavelength ranges as were used for the major axis are used for the minor axis, and so a direct comparison of the χ^2 values is possible. An order 3 polynomial was again employed initially for the continuum fitting, and each template stellar spectrum applied to the data to determine the kinematics.

All templates produce poor quality curves for the Mgb and FeI lines, particularly at radii, $r < 0$. Figure 3.25 displays the best-fitting rotation curve and dispersion profile for the Mgb and FeI lines along the minor axis. The dispersion uncertainties are very high and the rotation does not resemble the shape expected from a rotating galaxy.

The Nad line produces smooth curves with a rotation gradient and flat dispersion profile across the galaxy. Given this and the poor results for the FeI and Mgb lines, Nad will be used in the following analysis. The χ^2 values show excellent agreement at all radii except the outer few, which produce unreasonable values ($\sim 10^4$). As such, these outliers are removed from the χ^2 comparison, as they skew the results and don't allow sufficient discriminating power in the central regions. Table 3.5 lists the χ^2 values for the best-fitting solutions for each template. For the Nad line, the HR14 and HR224 templates once again are the preferred stellar type. (Note that the results with outliers included also show similar trends). As for the major axis, the three best-fitting templates, HR14, HR224 and HR22, are linearly combined in an attempt to find a better solution, but no improvement is found compared with the results for the HR14 template alone.

The centre of the galaxy and velocity zero point are found in a similar way to the major axis. Figure 3.26 displays the best-fitting profiles after

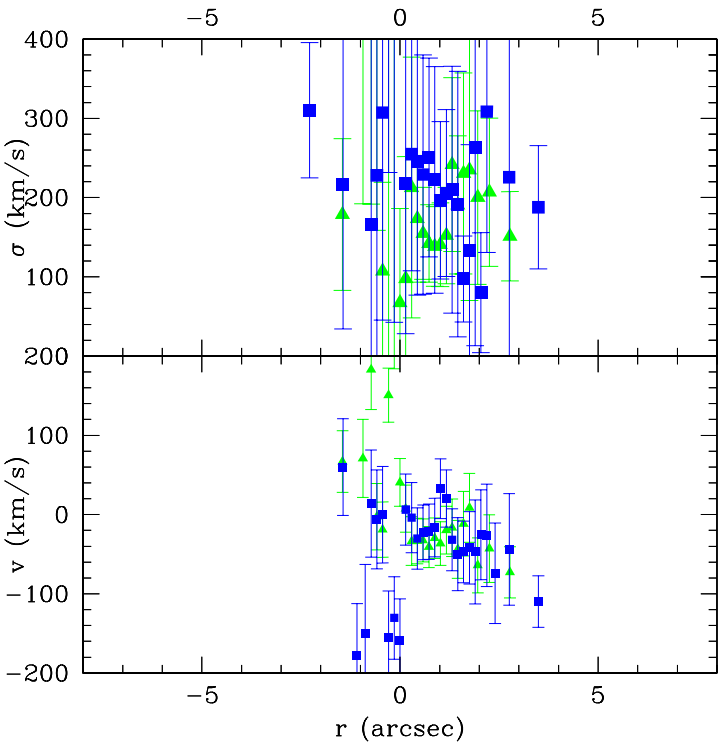

Figure 3.25: Minor axis rotation curve and velocity dispersion profile for the best-fitting stellar template (HR14) for the Mgb (green triangles) and FeI (blue squares) absorption lines. There is clear contamination occurring at $r < 0$, and the dispersion profile uncertainties are very high.

Template	Stellar Type	Nad $\overline{\chi^2}$	Nad $\Delta\chi^2$
HR14	K2III	118	64
HR19	K0III	128	64
HR224	K5III	117	65
HR22	G9III	126	64
HR279	G7III	130	64
HR40	G0III	127	64
HR4	G5III	131	64
HR60	G8III	130	64

Table 3.5: Average and standard deviation of χ^2 statistic for each template applied to the Nad line for the minor axis.

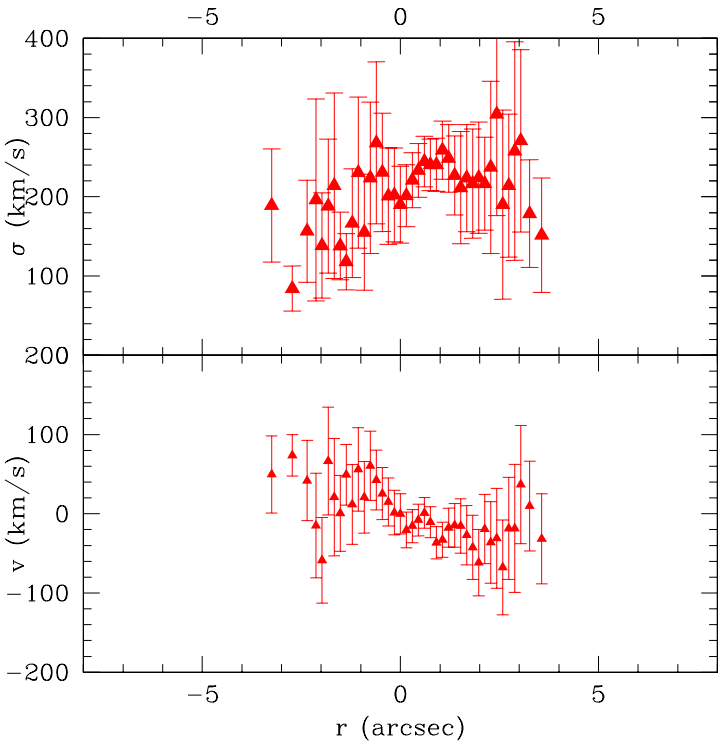

Figure 3.26: Minor axis rotation curve and velocity dispersion profile for the best-fitting stellar template (HR14) for the Nad absorption line, after solving for the galactic centre using a Gaussian profile. The contamination seen in the Mgb results are not visible here, however the profile uncertainties are still very high.

shifts. The contamination that is evident in the Mgb/FeI results are not visible here, however the uncertainties are still very high on both the rotation curve and velocity dispersion profiles. Some rotation is visible in the rotation curve, as expected, but not at the level of the major axis. The central line-of-sight velocity dispersion is also consistent between the major and minor axis (for the Nad line), $\sigma_c \simeq 220$ kms^{-1}, which is encouraging, and compares well with the result from Foltz et al. (1992) of $\sigma_c \simeq 215\pm30$ kms^{-1}.

To improve the results, as with the major axis, the wavelength range is reduced to just sample the Nad line and the data are binned to the resolution of the observations. Again, the four best-fitting templates produce consistent results and the uncertainties are reduced from those for the larger wavelength range. Figure 3.27 shows the four template rotation curves and

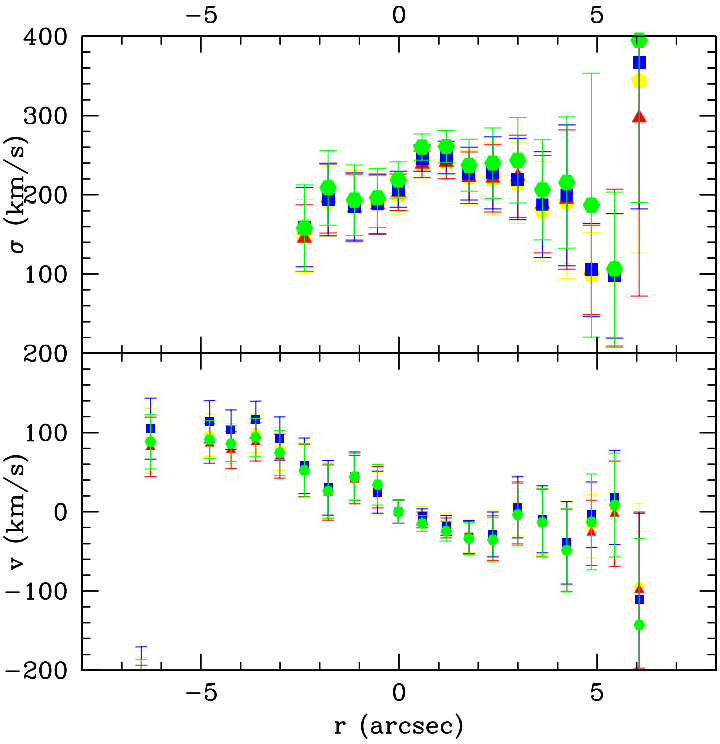

Figure 3.27: Minor axis kinematic results for the four best-fitting templates and with the wavelength range constrained to sample only the Nad absorption line. The templates produce consistent results, but outlying points are severely affected by the lack of galaxy signal beyond $r{\sim}0.6''$ and are therefore removed. Symbols are as for Figure 3.24.

dispersion profiles. The general shape of the earlier results is retained, but the data are much cleaner and the uncertainties reduced to the level found for the major axis. There are a lot of data omitted from this figure, due to the poor fits at these radii (low signal-to-noise produced double dips that the software tried spuriously to fit). The consistency between templates and the matching of the velocity dispersion in the central regions with that from the major axis, provide confidence in the results. As expected, the rotation is of a smaller magnitude than the major axis, but shows a definite trend of increasing rotation with radius and a flattening beyond a few arcseconds.

3.5 Results

3.5.1 2237+0305 rotation curve & velocity dispersion profile

The results from the above analysis can be now presented as the rotation curve and line-of-sight velocity dispersion profile for the major and minor axes. The results for the four best-fitting templates are averaged (since they are so similar, a simple average is justified) to produce the final fits. Figure 3.28 displays the fits and their uncertainties.

3.6 Conclusions

In this chapter data from the ESI echelle instrument on the Keck telescope were used to measure the major and minor axis kinematics of the galaxy 2237+0305. Three stellar absorption lines were used for measurement — FeIb, MgIb and Nad — but the former two were found to be contaminated, most likely by quasar spectral features at their wavelengths, and were not used in the final analysis. The spectra of eight nearby stars, with contiguous spectral type matching those expected in a galactic bulge (and matching the $(g-r)$ colour measured by Yee 1988), were used as templates against which the observed galaxy spectrum was matched. The Nad absorption line centre (rotation) and line width (velocity dispersion) were measured using these templates as calibration. The colder templates (spectral types G9III-K5III) were found to fit the line profile most accurately and their results were combined for the final measurement. Kinematics were obtained in a radius range from the galactic centre to $\sim 5''$, except in the minor axis dispersion profile where low signal-to-noise affected results on one side of the galaxy. These results will be used in the distribution function analysis presented in the next chapter to constrain the mass distribution of 2237+0305.

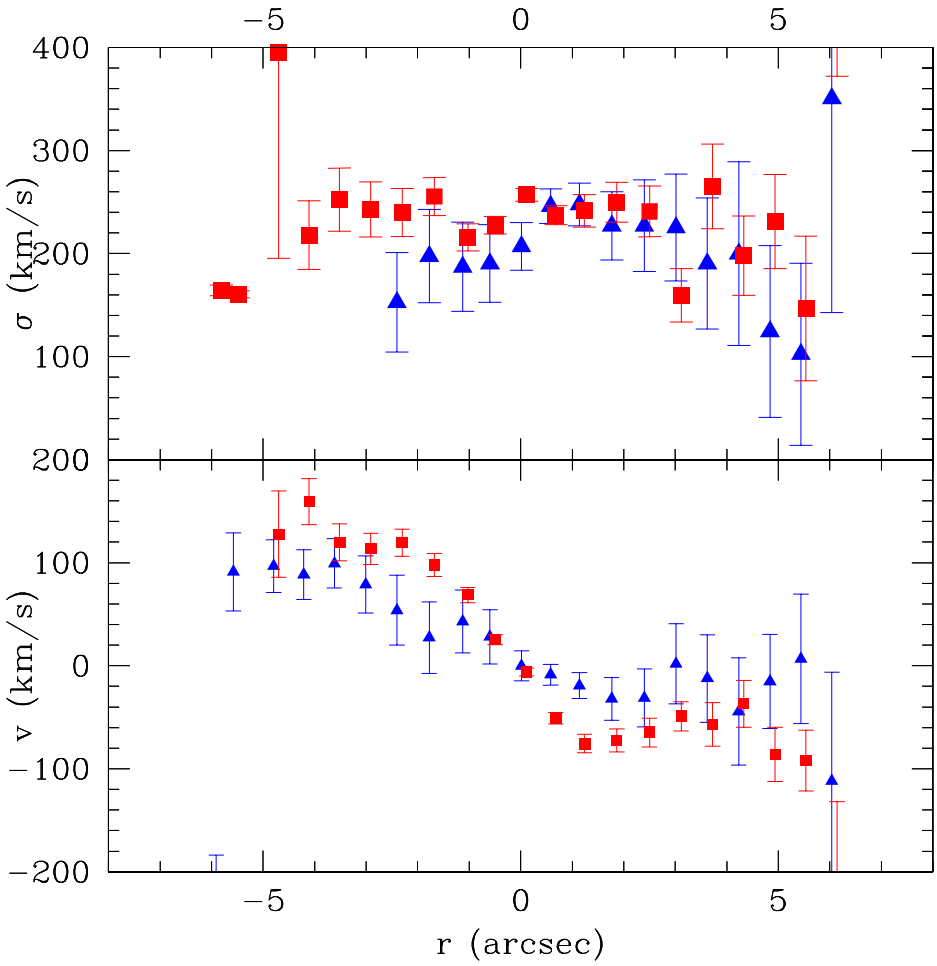

Figure 3.28: Final rotation curve and velocity dispersion profile for the major (red squares) and minor (blue triangles) axes of 2237+0305. The large error bars far from the galactic centre reflect the lower signal-to-noise in these regions.

CHAPTER 4

Mass Distribution of 2237+0305

The kinematic results from Chapter 3 are applied to modelling the galaxy 2237+0305. A combination of photometric, kinematic and lensing information is used to construct a mass model for the four major mass components of the system — the dark matter halo, bulge, disk and bar — plus an external shear due to perturbers along the line-of-sight. For the kinematic comparison, the bulge is modelled as a spherical system with a velocity anisotropy to mimic the observed flattening. The best-fitting solution is not a statistically acceptable fit to the data, suggesting an improved kinematic model is required. The best-fitting solutions favour a bulge with slightly tangentially anisotropic orbits and a softened isothermal-like dark matter halo.

4.1 Galaxy distribution function

In Chapter 2, where the mass distribution of 2237+0305 was modelled, it is argued that kinematic information breaks the remaining degeneracies between models. The high quality kinematic information obtained using the Keck telescope, presented in Chapter 3, can be applied to constrain the mass distribution.

Instead of constructing mass models and matching them to the lensing and kinematic data, the best approach is to construct complete phase space distribution functions (DF) of the mass components that fit all of the data simultaneously. Unfortunately, constructing DFs for flattened systems with mass components with different position angles is extremely difficult. However, since previous models have suggested the bulge component provides most of the lensing convergence and pressure support in the centre of the galaxy, its DF will be modelled to properly calculate the kinematics. The other components are modelled as they were in Chapter 2. This method provides a more realistic mass model since the spatial and velocity structure are intimately related from the outset, rather than combined *a posteriori*.

Spherically symmetric and static systems can have quite simple DFs that depend only upon the energy, E, of the system. Since the DF is a function of the integrals of motion of the system, Jeans' Theorem states that it must be a solution of the Boltzmann equation (Binney and Tremaine 1987). A spherical system has the energy and the three components of the angular momentum as integrals. In an axisymmetric system, the integrals are the energy and one component of the angular momentum. For a more general system with triaxiality, for example, the DF can be a complicated function, and the total energy may be the only integral. Real galaxies are rarely well fitted by an analytic functional form for the DF, but much work has been done to construct those that fit the components of real galaxies sufficiently.

4.1.1 Distribution function models

The distribution function for a system completely describes its structural and kinematic properties. The function, f, is the mass per unit spatial volume per unit momentum volume in the system. With a knowledge of the DF, the entire history and future of the system can be obtained by time evolution.

Where the DF depends solely on the energy, E, the mass density, $\rho(r)$, can be found via,

$$\rho = 2^{5/2}\pi \int_0^{\psi} f(\epsilon)(\psi - \epsilon)^{1/2}\, d\epsilon, \tag{4.1}$$

where $\psi = -\Phi$ is the gravitational potential, and $\epsilon = -E$, is the energy (Tremaine et al. 1994). From this expression, it is clear that the total DF can be constructed from a linear combination of individual component DFs, the same as the total density. Inverting this expression gives Eddington's formula (Binney and Tremaine 1987; Eddington 1916) for the DF in terms of the mass density function, ρ,

$$f(\epsilon) = \frac{1}{2^{3/2}\pi^2}\frac{d}{d\epsilon}\int_0^{\epsilon}\frac{d\rho}{d\psi}\frac{d\psi}{(\epsilon - \psi)^{1/2}} \tag{4.2}$$

where $\rho = \rho(\psi)$ (the 'augmented density') is the density written as a function of the potential alone.

Moments

The moments of a spherical distribution are defined as,

$$\mu_{ijk}(r) = \int\int\int f(r, \mathbf{v}) v_r^i v_\theta^j v_\phi^k \, d\mathbf{v}, \tag{4.3}$$

where $\mu_{000}(r)$ denotes the density, $\rho(r)$, and acts as the normalisation for the moments, and the integrals extend over all momentum space. Given this definition, the mean and variance (the square of the velocity dispersion) of the velocity in the radial direction are,

$$\overline{v_r(r)} = \frac{\mu_{100}}{\mu_{000}} = \frac{\int f(r, \mathbf{v}) v_r d\mathbf{v}}{\int f(r, \mathbf{v})\, d\mathbf{v}}, \tag{4.4}$$

$$\sigma^2(r) = \overline{v_r^2(r)} = \frac{\mu_{200}}{\mu_{000}} = \frac{\int f(r, \mathbf{v}) v_r^2 d\mathbf{v}}{\int f(r, \mathbf{v})\, d\mathbf{v}}, \tag{4.5}$$

assuming $\overline{v_r} = 0$. When the system is spherically symmetric and isotropic, the velocity dispersion is more easily calculated using the equation of hydrostatic equilibrium (Tremaine et al. 1994),

$$\frac{d(\rho\overline{v_r^2})}{dr} = -\rho\frac{d\Phi}{dr}. \tag{4.6}$$

If a uniform velocity anisotropy is included in the modelling, these equations can be extended. Binney and Tremaine (1987) define the anisotropy parameter, β_a, via

$$\beta_a(r) = 1 - \frac{\sigma_\theta^2}{\sigma_r^2}, \tag{4.7}$$

where σ_θ and σ_r are the angular and radial velocity dispersions, respectively. Here, this parameter will be assumed to be constant with position, although in general it is not.

Hence, varying β_a varies the amount of tangential versus radial motion ($\beta_a = 1$, purely radial; $\beta_a = 0$, isotropic; $\beta_a \to -\infty$, purely tangential). For a spherically symmetric but anisotropic system, the radial velocity dispersion can be calculated from the Jeans Equations with a correction for anisotropy (Lokas et al. 2004),

$$\sigma_r^2(r) = \frac{r^{-2\beta_a}}{\rho(r)} \int_r^\infty x^{2\beta_a} \rho(x) \frac{d\Phi}{dx}\, dx. \tag{4.8}$$

Before these kinematics can be compared with data, the velocity dispersions and rotation curves need to be projected onto the line-of-sight. Tremaine et al. (1994) quote the line-of-sight spherically symmetric velocity dispersion at projected radius R as,

$$\sigma_{\rm los}^2(R) = \frac{2}{\Upsilon I(R)} \int_R^\infty \frac{\rho(r)\overline{v_r^2}(r) r\, dr}{(r^2 - R^2)^{1/2}}, \tag{4.9}$$

where r and R are the spherical and projected radii from the potential centre, respectively, and $\Upsilon I(R)$ represents the mass-to-light ratio times the surface brightness,

$$I(R) = \frac{2}{\Upsilon} \int_R^\infty \frac{\rho(r) r\, dr}{(r^2 - R^2)^{1/2}}. \tag{4.10}$$

When the velocity distribution is anisotropic, geometry shows that there is an extra factor in this expression (Lokas et al. 2004),

$$\sigma_{\rm los}^2(R) = \frac{2}{\Upsilon I(R)} \int_R^\infty \frac{\rho(r)\overline{v_r^2}(r) r}{(r^2 - R^2)^{1/2}} \left(1 - \beta_a \frac{R^2}{r^2}\right) dr. \tag{4.11}$$

Equations (4.8) and (4.11) can be combined to write (Lokas et al. 2004),

$$\sigma^2_{\rm los}(R) = \frac{2G}{\Upsilon I(R)} \int_R^\infty \frac{r^{1-2\beta_a}}{\sqrt{r^2-R^2}} \left(1 - \beta_a \frac{R^2}{r^2}\right) \int_r^\infty x^{2\beta_a - 2} \rho(x) M(x)\, dx dr \tag{4.12}$$

which expresses the line-of-sight velocity dispersion for a system with an anisotropic velocity tensor. This can be reduced to a one-dimensional numerical integral by changing the order of integration and using the hypergeometric function (see Appendix B for a full derivation).

Binney and Tremaine (1987) describe the calculation of the rotation speed, v_c, in the presence of a uniform anisotropy,

$$v_c^2(r) = -\sigma_r^2 \left(\frac{d\ln\rho}{d\ln r} + \frac{d\ln\sigma_r^2}{d\ln r} + 2\beta_a \right). \tag{4.13}$$

which can be projected onto the line-of-sight and compared with the measured rotation curve.

These expressions allow one to take a spherical density profile for a mass component and calculate the expected anisotropic kinematics. They will be applied to the bulge component.

4.2 Mass models

Given the larger number of degrees of freedom in the problem with the addition of kinematic information, one can accommodate more flexibility in the models for the mass components. There is no reason to change the modelling of the disk (exponential surface density) and bar (Ferrers ellipse), since these are standard profiles that have worked well in previous work. The distribution of dark matter, however, remains unknown, and a more general profile can be fit to it. In addition, an external shear can be included in the solution of image positions to accommodate the influence of external perturbers along the line-of-sight. From the work of Rauch et al. (2002), we know that there are a number of absorption systems between the lens and quasar source that may affect the image positions. In addition, other unknown mass concentrations can have a small, but important impact on image positions — shear strength, $\gamma_{\rm ext} \sim 0.01$–$0.1$, for most lenses (Witt and Mao 1997), and Wucknitz (2002) finds $\gamma_{\rm ext} \lesssim 0.13$ for 2237+0305, based upon requiring H_0 to be positive.

The model chosen for the bulge component needs to be as simple as possible, for tractability, while retaining the key features that are required for both the lensing to reproduce the image positions, as discovered through the analysis of Chapter 2, and the kinematics to reproduce the spectroscopic observations. In previous work, and following that of Schmidt (1996), the bulge can be modelled successfully to follow a de Vaucouleurs surface brightness profile, with a flattening. More generally, the de Vaucouleurs profile is one of a class of profiles called Sérsic profiles (Sérsic 1968) where,

$$I(R) = I_0 \exp\left[-b_m (R/r_b)^{1/m}\right], \tag{4.14}$$

is the surface brightness distribution, r_b is the characteristic scale length, and b_m is a constant. Clearly, the de Vaucouleurs profile corresponds to $m = 4$, with an appropriately scaled r_b [see Equation (2.1)].

Lima Neto et al. (1999) and Lokas et al. (2004) present volume deprojections of the circularly symmetric Sérsic profile. These expressions allow one to use the kinematic expressions for the rotation speed and line-of-sight velocity dispersion, presented in Equations (4.13) and (4.12), but are not easily generalisable for a non-spherical density profile, although a flattened bulge component is critical for the lensing. For the kinematics, the spherical Sérsic expression with a constant anisotropy will be used across the bulge to mimic the effect of flattening on the kinematics. Intuitively, the shape of a stellar component must be related to the types of orbits found within it, and hence the anisotropy of the stellar population. Binney (1978) calculates the ratio of the rotation to dispersion speed for elliptical galaxies with given ellipticities (note that this refers to the rotation of the form rather than streaming motions). A back-of-the-envelope calculation presented by Binney shows that the ratio of kinetic energy in the radial and rotational components is a direct function of the axis ratio of the figure. Given that only two axes are measured for the bulge in 2237+0305 (the third is lost in projection), the exact relationship between the ellipticity and anisotropy is *a priori* unknown, however an anisotropic velocity tensor can be used to mimic an ellipticity.

The deprojected Sérsic profile, for general m, is given by,

$$\rho(r) = \rho_0 \left(\frac{r}{a}\right)^{-p} \exp\left[-\left(\frac{r}{a}\right)^{1/m}\right], \quad (4.15)$$

$$\rho_0 = \Sigma_0 \frac{\Gamma(2m)}{2a\Gamma[(3-p)m]}, \quad (4.16)$$

$$p = 1.0 - 0.6097/m + 0.05463/m^2, \quad (4.17)$$

$$a = r_b/(b_m)^m \quad (4.18)$$

where a is a generalised scale length and Σ_0 is the central surface mass density ($= \kappa\Sigma_{\rm cr}$ for connection with the lensing). The mass enclosed within a given radius is easily calculated,

$$M(r) = 4\pi\rho_0 a^3 m \Gamma_{\rm inc}\left[(3-p)m, \left(\frac{r}{a}\right)^{1/m}\right], \quad (4.19)$$

where $\Gamma_{\rm inc}$ is the incomplete Gamma function. In addition, the bulge and bar are constrained to have equal mass-to-light ratios since they contain the same population of stars.

The dark matter halo is modelled with a spherical generalised cusped mass model, with variable inner and outer density slope (Muñoz et al. 2001; Keeton 2001). This profile reduces to a variety of useful models, such as the NFW, Hernquist and isothermal, and has the form,

$$\rho(r) = \frac{\rho_s}{(r/r_h)^\gamma [1 + (r/r_s)^2]^{(n-\gamma)/2}}, \quad (4.20)$$

where γ and n are the inner and outer logarithmic slopes, respectively, and r_h is the characteristic scale length. For a spherical model, the lensing convergence, κ, is given by,

$$\kappa(r) = \kappa_h B\left(\frac{n-1}{2}, \frac{1}{2}\right)(1+x^2)^{(1-n)/2} {}_2F_1\left[\frac{n-1}{2}, \frac{1}{2}; \frac{n}{2}; \frac{1}{1+x^2}\right], \quad (4.21)$$

where $\kappa_h = \rho_s r_h/\Sigma_{\rm cr}$, $x = r/r_h$, B is the beta function and ${}_2F_1$ is a hypergeometric function.

The external shear adds both a convergence (equivalent to a mass-sheet degeneracy) and a shear to the calculation of bending angles. Neglecting the constant surface mass density sheet κ, the potential can be written as

Component	Parameter	Definition
Bulge	κ_b	convergence
	r_b	scale length
	β_a	anisotropy parameter
Disk	κ_d	convergence
	r_d	scale length
DM Halo	κ_h	convergence
	r_h	scale length
	γ	inner slope
	n	outer slope
Bar	κ_{br}	convergence*
Shear	$\gamma_{\rm ext}$	shear strength
	θ_γ	shear angle
Source	β_x	x source position
	β_y	y source position

Table 4.1: Parameters to be fit in the combined lensing and kinematic model of 2237+0305. The ellipticities of the bulge and disk are fixed at their photometric value, and the bar is modelled as in Schmidt (1996) with only a variable M/L. There are 13 parameters in total. (*the bar and bulge mass-to-light ratios are constrained to be equal.)

(Keeton 2001),

$$\psi(r,\theta) = -\frac{r^2}{2}\gamma_{\rm ext}\cos 2(\theta-\theta_\gamma), \tag{4.22}$$

where θ_γ is the direction of the shear (relative to the x-axis) and $\gamma_{\rm ext} = (\gamma_1^2 + \gamma_2^2)^{1/2}$ (see Section 1.3) is the shear strength (dimensionless). The bending angles at each image position can be calculated by taking the gradient of this potential.

The parameters in the model are shown in Table 4.1. There are 13 parameters to fit, including the unknown source position. The constraints include the four image positions, the two HI rotation points and the kinematic information (16 points for each rotation curve and dispersion profile), giving 74 constraints, and therefore 74–13=61 degrees of freedom.

There are, however, reasons to reduce the amount of kinematic information used in the fitting. Firstly, the method used to calculate the velocity dispersions [Equation (4.12)] will assign the same dispersion to both the major and minor axis — the anisotropy is modelled to alter the dispersion, but the alteration is isotropic. This method *will* affect the rotation speed however, since rotation is measured along the line-of-sight and the system is inclined. Hence, the minor axis dispersion data will not be used to constrain

the model.

Secondly, the rotation data are asymmetric from one side of the galaxy to the other. This is not surprising; we know that 2237+0305 has a bar lying at a different position angle to the bulge and disk, and the disk has prominent spiral arms. Hence, fitting a simplified model such as that discussed here will not be able to reproduce both sides of the rotation curve. The data to the left of centre in the plots are better behaved than those to the right — the errors are lower and the curves smoother — and so only these data are used.

Removing the unused data leaves the system with 42 constraints and 13 parameters, giving 29 degrees of freedom. The χ^2 statistic quantifying the goodness of fit for a model is defined as,

$$\chi^2 = \sum_{\text{Images}} \frac{(\theta - \theta_{\text{mod}})^2}{\sigma^2_{\text{images}}} + \sum_{\text{r}_{\text{HI}}} \frac{(v - v_{\text{mod}})^2}{\Delta v^2} \tag{4.23}$$

$$+ \sum_{\text{r}_{\text{Keck}}} \frac{(v - v_{\text{mod}})^2}{\sigma^2_{v,\text{data}}} + \sum_{\text{r}_{\text{Keck}}} \frac{(\sigma_{\text{data}} - \sigma_{\text{mod}})^2}{\sigma^2_{\text{data}}}, \tag{4.24}$$

where the summations are over image positions, HI rotation points, Keck rotation points and Keck velocity dispersion points, respectively. The reduced χ^2, given the large number of degrees of freedom, will be defined as $\chi^2/29$. One aims for a reduced χ^2 of unity for a statistically acceptable fit.

4.3 Construction of kinematic model

To compare the results with the measured data, the effect of aperture size and galaxy inclination need to be taken into account, after the line-of-sight calculation [Equation (4.12)] projects through the galaxy. Since the slit used to measure the spectrum has a finite width and the observations do not have perfect resolution, there will be an area on the sky that contributes to each of the observed kinematical datapoints. Each point will contribute an amount proportional to the surface brightness of the galaxy at that point. The aperture kinematics are therefore calculated in a similar way to those along the line-of-sight. Given the axis ratio of the assumed circular disk, the galaxy's inclination is calculated to be 60° from face-on, reducing the line-of-sight rotation along the major axis by $\cos(60°)$. In addition, since the observations were taken 12° from the major and minor axes, this also needs

to be taken into account when comparing a model curve with the measured data.

Given the corrections described above, the following recipe is followed to model rotation velocity data before comparison with the observed data:

- construct a rectangular grid around the datapoint, $0.3''$ on either side along the slit and $0.625''$ either side across the slit;
- at each grid point, multiply the surface brightness at that position by the rotation velocity;
- resolve this weighted velocity into the component along the line-of-sight;
- sum contributions from each grid point over the resolution element and normalise by the total surface brightness in the grid;
- multiply result by $\cos(60°)$ for inclination correction.

Mathematically, the line-of-sight velocity at a point (x, y) on the plane of the sky is

$$v_{\rm ap}(x,y) = \frac{\cos(60°)}{\sum_{\Delta s}\Sigma(x,y)} \sum_{\Delta s} \Sigma(x,y) v_c(x,y) \frac{x}{\sqrt{x^2+y^2}}, \tag{4.25}$$

where Δs is each grid rectangle in the resolution element, $\Sigma(x, y)$ is the surface density (surface brightness $\times$ Υ) and the geometric factor resolves the vector along the line-of-sight. The construction for this calculation is shown in Figure 4.1, where the blue lines show the slit edges and the red squares denote the grid across one resolution element. The aperture velocity dispersion is calculated using a similar recipe, however the line-of-sight component is already calculated via Equation (4.12).

The anisotropy parameter, β_a, plays an important role in the rotation speed of the bulge component. Using Equation (4.13), the amount of rotation increases as β_a decreases, since this corresponds to more tangential and less radial motion. Thus, a mass distribution for the system may also constrain the degree of anisotropy in the bulge velocity distribution.

The measured velocity dispersion is not a function of the bulge density profile alone, but is increased by the presence of a large dark matter component in the inner regions. The disk component has its own small dispersion

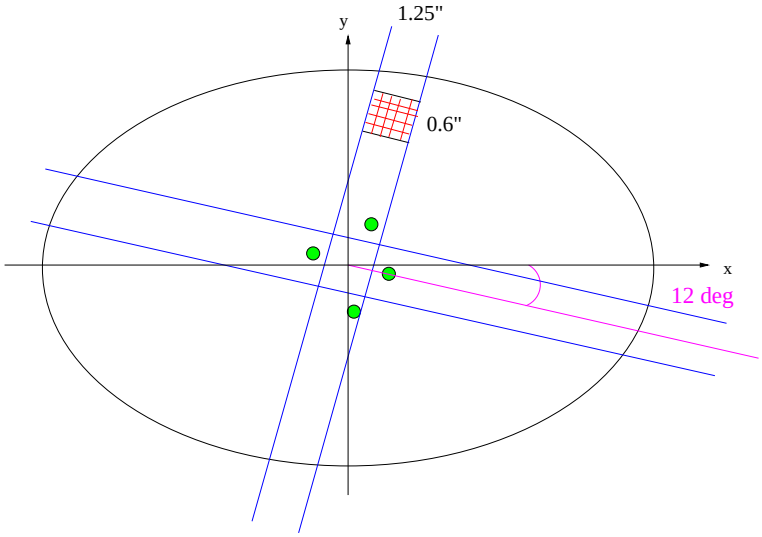

Figure 4.1: Schematic of the galaxy showing the spatial apertures (resolution elements) over which kinematic models must be integrated to compare with real data. The slit width during the observations was 1.25″ and the spatial resolution 0.6″. The blue lines show the position of the slit, 12° offset from the major and minor axes and the red grid shows how the kinematics are calculated. The green circles show the quasar image positions.

($\sim 20\mathrm{kms}^{-1}$) that can be ignored. Since the dark matter kinematics are not measured directly, the halo's influence will be observed through an increased dispersion in the bulge stars. This increase can be approximated by use of the hydrostatic equation to find the relationship between mass enclosed and dispersion in a spherically symmetric system. Note that Bottema (1993) and Kregel (2003) derive an estimate for the size of this effect for thin disks embedded in dark matter halos. Using Equation (4.6) and assuming a volume density profile, $\rho \sim r^{-\eta}$, and potential, $\Phi \sim M/r \sim r^{2-\eta}$, the radial dispersion, σ_r, is found to scale as,

$$\sigma_r^2(r) \sim r^{\eta} \sim \rho^{-1}, \qquad (0 < \eta < 1) \tag{4.26}$$

$$\sigma_r^2(r) \sim -r \ln r, \qquad (\eta = 1) \tag{4.27}$$

$$\sigma_r^2(r) \sim r^{2-\eta} \sim M(r)/r, \qquad (1 < \eta < 3) \tag{4.28}$$

where $M(r)$ is the mass enclosed at radius r (Bertin et al. 2002). Hence, the scaling depends on the density profile. In the case of the Sérsic profile used

here for the bulge, $\eta \sim 0.85$ in the central regions in which we are interested, and the first approximation is used. Hence, the dispersion calculated for the bulge component will be scaled by,

$$\sigma^2_{\rm meas} = \sigma^2_{\rm bulge} \times \frac{\rho_{\rm bulge}}{\rho_{\rm bulge} + \rho_{\rm halo}}, \tag{4.29}$$

to determine the overall stellar velocity dispersion, where $\sigma^2_{\rm meas}$ and $\sigma^2_{\rm bulge}$ denote the measured and bulge-alone velocity dispersions, respectively. Strictly, Equation 4.6 is for a self-gravitating system — bulge + halo. In this case the halo dispersion is unknown *a priori* and thus this approximation is used to factor the halo influence into the stellar dispersion.

4.4 Results

No models were able to fit all of the data to a statistically acceptable level. Given the simplicity of the models and the structure observable in the kinematic data, this is not surprising. The best-fitting solutions will therefore be taken and the goodness-of-fit studied while interesting parameters, such as the inner and outer slope of the dark matter halo and the bulge anisotropy parameter are varied.

4.4.1 Best fits

The model with the best-fitting solution has a massive dark matter halo with a softened isothermal density profile ($\gamma \sim 0$, $n \sim 2$) that dominates both the lensing convergence and rotational support of the galaxy at all radii across the optical disk. In this model, the bulge and bar have unphysically small mass-to-light ratios ($<0.03\Upsilon_\odot$, compared with $\sim$2–5$\Upsilon_\odot$ as discussed in Section 2.4.2) and the disk and external shear provide the shear for the image position fitting. The model also favours bulge orbits that are slightly tangential (β_a=0.05$\pm$0.05), although it is also consistent with isotropy. This solution is not acceptable, in a statistical sense with reduced $\chi^2 = 2.9$. Of the four components used for the χ^2 calculation, only the outer HI rotation points are fit acceptably. Table 4.2 shows the parameters for the best-fitting model and Figure 4.2 shows the rotation curve. The uncertainties are also shown for each parameter. They are defined as the deviation in the parameter value corresponding to an increase in the reduced χ^2 of one, while

Component	Parameter	Value
Bulge	M/L_I	$(0.03\pm0.09)\Upsilon_\odot$
	r_b	$3.9''$
	β_a	-0.05±0.05
Disk	M/L_I	$(2.5\pm1.7)\Upsilon_\odot$
	r_d	$11.3''$
DM Halo	κ_h	0.46±0.02
	r_h	$(1.85\pm0.25)''$
	γ	0.00±0.01
	n	2.53±0.05
Bar	M/L_I	$(0.03\pm0.09)\Upsilon_\odot$
Shear	$\gamma_{\rm ext}$	0.015±0.025
	θ_γ	$(18\pm100)^\circ$
Source	β_E	-0.021±0.020
	β_N	0.001±0.020
χ^2	Reduced χ^2	2.9

Table 4.2: Parameter values for the best-fitting solution with reduced $\chi^2 = 2.9$. The bulge and bar mass-to-light ratios are unphysically small in this solution suggesting the models require improvement. Here, β_E and β_N refer to the source position East and North of the galactic centre. The shear angle is measured counter-clockwise from the positive x-axis. Uncertainties are also shown corresponding to an increase of one in the reduced χ^2, keeping other parameter values constant.

keeping all other parameter values constant. Figure 4.3 shows the variation of reduced χ^2 with varying anisotropy parameter, β_a.

To reconcile this statistically unacceptable result, it is instructive to look at the model fit to the kinematics, keeping in mind that only the data to the left of the galactic centre is used to fit the rotation. Figure 4.4 shows the fits to the inner kinematics along the major and minor axis. The major axis rotation curve is well reproduced by the model, but the minor axis rotation is too high compared with the data. Similarly, the model dispersion profile has a flat profile overall, but deviates significantly from the data at most radii. The model is therefore not adequately reproducing the observed kinematics.

The constraints used to model the galaxy in Chapter 2 were primarily image positions with the two neutral hydrogen rotation points at large radius (and well away from the image positions). Given that no kinematic information was available in the central regions, the calculated rotation due to the four mass components was assumed to be circular motion based on balancing gravitational and centripetal acceleration. This means that an ac-

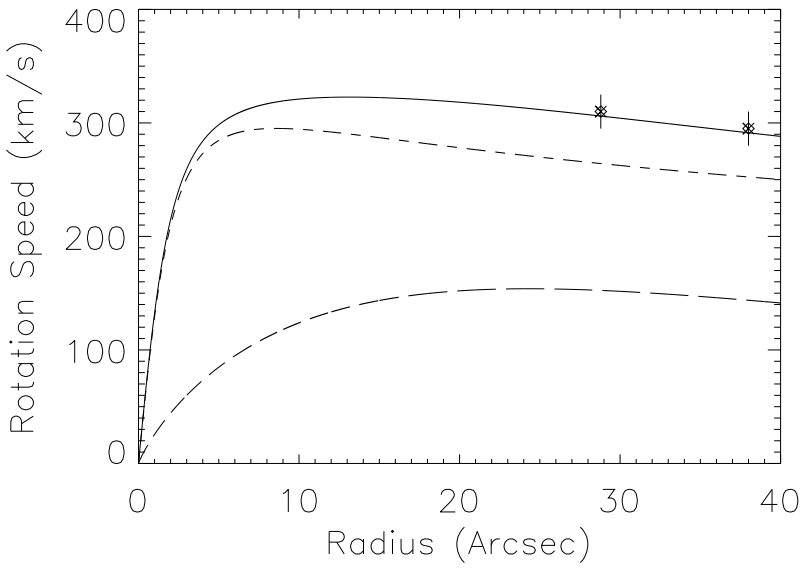

Figure 4.2: Rotation curve (edge-on) for the solution with the best χ^2. In this solution, the bulge and bar have unphysically small mass-to-light ratios and the lensing convergence and rotational support are dominated by the dark matter halo. The short-dashed line shows the halo rotation and the long-dashed shows the disk. Even here the disk is sub-maximal, providing $\sim$50 per cent of the rotational support, as found in earlier work.

ceptable fit to the data is attainable with the four smoothly modelled mass components because the constraints effectively lie at only two radii — $0.9''$ (images) and $\sim 30''$, and there is no kinematic information at the image radii. Therefore, there is room for deviations from reality at other radii where there are no constraints (see Figure 2.9 as an example). In comparison, the addition of the kinematic data effectively provides additional constraints from the galactic centre to $\sim 6''$. 2237+0305 has observable additional structure, not accounted for in the five component model, e.g., prominent spiral arms that are attached to the bar component. These may not be important for the lensing (their contribution may be accounted for by the external shear) but still produce anisotropy in the kinematics.

Kinematically, the bar is extremely difficult to model and a sophisticated attempt has not been made in this work. However, in the central few arcseconds its presence will have an effect on the streaming motions

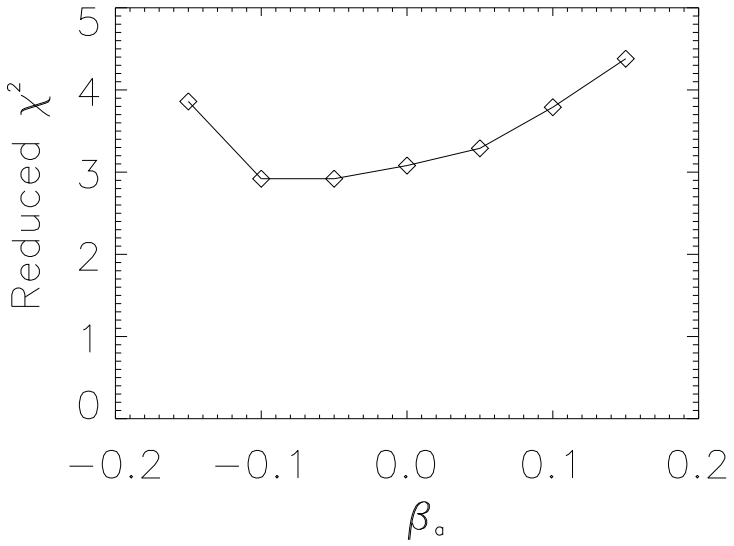

Figure 4.3: Best-fitting solution reduced χ^2 as a function of anisotropy parameter, β_a. The model favours a slightly tangentially anisotropic orbital structure for the bulge while being consistent with isotropy, however the variation in this β_a range is small.

of stars and therefore on the observed kinematics. In addition, the ad hoc method employed to include the dark matter contribution to the stellar velocity dispersion is an approximation, based upon hydrostatic equilibrium and therefore neglecting any ellipticity or anisotropy in the system. The true effect will be more complicated and depends on the clumpiness of the dark matter.

The inability of the minimisation routine to find an acceptable χ^2 reflects the inadequacy of the mass models to sufficiently reproduce the structure of the galaxy. The situation, however, is not as dire as it may appear. Solutions with bulge and bar mass-to-light ratios consistent with the previous results ($M/L_I \sim 2$) have reduced χ^2 statistics of ∼3.5–4. These are not the best solutions found but are not significantly worse.

An improved model is therefore required. The structural model is quite robust given that light profiles of the bulge, disk and bar have been observed, and that the bar itself has been modelled in detail by Schmidt (1996). The

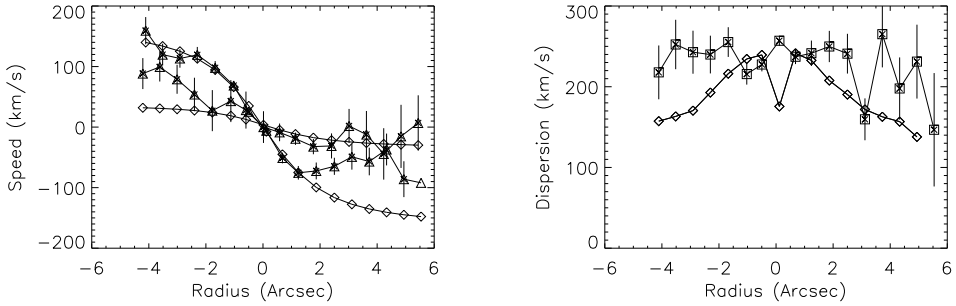

Figure 4.4: (Left) Major and minor axis data (triangles) and fits (diamonds) for the rotation curve (inclined and calculated over an aperture) for the best-fitting solution. The measurement uncertainties on the data are also shown as error bars. (Right) Major axis model (diamonds) and data (squares) line-of-sight velocity dispersion profiles for the best-fitting solution.

kinematic model, however, requires improvement.

Such modelling is beyond the scope of this work, however the analysis presented here can be used to investigate the density profile of the dark matter halo and whether it has a constant density core. The results from N-body simulations, which display a steeper inner slope for the density profile ($\gamma \sim 1$, although simulations do not converge to a universal value, Navarro et al. 2004), have been challenged by observational work that suggests the central regions of halos have constant density cores ($\gamma \sim 0$, $n \sim 2$, de Blok et al. 2001b). To probe the structure of the dark matter halo with the current modelling, the bulge mass-to-light ratio will be artificially constrained to be $M/L_I = 1.9$, which is the result found in Chapter 2, and the halo inner and outer logarithmic slopes varied to determine the goodness-of-fit of each model.

4.4.2 Dark matter halo structure

Firstly, the best-fitting solution for the fixed bulge and bar mass-to-light ratios will be established, before the halo parameters are also fixed.

Fixing mass-to-light ratios degrades the quality of the results compared with those presented above. Allowing the halo slopes to be free, the reduced χ^2 statistic for the best-fitting solution is 5.2 and the parameters for this model are shown in Table 4.3. The results are not significantly different to

Component	Parameter	Value
Bulge	M/L_I	$1.9\Upsilon_\odot$
	r_b	$3.9''$
	β_a	-0.05±0.05
Disk	M/L_I	$(2.5\pm1.1)\Upsilon_\odot$
	r_d	$11.3''$
DM Halo	κ_h	0.12±0.01
	r_h	$(1.22\pm0.03)''$
	γ	0.00±0.20
	n	2.24±0.15
Bar	M/L_I	$1.9\Upsilon_\odot$
Shear	$\gamma_{\rm ext}$	0.014±0.025
	θ_γ	$(198\pm110)^\circ$
Source	β_E	-0.034±0.020
	β_N	-0.010±0.020
χ^2	Reduced χ^2	5.2

Table 4.3: Parameter values for the best-fitting solution with the bulge mass-to-light ratio fixed. The reduced $\chi^2 = 5.2$. The bulge and bar mass-to-light ratios are unphysically small in this solution suggesting the models require improvement. Here, β_E and β_N refer to the source position East and North of the galactic centre. The shear angle is measured counter-clockwise from the positive x-axis. Uncertainties are also shown corresponding to an increase of one in the reduced χ^2, keeping other parameter values constant.

those found in the best solution. The shear angle has changed significantly, reflecting the need to adjust to the increased shear from the bulge and bar, and the source position has changed, but the disk mass-to-light ratio and the shear strength are relatively unaffected. Most interestingly, the halo is still best-fitted with a profile that has an almost constant density core and declines at large radius with logarithmic slope slightly steeper than isothermal.

The full edge-on rotation curve and the model fits to the kinematic data are shown in Figures 4.5 and 4.6. The dark matter halo, although it has a similar density profile to the solutions above, is much less massive, due to the significant contribution to the inner rotation by the bulge. The disk, again, is clearly sub-maximal (∼50 per cent). To the eye, the model fits the kinematic data as well as the model for the best solution. Indeed, the increased χ^2 is almost entirely accounted for by an increase in the deviation of the model from the observed image positions.

The inner and outer halo logarithmic slopes will now be fixed to phys-

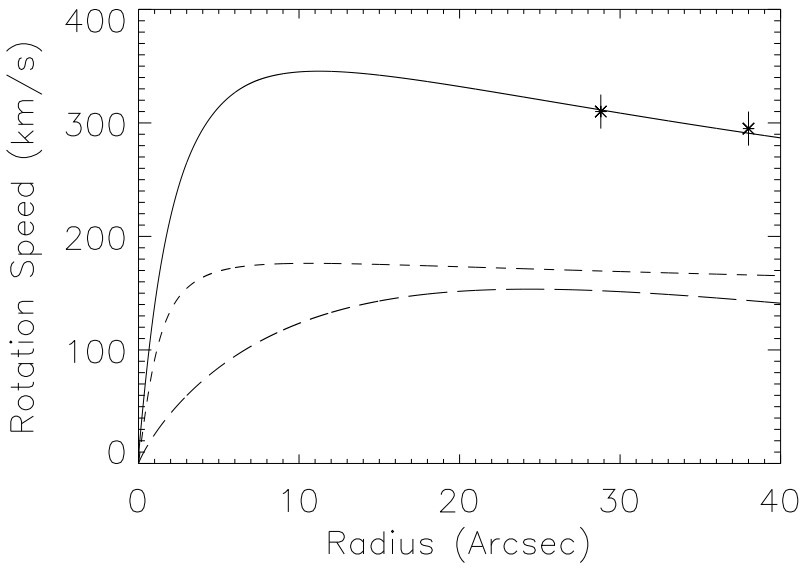

Figure 4.5: Rotation curve for the best-fitting solution with the bulge mass-to-light ratio fixed.

ically interesting values, keeping the bulge mass-to-light ratio also fixed at $M/L = 1.9\Upsilon_{\odot}$, and parameter space searched for the best-fitting solutions.

Figure 4.7 shows contours of the reduced χ^2 for models as a function of fixed halo slope parameters. Increasing the inner slope from zero (constant density core) worsens the fit significantly — the NFW result from N-body simulations ($\gamma = 1, n = 3$) has a reduced χ^2 of 7.1. This is primarily due to the worsening of the velocity dispersion fit and fitting the image positions. The NFW density profile cannot be ruled out by these results because the modelling cannot produce a statistically acceptable mass model, however the softened isothermal model is the preferred solution.

4.5 Discussion

Although the five component model used to construct the galaxy was not able to produce a statistically acceptable solution (reduced $\chi^2 = 1$), the best-fitting solution does reproduce the data to a level that suggests an acceptable model is attainable with future improvements. The most obvious

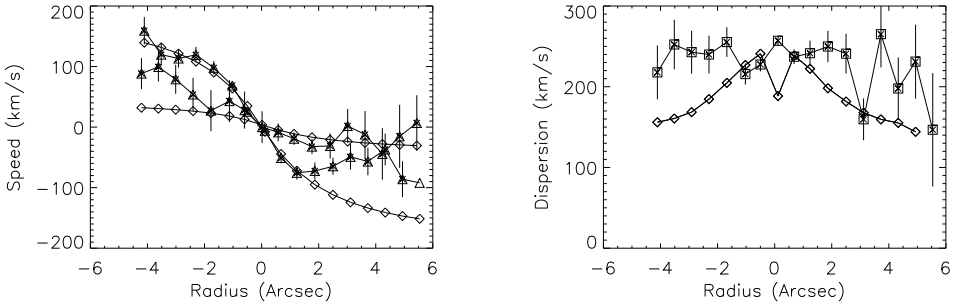

Figure 4.6: (Left) Major and minor axis data (triangles) and fits (diamonds) for the rotation curve (inclined and calculated over an aperture) for the best-fitting solution with the bulge mass-to-light ratio fixed. The measurement uncertainties on the data are also shown as error bars. (Right) Major axis model (diamonds) and data (squares) line-of-sight velocity dispersion profiles for the best-fitting solution.

way to improve the modelling is to include the bar orbits in the kinematic model. Since the bar lies at a different position angle to the other major components, it will have a complicated orbital structure that will have a non-trivial influence on the model kinematics. Recently, Shen and Sellwood (2004) modelled bar orbits to investigate the effect of mass concentrations on the stability and longevity of the bar. Binney and Tremaine (1987) also discuss bar kinematic models, including the idealised non-rotating system that features loop and box orbits of stars. Characteristics of such models could be applied to the bar in 2237+0305.

The contribution of the dark matter halo to the measured velocity dispersion needs to be carefully quantified. Given that one has no *a priori* kinematic and structural information about the dark matter component, general assumptions need to be made carefully. The poorer results for halos with central logarithmic slopes steeper than constant density are partly due to the steepening of the velocity dispersion profile for non-constant cores — a constant density core in the dark matter halo produces a flat velocity dispersion profile, in line with the observations. This is an important result for the profiles of dark matter halos and the predictions of N-body simulations, and therefore needs to be more rigorously investigated.

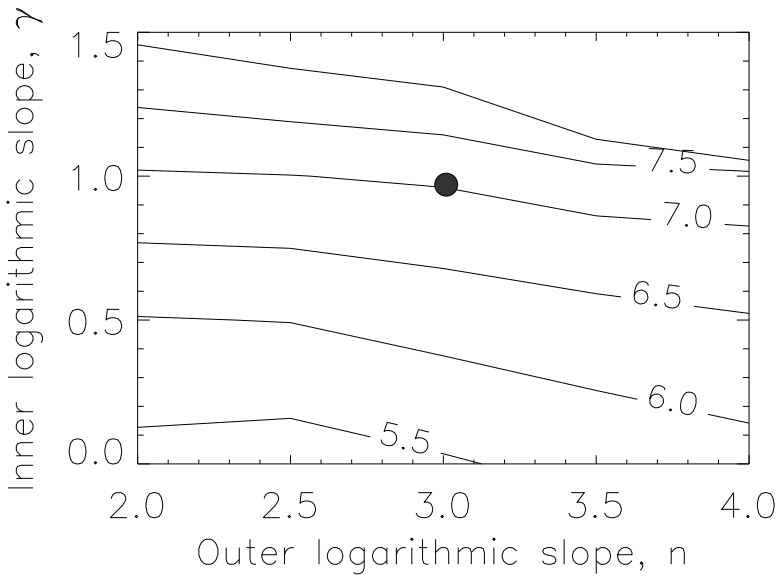

Figure 4.7: Contour plot of the reduced χ^2 statistic for the best-fitting model with inner and outer logarithmic slopes, γ and n. In these solutions, the bulge and bar mass-to-light ratios are also kept constant. The solution favours a halo with a constant density core and outer logarithmic slope between –2 and –2.5, but disagree with a solution consistent with the results from N-body simulations (γ=1, n=3, black circle).

4.6 Conclusions

The kinematic data providing the observed rotation and velocity dispersion profile in the central few arcseconds of 2237+0305 are combined with the knowledge of lensed image positions and the rotation beyond the optical disk (HI rotation points) to construct a structural and kinematic model of 2237+0305. Five components are used to constrain the mass distribution — a dark matter halo, modelled as spherically symmetric with a variable inner and outer logarithmic slope; a de Vaucouleurs bulge, modelled structurally with a flattening consistent with the light profile; an exponential disk, inclined at 60°; a Ferrers bar, at a position angle 39° from the disk major axis; and, an external shear, to account for the influence of perturbers along the line-of-sight. In addition, the bulge and bar mass-to-light ratios are constrained to be equal, since they combine in the galaxy to form one

continuous, but distorted, component, and share stellar orbits.

Kinematically, the bulge is modelled as a spherical Sérsic profile with a velocity anisotropy. This is found to be simpler than trying to calculate the kinematics for a flattened system. The model rotation curve and velocity dispersion profile are projected along the line-of-sight and then smeared over a spatial aperture corresponding to the resolution of the observations and the slit width, before comparison with the observed data.

The best-fitting solution is not a statistically acceptable fit. The reduced χ^2 for this solution is 2.9. This solution also has an unphysically low-mass bulge and bar, and a softened isothermal-like dark matter halo. The failure of the model to produce an acceptable solution reflects the inadequacy of the kinematic model to properly characterise the bulge and bar stellar kinematics, and the improvement required to the calculation of the halo contribution to the dispersion profile.

To investigate the goodness-of-fit for different halo models, the bulge and bar mass-to-light ratios are constrained to be $M/L_I = 1.9\Upsilon_\odot$, the best-fitting value found in the previous modelling presented in Chapter 2, and the reduced χ^2 calculated for the best-fitting model. A halo with constant density core and an outer logarithmic slope of $n \sim 2 - 2.5$, is found to be optimal. This solution had a reduced χ^2 of 5.2. The best-fitting solution for a model with a halo profile consistent with results from N-body simulations, $\gamma = 1$ and $n = 3$, had a reduced χ^2 of 7.1.

Future work will improve the kinematic model to include the effect of the bar on the streaming motion of stars, and investigate more rigorously how the density profile of the dark matter halo influences the observed kinematics.

CHAPTER 5

Detecting Dark Matter Substructure in the Galaxy

Cosmological models of structure formation in the universe predict the formation of dark matter halos as the first gravitationally bound objects. Small halos coalesce at the earliest times and grow to the massive halos we observe today via hierarchical growth. This scenario predicts that current dark matter halos are not smoothly distributed in space, but rather are lumpy due to the existence of smaller subhalos orbiting within them. Such dark matter subhalos should affect the stellar structure of massive galaxies due to their gravitational interaction as the subhalos transit the disk. The magnitude of this effect is calculated using simple scattering simulations and the signatures of stellar scattering discussed. The predictions are tested against observations from the next generation satellite, GAIA, which aims to measure the six-dimensional phase-space positions of a large number of stars in the Galaxy, to determine if the subhalos are detectable.

5.1 Introduction

The Cold Dark Matter theory of structure formation is very successful at describing many observations of the universe (Peebles 1982). Cold, collisionless, massive particles, which formed in the early universe, collapse gravitationally to form the seeds of today's galaxies. At later times, baryons fall into the dark matter potentials and sink to their centres via dissipative cooling, producing the luminous galaxies observed in the modern universe. These processes are understood in a general sense, but many of the details are, as yet, unknown (e.g. the formation of flattened stellar disks, and the distribution of dark matter in galaxies).

The mass function of dark matter halos in the universe is a function of time and the initial power spectrum of primordial density fluctuations. Measurements of the normalisation and power index of the spectrum are consistent with a bottom-up approach to structure formation: less massive halos form first and coalesce to form more massive halos at later times. As such, one expects smaller *subhalos* to coalesce with more massive halos. As the DM is collisionless, massive halos are spatially clumped — the subhalo structure is not destroyed immediately by collisional processes. Collisionless processes, such as phase mixing in a time-dependent potential, will eventually erase the subhalo memory, but this is a process with a long timescale (of order the relaxation time). Given the predictions of cold dark matter theory, one expects that dark matter subhalos reside in the Milky Way halo today, and therefore may be detectable via their gravitational effect on the stellar disk. It is the aim of this study to estimate the size of this effect and whether it is observable with the upcoming GAIA experiment.

The Galaxy's stellar disk is supported by rotation in the radial direction, and pressure in the vertical direction. Putting energy into the disk, via a transfer from a massive body, can increase the vertical velocity dispersion and increase the disk scale height ('heating'). Scattering of stars by a gravitational encounter with a massive object changes the local stellar velocity distribution function (DF) due to the transfer of energy from the more massive object to the stars. The change in the DF can be calculated by integrating over two-body interactions between the stars and the massive object.

Dynamical friction is an energy transfer process due to the gravitational

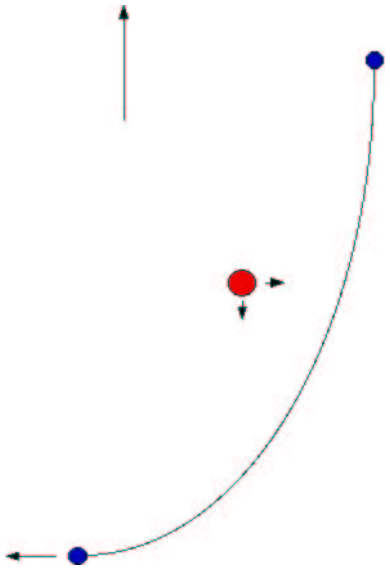

Figure 5.1: Example interaction between a star (blue) and massive object (red) showing the momentum changes (small arrows) for each particle after the interaction. The large arrow shows the direction of motion of the massive object. The massive object's forward motion is reduced.

interaction between bodies. When one massive body is moving through a sea of many less massive objects, it will, on average, transfer kinetic energy to the sea and thus have its own speed reduced. The sea increases its velocity dispersion due to the energy input. Dynamical friction is effectively the integrated effect of many two-body encounters between the massive and test objects. Each individual two-body interaction may transfer energy from the massive to the test particle, or vice versa, with a given probability, dependent on the exact geometry of interaction. The overall effect, however, is asymmetric parallel to the direction of motion of the massive object, and it loses forward momentum to the test particles. The momentum perpendicular to the direction of motion averages to zero since a uniform sea of test particles interact with it equally from both sides. Figure 5.1 shows an example interaction between the massive object (red) and the star (blue). The arrows denote the change in momentum for each particle.

Mulder (1983) constructed a distribution function for the response of the stellar medium to the passage of a massive object, using Jeans Theorem and the integrals of motion of the system. His analysis assumes a Maxwellian ve-

locity, and uniform spatial density, distribution function (DF) for the stars, and in a spherically symmetric potential. His solution treats the stars as test particles only, and does not include any subsequent stellar relaxation or diffusion. He investigates the overdensity of stars that accumulate in the massive object's wake, and the subsequent drag force exerted upon it. The shape and size of the overdensity is found to depend primarily upon the ratio of the object's speed to the stellar velocity dispersion (the 'Mach number').

In Section 5.2 and 5.3 the problem is introduced, and the collisionless Boltzmann equation, Jeans Theorem and Mulder's dynamical friction formalism are discussed. The satellite GAIA is then introduced, the uncertainties in its measurements are discussed, and possible sources of confusion in the Galaxy are reviewed in Section 5.5. Section 5.6 reviews the expected mass function for CDM halos from past work, and applies these expressions to a Milky Way-like galaxy mass. In Section 5.7, the semi-analytic results of Andrew Benson's simulations are used to obtain realistic subhalo properties. The simulations performed are then discussed in Section 5.9 and the relaxation of stars after subhalo transit is investigated in Section 5.9.1. Phase-space signatures of subhalos are then presented in Sections 5.10 and 5.11, and conclusions are drawn.

5.2 Boltzmann Equation & Jeans Theorem

The evolution of the phase-space distribution function (DF) of a system is governed by the collisionless Boltzmann equation:

$$\frac{df}{dt} = \frac{\partial f}{\partial t} + \vec{v} \cdot \nabla f - \nabla \Phi \cdot \frac{\partial f}{\partial \vec{v}} = 0, \tag{5.1}$$

where f is the mass per unit volume per unit velocity interval, and Φ is the mean-field gravitational potential of the system. In practice, this equation is difficult to solve and approximations are required. The integrals of motion of a system can be used to determine solutions in these cases. Jeans Theorem states that a DF that is only a function of the integrals of motion is necessarily also a solution of the Boltzmann equation (Binney and Tremaine 1987).

Mulder (1983) uses Jeans Theorem to look at the response of the DF of a system to the presence of a massive object. He chooses a DF that is only a function of the integrals of motion and that reduces to the unperturbed

solution at infinite distance from the object. In this way he finds a steady-state solution (which is not unique) to the DF in the massive object's frame without needing to consider the Fokker-Planck equation (which accounts for encounters between particles as non-zero diffusion terms on the RHS of Equation 5.1). The solution is simply the response of the medium and does not include the subsequent two-body relaxation of the stars after they have been scattered. He finds an overdensity of particles behind the massive object, which causes the dynamical friction.

The final DF can then be integrated over either spatial or velocity coordinates in order to find the density distributions. Both spatial density, $\rho(r)$, and velocity distribution, $f(\mathbf{v})$, are interesting for this problem — a signature of the massive object's presence could be found in either. GAIA has the ability to probe both domains.

5.3 Dynamical friction framework

Behind a massive object moving through a sea of test particles, an overdense wake is produced. This overdensity depends on the speed and mass of the massive object. For high Mach number (v/σ), the equidensity surfaces of the wake become highly collimated and this is a possible observable signature of the passage of the massive object. (Physically, in the massive object's frame, the test particles move towards the massive object with higher relative speed and some will therefore cross the object's path further behind it, stretching the region of overdensity behind the massive object.)

The mechanism of dynamical friction is analysed in Binney and Tremaine (1987). The most commonly used form of the equation for the deceleration of the massive object was first written down by Chandrasekhar (1943). This mean effect (averaged over many individual stellar orbits) requires that $v_M \gg v_{\text{test}}$ and $M \gg m$.

There are two intuitive ways to visualise the slowing of the massive object. Firstly, a single scattering event will change a test star's velocity by giving it a kick parallel to the direction of the massive object's motion. The massive object would simultaneously be kicked in the opposite direction; its forward speed decreases when integrated over many test stars. The perpendicular kicks average to zero.

The second way to visualise dynamical friction is by considering the

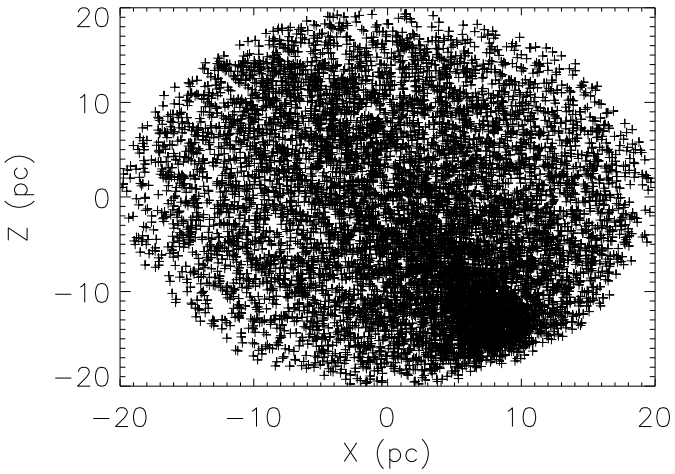

Figure 5.2: Overdensity of stars behind the subhalo (located at the origin), in the XY plane. The subhalo is moving in the $+Z$ direction (the overdensity is rotated as the stars have an initial velocity component in the X direction). Results taken from simulations described in Section 5.9.

paths of the test particles as they are scattered by the massive object. An initially uniform field of test particles will develop an overdensity behind the massive object as they are deflected around it since they are gravitationally attracted to it. This overdensity will exert a drag force on the massive object, slowing its motion. Figure 5.2 shows an example of a stellar field, and the overdense region behind the subhalo (located at the origin and moving in the $+Z$ direction), taken from simulations described in Section 5.9.

The commonly employed expression (Chandrasekhar 1943) for the slowing of an object of mass M, and speed $\mathbf{v}_M$, travelling through an infinite field of stars of mass m, with a Maxwellian velocity distribution, is given by,

$$\frac{d\mathbf{v}_M}{dt} = -\frac{4\pi \ln\Lambda G^2 \rho_0 M}{v_M^3}\left[\mathrm{erf}(X) - \frac{2X}{\sqrt{\pi}}\exp(-X^2)\right]\mathbf{v}_M, \qquad (5.2)$$

where Λ is the Coulomb logarithm and is given by $\Lambda = b_{\max}V_0^2/G(M+m)$, $b_{\max}$ is the maximum scattering impact parameter, V_0 is the initial relative velocity, $X = v_M/\sqrt{\sigma}$, σ is the stellar velocity dispersion and ρ_0 is the background stellar density. Most importantly, the deceleration is proportional to the mass M. This equation can be used to estimate the

heating of a test particle (see Section 5.8).

The overdensity will be calculated in a region as,

$$\delta = \frac{\rho}{\rho_0} - 1, \tag{5.3}$$

where ρ_0 is the background density seen in Equation (5.2). What is the threshold overdensity required for the stars to be observable over the background? This question has different answers depending on whether a uniform stellar distribution is assumed, or a real, clumpy disk distribution. Similarly, the projection of an overdensity onto the sky will dilute any observable effect. The addition of three dimensions of spatial information can help in this regard, isolating a streamer of stars. Here, the uncertainties of the GAIA results are critical, and these are discussed next.

A discussion of confusing sources of phase-space signatures is then presented, followed by an investigation of the spatial and velocity domain signatures for point-mass and extended subhalos. The results are then compared with the expected number and distribution of subhalos from N-body simulations.

5.4 GAIA as the instrument of choice

GAIA (Global Astrometric Interferometer for Astrophysics) is a European Space Agency satellite to be launched in 2010–2012 to the second Lagrange point (Lindegren and Perryman 1996). Its primary science goal is to measure the six dimensional phase-space co-ordinates of 1 billion Galactic stars to unprecedented accuracy, easily surpassing the previous census performed by the Hipparcos satellite. With expected microarcsecond astrometry it will measure radial velocities, distances (via parallaxes) and proper motions to high precision. The final catalogue will provide a high precision view of the spatial and kinematic structure of the Galaxy.

Initial estimates of measurement uncertainties for GAIA are calculated using basic mission data such as primary mirror size and CCD efficiency. An Astrometric Accuracy Tool has also been developed to simulate data with more secondary effects such as star colour, effect of choice of mirror coating, and differences in the spatial scanning method with position on the sky. The predictions used in this work are derived from preliminary estimates;

advanced results are not yet available.

The predictions for the accuracy of parallaxes measured with GAIA can provide estimates of distances to bright stars and those within a few kiloparsecs (parallax measurements are used for distance determinations). Table 5.1 shows the distance error of stars with a given V-band apparent magnitude as calculated from the quoted GAIA uncertainties (Lindegren and Perryman 1996). Also included is the V-band absolute magnitude of such stars at the given distance. Clearly, faint stars will not be visible at large distance. Bright stars are accurate to distances of ∼10 kpc. Fainter stars

V	Error	Distance	M_V	Δd	Δv
	μas	kpc		%	kms^{-1}
20	160	1	10	16	1.5
20	160	5	6.5	80	8
20	160	10	4.8	>100	15
20	160	20	3.5	>100	30
15	11	1	5	1	0.1
15	11	5	1.5	5	0.5
15	11	10	0	10	1
10	4	1	0	0.4	0.04
10	4	5	-3.5	2	0.2

Table 5.1: Parallax errors of stars with given V-band apparent magnitudes and distances from the observer as a percentage of actual distance. The absolute magnitude is also shown to demonstrate the use of bright stars at large distances. The final column gives the proper motion uncertainty given the parallax errors.

are only accurately measured within ∼1 kpc. This implies that unwanted faint stars may be incorrectly located in space and therefore measured to lie in a region of interest where they do not actually reside — one cannot say where they are located with certainty. This is reason to attempt this analysis with only brighter stars. Similarly, Table 5.1 shows the proper motion uncertainty expected given the parallax errors. The velocity distributions of stars at a distance of 10 kpc from the Sun should be accurate to better than 15 kms^{-1}. In addition, GAIA will be able to measure radial velocities to 1–10 kms^{-1} out to V=16–17 (the range accounts for the distance uncertainty to the star). This accuracy is comparable to that in the plane of the sky.

Accuracy in distance and proper motion measurements is critical for

the isolation of subhalos in phase space. The use of brighter stars for this analysis is clearly better than fainter stars, however the small number of bright stars could ruin any potential signal. Holmberg and Flynn (2000) quote the number density of local stars within absolute magnitude bins from Hipparcos and HST measurements. Table 5.2 reproduces these values from Table 1 of Holmberg and Flynn. The faintest bin therefore accounts

Magnitude Bin	$\rho(0)$ $M_\odot \mathrm{pc}^{-3}$
M_V <2.5	0.0031
2.5< M_V <3.0	0.0015
3.0< M_V <4.0	0.0020
4.0< M_V <5.0	0.0024
5.0< M_V <8.0	0.0074
8.0< M_V	0.014

Table 5.2: Local stellar densities in the Galaxy within different absolute V-band magnitudes reproduced from Table 1 of Holmberg and Flynn (2000). All results are from the Hipparcos catalogue, except for the $M_V > 8.0$ bin which uses HST number counts.

for $\sim$ 46 per cent of the total local stellar census (excluding brown and white dwarfs). These stars reach V=20 at d=2.5 kpc where their distance uncertainty is $\Delta d/d \sim 0.4$. Assuming only V=15 stars are to be used within 2.5 kpc (due to their reasonable distance uncertainties), only 15 per cent of the stars ($M_V < 3.0$) are available. Figure 5.3 shows the percentage of stars available for use as a function of distance from the Sun. Clearly, an apparent magnitude cut at V=15 would only be useful for subhalos passing within 2–3 kpc of the Sun, since so few are available beyond $\sim$3 kpc. These issues will certainly reduce the probability of a subhalo being detected.

The GAIA uncertainties quoted in Table 5.1 and the stellar densities published in Holmberg and Flynn (2000) will be used as the threshold values in all subsequent analysis.

5.5 Confusion

The Galaxy is not composed of a uniform distribution of stars with a well characterised velocity or spatial distribution function. The issue of confusion in both domains is a critical factor for detecting dark matter subhalos. Collections of stars such as star formation regions and spiral arms have higher

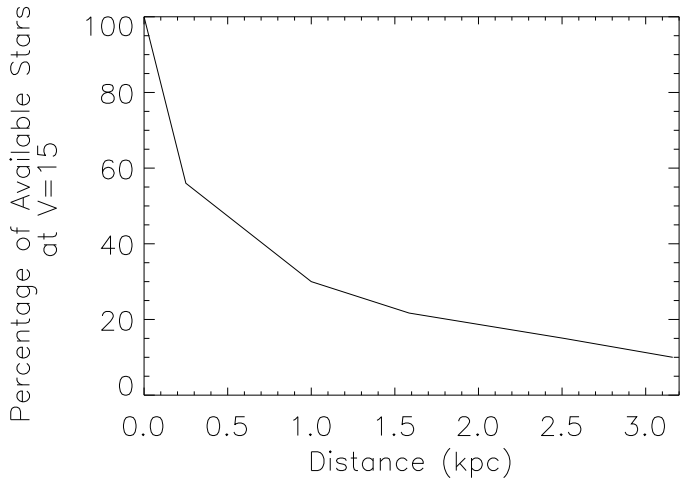

Figure 5.3: Percentage of available stars for analysis as a function of heliocentric radius for a V=15 cutoff. Even the brightest stars are only available within 3 kpc of the Sun.

density than surrounding regions, possibly mimicking the dynamical friction signatures of a transiting object.

To determine the level of inhomogeneity in the disk itself, we look at results from the most recent comprehensive study of the phase-space distribution of stars in the disk, performed by the Hipparcos satellite (Esa 1997). In most studies, the disk density distribution is determined using kinematic information, since distances are poorly determined. Chereul et al. (1999) investigated inhomogeneities in the Hipparcos sample for A-F type dwarf stars within 125 pc of the Sun. They identified 11 spatial structures based upon a wavelet analysis, which provides overdensities on a given spatial scale (a cut on velocity was also performed to find coherent stellar structures). The structures are mostly known star clusters with 2–40 stars, occupying regions of volume $5\mathrm{pc}^3$–$2\times10^5\mathrm{pc}^3$. For structures with less than ~ 5 stars, the Poisson noise is greater than the overdensity signal, and the result is uncertain (Poisson statistics are used to quantify the variance of stellar densities with location in space). Removal of these systems leaves 6 structures with overdensities in the range δ=0.06–13 (in this case 6 stars were found in a volume where 0.43 A-F dwarfs are expected to reside; a sphere of radius

$\sim$6 pc). Of these, five are on scales interesting to this work ($\sim 10^4$ pc^3), and their overdensities are in the range $0.06 < \delta < 3$.

Holmberg and Flynn (2000) also used a sample of A-F stars within 200 pc of the Sun to determine the vertical mass density of the disk in a given region of sky, using a technique dependent upon vertical velocity components. Inhomogeneities are produced by large-scale structures such as spiral arms, as well as local structures such as star formation regions. Within this region, they find a total mean mass density of 0.102 ± 0.010 M$_\odot$pc^{-3} within 200 pc of the Sun, and a total *stellar* mass density of $\sim$0.044 M$_\odot$pc^{-3}, based upon Hipparcos, HST and local density counts. The stellar number density is found to be $\sim$0.023 pc^{-3}. As well as the $\sim$10 per cent uncertainty in the total mass density, obtained from uncertainties in measured parameters, Figures 6 and 7 from Holmberg and Flynn (2000), which display the vertical distribution of A and F stars and their best-fits, can be used to determine the magnitude of individual inhomogeneities. As above, they are typically of size $\delta = 0.1$–0.3. These values will be taken as representative of the magnitude of density variations throughout the stellar disk.

Heating of the Galactic disk is caused by many effects, including the deposition of energy by transiting subhalos. Benson et al. (2004) uses N-body simulations and semi-analytic calculations to reproduce the observed distribution of disk scaleheights using subhalo heating and scattering of stars via molecular clouds. A Milky Way-like disk is predicted to be heated from a thin disk to one with $h = R_d/R_v \sim 0.2$ (where R_d and R_v are the radial and vertical disk scale lengths, respectively), consistent with the calculations of Mendez and Guzman (1998) and the models of Dehnen and Binney (1998) that obtain h=0.18$\pm$0.05. Local heating leads to a global increase in disk scaleheight via mixing of individual heated stars with external, unheated stars (galaxies are observed to have uniform disk scaleheights with radius, de Grijs and Peletier 1997).

Locally, other heating effects, such as scattering by molecular clouds, must be quantified and characterised to avoid confusion with real subhalos. Lacey (1984) calculates the disk heating due to scattering of stars by a cloud of mass, M_c. Assuming the cloud scaleheight is less than the disk, the evolution of the stellar velocity dispersion with time can be described by (from Eqns (55)–(56), Lacey 1984),

$$\sigma(t) = \left(2t\alpha + \sigma_0^4\right)^{1/4}, \tag{5.4}$$

where σ_0 is the unperturbed dispersion, and $\alpha \propto M_c \Sigma_c$, is a collection of constants including the cloud mass, surface density of clouds and the vertical epicycle frequency, with the approximate value, $\alpha \approx 10^{17} m^4 s^{-5}$ in our Galaxy. Given this expression, one typically massive molecular cloud (M_c=6×10^{5}M$_\odot$) in a region of 100 pc^2 will increase the velocity dispersion by 50 per cent over 10^8 years. (Note that this calculation is based upon the dynamical friction mechanism where there is a preferred direction and $\langle v \rangle \neq 0$, unlike the diffusion calculation of Wielen (1977) which assumes isotropic diffusion in velocity space, $\langle v \rangle = 0$).

The assumption of a Gaussian velocity dispersion in the vertical direction is also a simplification. The sample of Holmberg and Flynn (2000) shows an excess of stars with lower velocities than expected from a normal distribution, and hence a deficit at higher speeds. This discrepancy is typically at the 10–20 per cent level.

As well as a study of the distribution of stars in stellar associations, there are other factors affecting these results. Firstly, A-F dwarfs are typically an older stellar population and therefore have had sufficient time to diffuse from their original birth clusters. One would expect younger O and B type stars to have different clustering properties as they have not had sufficient time to mix out. There is also the issue of the overall density distribution of the disk, which can vary by a factor of ∼30 radially, from the centre to the outer disk edge. In addition, the disk density profile is not a pure exponential. López-Corredoira et al. (2004) use 2MASS, MSX and ATCA/VLA data to investigate the large-scale (several kiloparsecs) deficit of old and young stars with respect to a pure exponential disk model, 2–4 kpc from the Galactic centre, on the mid-plane. Such a deficit will not cause confusion with the signatures of a subhalo transit because it occurs over a large region and is axisymmetric, suggesting it is caused by an intrinsic effect. More critical is the smaller scale (∼100s pc), localised clumpiness discussed above.

Given these results, a threshold overdensity of at least δ=0.4, to exceed the background clumpiness of the stars, and departures from Gaussian velocity dispersions of at least 50 per cent, to exceed the dispersion due to molecular clouds, are required to separate the signatures of a real subhalo

transit from natural disk inhomogeneities.

5.6 Probability of subhalo transit

5.6.1 Analytic considerations

There will be a given mass of subhalo above which the disruption to the stellar orbits will be detectable. The likelihood of objects above the minimum mass passing through the disk at any one time need to be calculated. Assuming the mass function of subhalos is a power law (this is discussed below), the number density can be represented by,

$$dN = \alpha M^{-\beta} dM \tag{5.5}$$

where α and β are constants found from numerical simulation.

One can ask what the probability is that, at any given time, a subhalo of mass $M > M_{\rm min}$ is lying within the disk. To simplify matters, let all subhalos move at the same speed at all times (simple harmonic motion could be used for a better estimate, but semi-analytic modelling discussed in Section 5.7 shows this assumption to be adequate, as most subhalos transit the disk with similar speed). Then, the probability that one particular subhalo is within the disk is simply the ratio of disk volume to the volume of the sphere containing the subhalo orbits. The probability for all subhalos combined is then this ratio multiplied by the number of subhalos with mass greater than the minimum,

$$\begin{aligned} P(M > M_{\rm min,indisk}) &= \frac{V_d}{V_T} \times n(> M_{\rm min}) && (5.6)\\ &= \frac{V_d}{V_T} \times \int_{M_{\rm min}}^{\infty} \alpha M^{-\beta}\, dM && (5.7)\\ &= \frac{V_d}{V_T} (\frac{\alpha}{\beta - 1} M_{\rm min}^{1-\beta}). && (5.8) \end{aligned}$$

In reality, the disk passage will occur at the maximum in the subhalo's speed and so the actual probability will be less than this simple ratio.

5.6.2 Numerical results

Springel et al. (2001) simulated a cluster of galaxies and produced a mass

function for subhalos within the primary potential. Although their results are presented graphically, we extract the values for α and β,

$$\alpha \sim 10^{11} M_{\odot}, \beta \sim 1.9, M_{\rm cluster} = 10^{15} M_{\odot}. \tag{5.9}$$

Scaling $M_{\rm cluster}$ down to a Galactic mass of $\sim 10^{12} M_{\odot}$ changes α to $\sim 10^{8} M_{\odot}$, giving

$$P(M > M_{\rm min}) = \frac{V_d}{V_T}(10^8 M_{\rm min}^{-0.9}). \tag{5.10}$$

For a typical galaxy with a disk of radius 20 kpc and thickness 500 pc, the volume ratio is ~ 0.02. Hence, there need to be $\sim$50 subhalos with mass in excess of the minimum for a good chance of detection.

Zentner and Bullock (2003) undertook simulations to investigate the merger rates, destruction probabilities and substructure properties of galaxy-mass halos with different input power spectra. They find a mass function with the form,

$$\frac{df}{dx} = \left(\frac{x}{x_0}\right)^{-\alpha} \exp\left(-\frac{x}{x_0}\right) \tag{5.11}$$

where f is the number of subhalos with normalised mass, $x \equiv M/M_{\rm host}$, $\alpha = 0.6$ and $x_0 = 0.07 \pm 0.05$, and the host mass varies between 10^{11} and $10^{13} M_{\odot}$. The integral of this function gives the mass in subhalos greater than the minimum mass. This expression gives $\sim$80 subhalos with greater mass than $10^8 M_{\odot}$ in a $10^{12} M_{\odot}$ host halo. If the minimum is $10^7 M_{\odot}$, this becomes $\sim$330 subhalos. Figure 5.4 displays this graphically for the results of Springel et al. (2001) for $\beta = 1.8$, 1.9. There are few subhalos with $M > 10^9 M_{\odot}$. Hence, if the minimum subhalo mass that is detectable is large, there will be few available for detection, and fewer in the disk itself, at any one time. If 50 subhalos are required to have mass in excess of the minimum, these results suggest that $M_{\rm min} \lesssim 2 \times 10^8 M_{\odot}$ must hold for detection.

The estimate of the subhalo's speed and fractional time within the disk is investigated in more detail in the next section, with semi-analytic results for the evolution of subhalos.

5.7 Semi-analytic results for Milky Way-like halos

Semi-analytic methods are useful for investigating the statistical properties of halo mergers and tidal stripping since they do not require the compu-

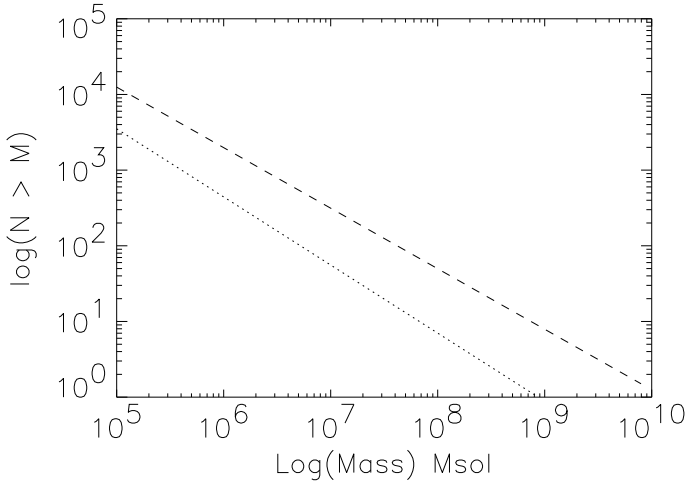

Figure 5.4: The number of subhalos with mass greater than M, as a function of mass, for two values of the power law exponent, $\beta = 1.8$ (dashed) and 1.9 (dotted), in a 10^{12} $M_{\odot}$ halo.

tational power of full N-body simulations. They take the Press–Schechter formalism for the distribution and masses of dark matter halos and randomly generate halos merging and interacting with other halos and subhalos. Each halo is assigned a disk and bulge component and their orbits are integrated forward in time under the influence of the mean gravitational force, as well as dynamical friction due to the different components. Mass loss and tidal heating are investigated by calculating the halo's tidal radius at each timestep and removing material beyond this radius.

Benson et al. (2002) details semi-analytic models used to study the effects of a photoionising background on galaxy formation. These models are based upon the earlier work of Cole et al. (2000) and include an improvement developed by Taylor and Babul (2001) of tidal stripping of satellites. The dark matter results for semi-analytic subhalos, kindly provided by Andrew Benson, will be used to determine the expected mass and spatial distribution of subhalos in a Milky Way-like halo.

Benson's code assigns a mass, energy, angular momentum and orbit to a satellite and integrates forward from its apocentric distance (where the tidal effects of the main halo are smallest). The initial energy and angular

momentum are chosen using global parameters of the host halo (e.g. its virial radius) which are consistent with those observed in N-body simulations. The dark matter halos are modelled as NFW halos (Navarro et al. 1996), suitably altered by adiabatic contraction due to the baryonic component, and the disk and bulge by exponential and de Vaucouleurs profiles. At each point in the orbit, the radius at which the tidal forces from the main satellite equal the self-gravitating force within the subhalo, is calculated, along with the effect of dynamical friction on the different components (Benson employs the Chandrasekhar formula here) and any heating due to shocks as components cross. The mass loss at each step is therefore calculated and mass is removed in spherical shells.

The output of the code provides the mass, density profile, time, location and speed of the subhalo at each disk crossing. Only the results for Milky Way-like halos will be considered (bulge to bulge+disk mass ratio is 5–20% and $v_{\rm disk} = 210 - 230 {\rm kms}^{-1}$). Given the N-body results for the mass function of dark matter subhalos described in Section 5.6, Benson's results can provide insight into the frequency of disk transits, and the subhalo's speed and mass loss. These are critical for ascertaining the abundance of detectable subhalos in the Galactic disk today.

Benson has produced tables of some of the host halo - subhalo interactions in his simulations. He has chosen a few interesting examples where the mass, speed and position of the subhalo is traced over several disk crossings. Interestingly, these subhalos can pass within a few kiloparsecs of the Galactic centre and with high frequency (crossing times $\sim$100 Myr), making them easier to detect; they are in a high stellar density region more often. Some will of course have much longer periods and larger impact parameters, but these initial results are encouraging. The major drawback evident from these results is the rapid loss of mass from the subhalo, since the magnitude of the dynamical friction heating scales with mass. The first few disk crossings can strip >99 per cent of the mass.

In order to properly characterise the subhalos, many of these output files are required to build-up a statistical view of the masses, crossing times, speeds and impact parameters. In the first instance, a few examples will be used to determine the viability of detecting a subhalo. A positive result would then warrant a deeper investigation.

Below are presented results for one subhalo followed in the simulation

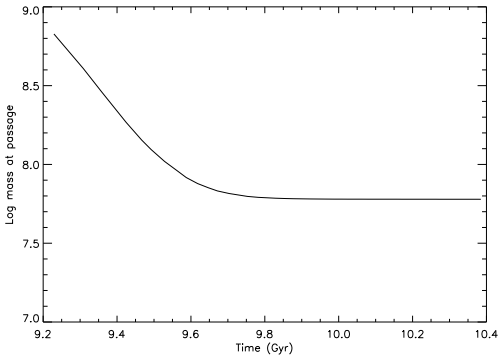

Figure 5.5: Mass of subhalo vs time. The subhalo rapidly loses mass and then stabilises.

for about 1 Gyr. The subhalo's mass, speed and impact parameter from the Galactic centre for each passage through the disk are plotted. This subhalo began with $1.4{\times}10^{10} M_{\odot}$ in the simulation and crosses the disk once every $\sim$20 Myr in the period of time shown.

The points in the figures each represent a passage of the subhalo through the disk. They are:

- Figure 5.5: Mass of subhalo vs time. The subhalo rapidly loses mass and then stabilises.
- Figure 5.6: Position of subhalo vs time. This is the distance to the Galactic centre from the subhalo's passage point in the disk.
- Figure 5.7: Speed of subhalo as it passes through the disk mid-plane as a function of time. Each point represents one disk passage.
- Figure 5.8: Time between impacts (Myr) vs time. As the subhalo slows, its crossing time reduces.

The critical information to be taken from these results are:

- the rapid mass-loss the subhalos undergo as they transit the disk. Figure 5.5 shows that a 10^9 $M_{\odot}$ subhalo will lose $\sim$90 per cent of its mass within 1 Gyr. This would reduce the subhalo to have mass $\sim$ $10^8 M_{\odot}$, and move from a potentially detectable signal to being undetectable with GAIA (see results for these masses later in Section 5.9);

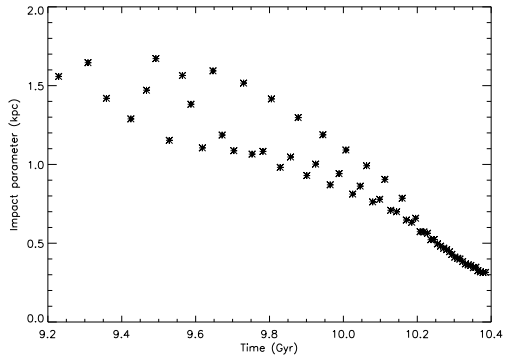

Figure 5.6: Position of subhalo vs time. This is the distance to the Galactic centre from the subhalo's passage point in the disk.

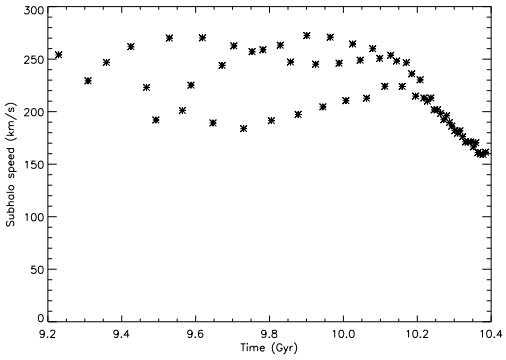

Figure 5.7: Speed of subhalo as it passes through the disk as a function of time.

- the speed of the subhalo at disk transit — all results point to a value of $v \sim 200\text{kms}^{-1}$ being representative of the simulation results (100–300kms^{-1} observed from Benson's simulations);
- fractional time spent within disk — the simplified estimation of 0.02 presented above is reasonable.

Given these values, the original estimation of the required number of subhalos in the potential is reasonable. In order to have at least one sufficiently massive subhalo in the disk at any given time, the minimum mass must be less than $\sim 2\times10^8 M_\odot$, as discussed in Section 5.6.2.

The phase-space signatures due to point-mass and extended subhalos of

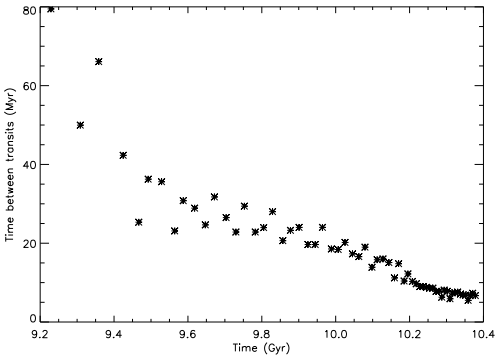

Figure 5.8: Time between subhalo transits of the disk (Myr) vs time. As the subhalo slows via friction and its apogalacticon decreases, its crossing time reduces.

different mass will now be investigated.

5.8 Point mass subhalos

The overdensity produced by a point-like object can be calculated. In his Appendix IV, Mulder (1983) derives an approximate functional form for the overdensity compared with the background. This approximation is sufficient for our purposes and is simple to compute. It is:

$$\delta = \frac{\rho - \rho_0}{\rho_0} = \frac{GM}{r\sigma_0^2} \exp\left[-\frac{p^2}{2}(1-\mu^2)\right]\left[1 - \mathrm{erf}\left(\frac{p\mu}{\sqrt{2}}\right)\right] \qquad (5.12)$$

where M is the mass of the compact object, $p \equiv v_0/\sigma_0$ is the Mach number, $\mu \equiv cos(\theta)$ and 'erf' is the standard error function. The density distribution is obviously axisymmetric about the axis of the object's motion and so δ is best written in cylindrical co-ordinates where the z-axis is defined to be the direction of motion of the compact object.

A threshold overdensity is required according to the quality of observational data in the spatial domain. A subhalo speed of v_0=200 kms^{-1} is assumed following the results from semi-analytic models (Section 5.7). This gives a Mach number of p=10 for a velocity dispersion of σ_0=20 kms^{-1}. In this high speed, high mass-ratio regime, the overdensity is highly colli-

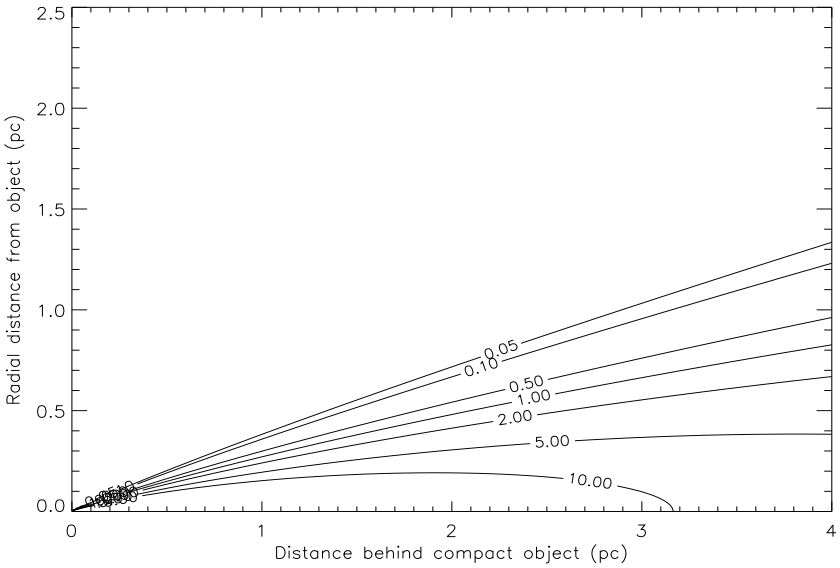

Figure 5.9: Spatial overdensity contours for stars behind a compact object of mass $10^7 M_\odot$ with $p \equiv v_0/\sigma_0 = 10$. The equidensity contours are collimated due to the speed difference between the point mass and the test particles, and the few parsecs behind the point mass have significant overdensities, $\delta \sim 10$.

mated behind the object. Above is plotted the overdensity contour map for a subhalo mass of M=$10^7 M_\odot$ in Figure 5.9. The inner few parsecs have overdensities $\delta \sim 10$. The ratio of radial to axial distance of the equidensity contours is independent of mass (dependent upon p) and has a value of 0.06 at their respective maximum values. The overdense region is therefore highly collimated.

In the velocity domain, a star passing reasonably close to a $10^8 M_\odot$ compact object [$b_{\max} \sim 1\mathrm{pc}(M/10^8 M_\odot)^2 (V_0/200\mathrm{kms}^{-1})^{-4}$] approaching at 200 km/s, will gain $\sim$200 kms^{-1} in speed ($\Delta v_m \sim V_0$). So, for very massive objects one would expect to see a shift of the velocity centroid of the stellar DF to that of the object's, in the rest frame of the galaxy, easily exceeding the GAIA uncertainties.

5.9 Real subhalos — extended mass distributions

Real subhalos are not compact objects, according to the results of N-body simulations. Their distributed nature will reduce their ability to disperse and accelerate stars. N-body simulations of the collapse and virialisation of dark matter halos (e.g. Navarro et al. 1996) find a nearly universal spherically averaged density profile. This profile is universal in the sense that only the scale length changes according to collapse redshift, but the overall shape remains the same — density as a function of radius follows r^{-1} in the inner regions, and r^{-3} in the outer.

In order for the acceleration due to the potential to be derived analytically, a slightly altered profile will be used in the simulations. This profile,

$$\rho(r) \propto \frac{1}{\frac{r}{r_s}\left[1+\left(\frac{r}{r_s}\right)^2\right]}, \tag{5.13}$$

has the same asymptotic features as the NFW, and the same scale radius, r_s. This scale length is chosen such as to match semi-analytic models of subhalos in a Galactic potential (see Section 5.7). Given that the cooling of baryons to form a disk in such an object should produce adiabatic contraction of the halo (Blumenthal et al. 1986) and thus alter this profile, the small difference between Equation (5.13) and the NFW result is negligible.

The effect of this subhalo on disk stars is modelled in a simple simulation that tracks the orbits of test particles (stars) moving in the combined potential of a disk plus subhalo. A 3D distribution of stars is constructed by randomly placing particles in a planar disk with a thickness of 500 pc. The initial velocities of the stars are all chosen to have Maxwellian velocity dispersion in all three velocity components, as well as a circular rotation determined by their position in an exponential disk.

The Cartesian co-ordinates of the disk, x and y, lie in the disk plane, and z is normal to the plane. The simulation is performed in the subhalo's rest frame (co-ordinates X, Y and Z), whereby the stars all begin with $\overline{v_Z} = -v_{\rm sub}$, $\overline{v_X} = v_{\rm circ}/\sqrt{2}$, $\overline{v_Y} = v_{\rm circ}/\sqrt{2}$ with $v_{\rm sub}$ the subhalo's speed and $v_{\rm circ}$ the circular rotation speed (see Figure 5.10 for an explanation of the co-ordinate system). The subhalo begins at the disk edge and moves normal to the plane of the disk. This is an idealised trajectory for the subhalo, and is employed for computational simplicity. Until the size of a potential signal

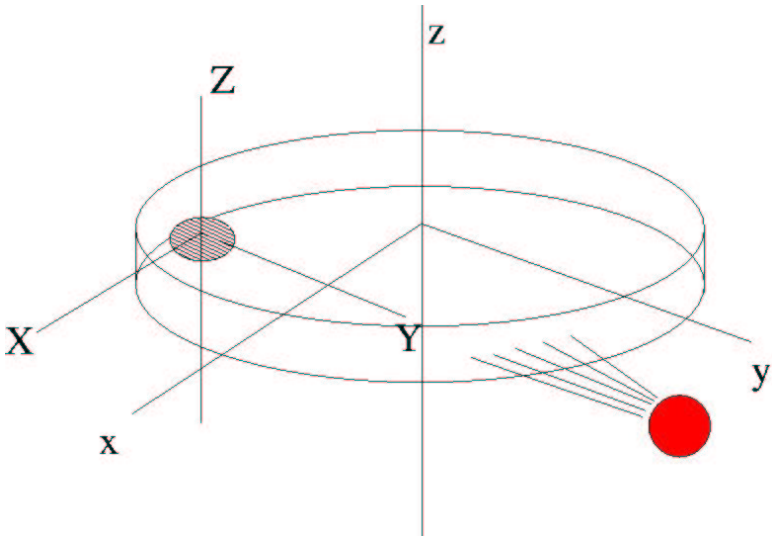

Figure 5.10: Co-ordinate system for the simulations (observer, red, looking through the disk; subhalo, hashed). Lower case letters refer to the stationary observer's frame viewing the rotating galaxy from the outside. The upper case letters refer to the subhalo's frame, in which the simulations are performed.

is obtained with this simple simulation design, it is not worthwhile pursuing more complicated models. The subhalo remains a static potential that does not respond to interactions with the stars.

The combined potential of disk and subhalo is used to calculate each star's acceleration. The stars obey the equations of motion (in the subhalo rest frame),

$$\mathbf{a}_X = -\frac{MG}{2R^2}\frac{\ln\left[1+(R/r_s)^2\right]}{\ln A/r_s}\frac{X}{R}\hat{\mathbf{R}} - \frac{v_c^2}{r}\frac{X+x'}{r}\hat{\mathbf{r}}, \tag{5.14}$$

$$\mathbf{a}_Y = -\frac{MG}{2R^2}\frac{\ln\left[1+(R/r_s)^2\right]}{\ln A/r_s}\frac{Y}{R}\hat{\mathbf{R}} - \frac{v_c^2}{r}\frac{Y+y'}{r}\hat{\mathbf{r}}, \tag{5.15}$$

$$\mathbf{a}_Z = -\frac{MG}{2R^2}\frac{\ln\left[1+(R/r_s)^2\right]}{\ln A/r_s}\frac{Z}{R}\hat{\mathbf{R}}, \tag{5.16}$$

where the first term in Equations (5.14)-(5.15) is due to the subhalo [calculated by integrating Equation (5.13) for the mass enclosed within a given radius and letting $\mathbf{a}_R = -GM(<R)/R^2$] and the second is due to the disk potential. M is the total mass of the subhalo, $\mathbf{R}$ is the vector from the

subhalo centre to the star, A is a sufficiently large radius to contain all of the subhalo mass, $\mathbf{r}'$ is the position of the subhalo relative to the galaxy centre, $\mathbf{r} = \mathbf{R} + \mathbf{r}'$ is the position of the star from the galaxy centre, and v_c is the circular speed at $0.6r_d$ due to an exponential disk (see Equation (2-169), Binney and Tremaine 1987). The Z component of acceleration has no circular rotation component.

Each timestep sees each star's velocity increment by (in the X direction) $\mathbf{v}_X(i+1) = \mathbf{v}_X(i) + \mathbf{a}_X(i)\Delta t$, and position by, $\mathbf{X}(i+1) = \mathbf{X}(i) + \mathbf{v}_X(i)\Delta t$, where Δt is the time step, for each component. With hindsight, a high order Runge-Kutta approach would have followed the orbits more accurately, however since the exact orbits are not required and the time integration not too long (6000 timesteps), this approach is acceptable. After a sufficient response time, the system reaches equilibrium with as many stars entering as leaving the subhalo's region of influence. This time is experimentally found to be $\sim 10^5$ years (for a subhalo that transits the disk in $\sim 10^6$ years).

The simulation is not realistic in the sense that the stars do not feel each other's potential and the subhalo does not experience tidal effects, however since we are interested in the heating of stars, a full N-body simulation is not required (star-star interactions are inferior to star-subhalo interactions as discussed in Section 5.9.1 and therefore this idealisation is acceptable).

The timestep, Δt, must be sufficiently small for the orbits to be representative of a true disk, but long enough to keep the computation tractable. A timestep of 50 years was found to be sufficient — doubling the time did not change the results (within Poisson errors). A realistic value for the background stellar density is desired in order to probe the overdensity statistics as accurately as possible, and the values from Holmberg and Flynn (2000) are used.

The parameters that can be varied in the simulation are the total subhalo mass, M, the scale radius, r_s, the stellar velocity dispersion, σ_0, and the subhalo speed, $v_{\rm sub}$. The scale radius, r_s, will be fixed at 10 pc, and the subhalo's speed, $v_{\rm sub} = 200$ kms^{-1}, consistent with the stripped subhalos of Benson's simulations.

5.9.1 Relaxation time

Two-body relaxation between stars will redistribute the energy obtained from the subhalo throughout the disk. Binney and Tremaine (1987) derive

a simple approximation for the timescale for such a process. Since the simulations do not treat star-star interactions, they are only representative of reality if the timescale for such interactions is long compared with the longevity of the overdensity effect or the time it takes for the subhalo to transit the disk. Otherwise the energy may be quickly dispersed into the surrounding stellar field, and the observational effect will be quite different to that predicted by the simulations.

Binney and Tremaine (1987) derive the two-body relaxation timescale based upon the density of stars and the crossing time of the system. This expression, dependent upon the number of stars in the system, N, is longer than the crossing time for $N \gtrsim 35$ and is given by,

$$t_{\rm relax} = \frac{NR}{8v \ln N} \approx \frac{0.1N}{\ln N} t_{\rm cross}, \tag{5.17}$$

where R and v are the characteristic size and internal speed of the system, and $t_{\rm cross}$ is the crossing time. Hence, for a galaxy with 10^{11} stars, the relaxation time is $t_{\rm relax} \approx 10^{10}$ years. This is the characteristic time for a star to lose half its initial momentum to field stars via two-body interactions. In the overdense region, this redistribution of energy will occur more rapidly, since the star-star impact parameters are, on average, smaller than in less dense regions. As we will see, however, the overdensities predicted by the simulations are $\delta \sim 1$ (double background density), reducing this timescale by only a factor of two.

Hence, two-body relaxation will not produce any observable effect over these timescales ($\sim 10^6$ years) and the simulations are therefore representative of reality although they do not calculate star-star interactions.

5.10 Spatial density signatures

Identifying the spatial effects of a subhalo requires careful use of the phase-space information available. A subhalo of a given mass will influence its surroundings according to its mass and spatial configuration. As such, the average overdensity in apertures of various size will be investigated, thereby optimising any potential signal.

The limiting factors for detecting subhalos will be the ability of GAIA to accurately determine distances to stars, and, given that distance uncer-

tainties do exist and increase for fainter stars, will force large distance stars to be unusable. As a consequence of this distance uncertainty, the volume of the disk available for use will decrease, making detection less likely.

As discussed in Section 5.4, the uncertainties in stellar distances approach 100 per cent for most stars beyond 5–10 kpc. Figure 5.3 showed the percentage of stars available for use at a given distance for a V=15 cutoff. Figure 5.11 shows the uncertainty in the distance measurements for the same sample. For example, at a distance of 3 kpc (which is a larger cross-section

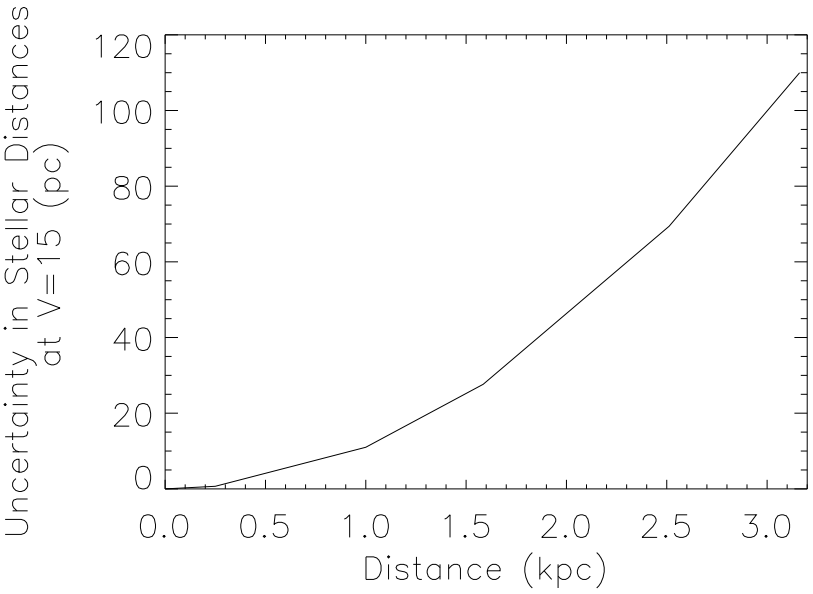

Figure 5.11: Uncertainty in distance measurement (parsecs) as a function of distance from the Sun for stars with V=15 using results from Table 5.1. By $d = 3$ kpc where only 10 per cent of stars are available for use (see Figure 5.3), the uncertainty is 3 per cent, or 110 pc.

of the disk than at 1 kpc), only stars with $M_V < 2.5$ are available, and their distance uncertainty is ∼100 pc.

To establish the largest overdensity measurable for a subhalo of given mass, the average overdensity will be calculated in regions of different size around the subhalo location. To mimic distance uncertainties in the real data, the regions in the simulations from which results are taken are enlarged to match the distance error (e.g. a region of depth 500 pc is used

to represent a distance error of 500 pc), thereby scattering unwanted stars into the region of interest and diluting the signal. This will be accomplished by considering cylindrical regions where the depth of the cylinder is the distance uncertainty.

Both a perfect experiment, where all stellar distances are known (and the region studied is a sphere), and an imperfect experiment, where the GAIA uncertainties are included (and the region studied is a cylinder) will be performed for comparison. Figure 5.12 computes the overdensity for stars within a spherical region, centred upon the subhalo, as a function of the radius of the sphere, to find the largest overdensity. This is a perfect experiment with no distance uncertainties. Figures 5.13 and 5.14, on the other hand, compute overdensities as a function of *projected* radius from the subhalo centre, and in a line-of-sight region 75 pc and 100 pc thick, respectively (i.e. distance uncertainties of Δd=75, 100pc). Note that

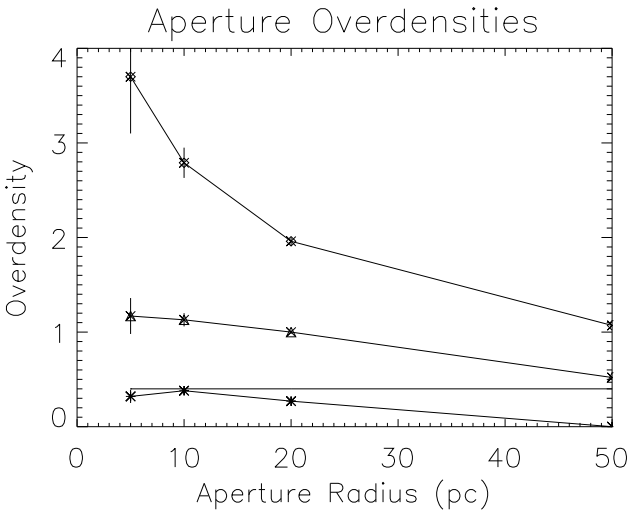

Figure 5.12: Predicted overdensity, δ, as a function of spherical radius. The three lines correspond to (from top to bottom) subhalos of mass, $M_{\rm sub} = 10^9$, 5×10^8, 10^8 $M_\odot$. The horizontal line at δ=0.4 is the threshold overdensity as discussed in Section 5.5.

the overdensities are much smaller than those found for the 10^7 $M_\odot$ point mass in Section 5.8 and are best observed over a larger region (due to the extended subhalos' more distributed nature). The horizontal line at $\delta = 0.4$ corresponds to the threshold value due to confusing intrinsic overdensities,

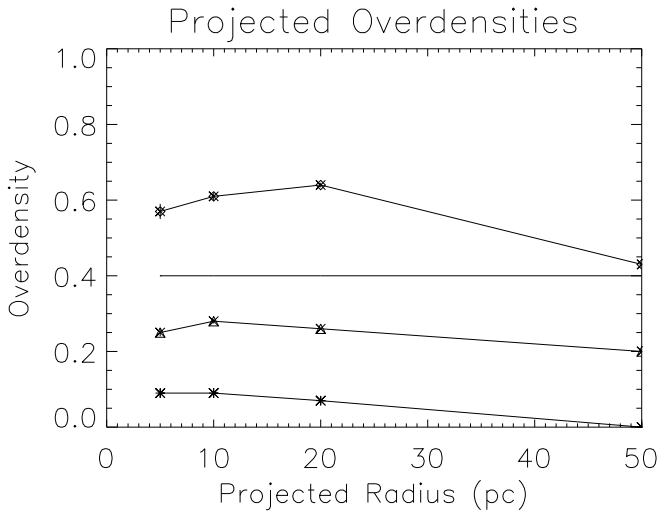

Figure 5.13: Predicted overdensity, δ, as a function of cylindrical radius, for stars within 75 projected (line-of-sight) parsecs of the subhalo. The three lines correspond to (from top to bottom) subhalos of mass, $M_{\rm sub} = 10^9$, $5{\times}10^8$, 10^8 $M_\odot$. The horizontal line at δ=0.4 is the threshold overdensity as discussed in Section 5.5.

as discussed in Section 5.5.

Results are shown for three subhalo masses, namely $M = 10^8$, $5{\times}10^8$, and $10^9 M_\odot$. Poisson uncertainties are also calculated and added to the figures to characterise the variance in background stellar density with position. These uncertainties are prominent in regions where few stars are found. The minimum stellar population labelled an overdensity here has 54 stars within a 5 pc aperture, where the background has 41 ($10^8 M_\odot$ subhalo).

In the perfect case where the stars' positions are known precisely (Figure 5.12), both the $5{\times}10^8 M_\odot$ and $10^9 M_\odot$ subhalos produce overdensities that exceed the threshold and would be detectable. The $10^8 M_\odot$ subhalo lies in the confused region. As the uncertainty on distance is increased from zero in the next two figures, the $5{\times}10^8 M_\odot$ subhalo falls below the threshold, and the $10^9 M_\odot$ is barely detectable. In addition, these calculations include all stars in the galaxy, not just the most luminous. The effect of the luminosity cutoff will now be discussed.

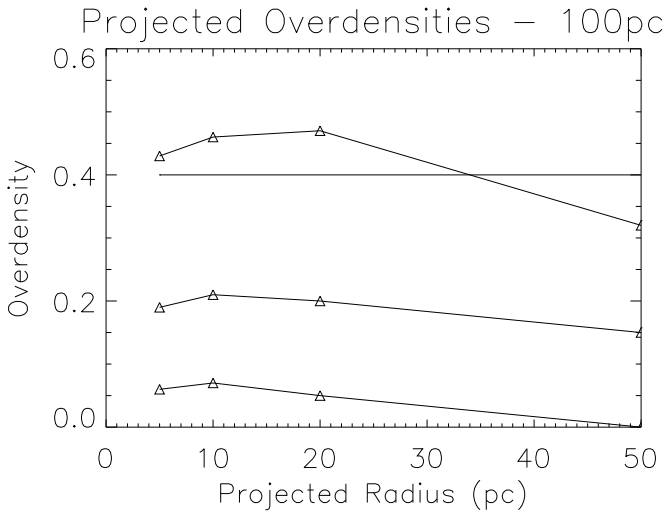

Figure 5.14: Predicted overdensity, δ, as a function of cylindrical radius, for stars within 100 projected (line-of-sight) parsecs of the subhalo. Symbols have the same meaning as in Figure 5.13.

5.10.1 Effect of distance uncertainties

The simulations show that the maximum distance uncertainty that the real data can have before these subhalos are no longer detectable above the $\delta = 0.4$ threshold are: for the $5{\times}10^8 M_\odot$, $\Delta d_{\rm max} \sim 20$ pc, and for the $10^9 M_\odot$ subhalo, $\Delta d_{\rm max} \sim 120$ pc.

One can now ask how far the subhalos can be from the observer before the distance uncertainties exceed these values. Clearly, brighter stars will reach this limit at a larger distance than fainter stars (see Table 5.1). The brightest class of stars in the Galaxy, $0 < M_V < 2.5$, will therefore be used. These account for 10 per cent of the total population (see Table 5.2) and therefore are numerous enough to produce reasonable statistics (i.e. low Poisson noise in star counts) while being bright enough to be visible at large distance. At 1, 3 and 10 kpc, these stars have apparent V-band magnitudes of (10–12.5), (12.5–15) and (15–17.5), respectively, with associated uncertainties according to Table 5.1. Given this information, and the maximum distance uncertainties quoted above, Table 5.3 displays the largest distance to a subhalo before it is undetectable, as a function of mass. Both subhalo masses are only observable within a few kiloparsecs of the Sun.

Mass	Max. Uncert.	Max. Dist.
$M_\odot$	pc	kpc
5×10^8	20	2
10^9	120	4

Table 5.3: Largest distance a subhalo can be from the observer before the uncertainties in the distances to stars predicted for the GAIA satellite, exceed the maximum uncertainty allowable for a subhalo of a given mass, M, to produce an overdensity in excess of the $\delta = 0.4$ threshold.

5.10.2 Available fraction of disk

The uncertainty in the distances to stars, particularly beyond ∼5 kpc, reduces the subhalo signal significantly. Table 5.4 summarises the maximum distance to a subhalo before it becomes undetectable, and includes an estimate of the fractional volume of the disk in a detectable region. Given the

Mass	Max. Dist.	δ	Best Aperture	Disk Volume	No. Reqd
$M_\odot$	kpc		pc	%	
5×10^8	2	0.50	20	1.2	4000
10^9	4	0.48	20	8	600

Table 5.4: Results for the spatial overdensities of stars for a given subhalo mass. The radius of the cylindrical aperture where the best overdensity is found is given, and the maximum distance from the Sun the subhalo can be before it falls below the detection limit. Given these values, only a small fraction of the disk volume is available. The final column lists the number of subhalos of a given mass or greater required to reside in the Galactic halo for one to be expected to pass within the maximum distance.

small disk fractions, the number of subhalos one requires for it to be likely that a subhalo is passing within the maximum distance becomes quite large. Assuming that the disk occupies 2 per cent of the halo's volume and 8 per cent of the disk is available (Table 5.4), there needs to be $\sim 1/(0.02\times0.08)$ $\sim$ 600 subhalos with $M > 10^9 M_\odot$. As shown is Section 5.6.2, this number is two orders of magnitude more than expected from N-body simulations. Spatial signatures therefore appear to be too weak to be detected with the uncertainties of GAIA.

5.11 Velocity signatures

A subhalo transit shifts and broadens the velocity distribution function. This signal will be most evident in the stars closest to the subhalo, and in the Z-component of the velocity (this is where the bulk of the momentum is transferred since the perpendicular kicks on any individual star add up to zero over time). A spatial cut is therefore used to isolate such a region.

Stars will be both accelerated toward the subhalo and swept along behind it, producing a broadened distribution function. Figure 5.15 plots the phase-space positions $(Z - v_Z)$ of stars at the end of a simulation with a $10^{10} M_\odot$ subhalo (large mass to exaggerate effect). The stars' velocities have been

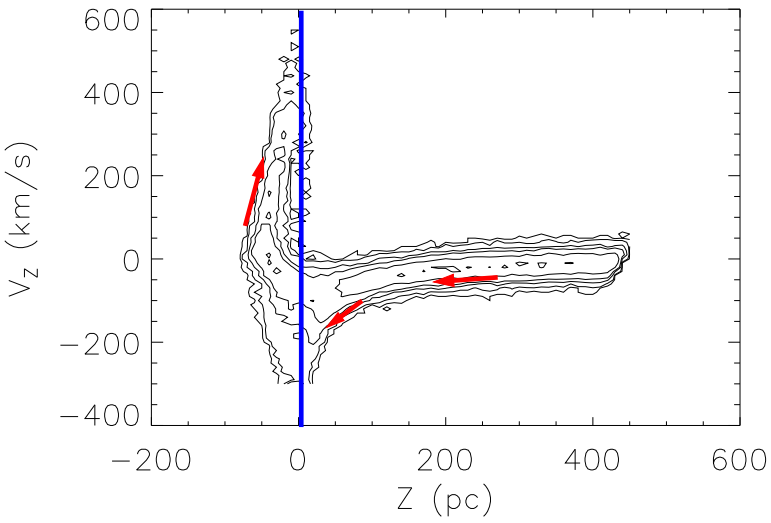

Figure 5.15: Contour plot of phase-space positions $(Z - v_Z)$ of stars at the end of a simulation (observer's frame in velocity). The subhalo has mass, $M = 10^{10} M_\odot$. The red arrows show the direction of motion of the stars, and the blue line denotes the subhalo's spatial position. Contours are [1, 5, 20, 40, 100, 200] stars per 100 pc kms^{-1}.

shifted to the observer's frame (where they are centred around $v_Z = 0$). As the stars are accelerated toward the subhalo, their trajectories move from positive Z values to zero, and their velocities become more negative. As they pass $Z = 0$ (scatter past the subhalo), they decelerate again and return to their initial position (see red arrows). In addition, since the subhalo is being

slowed by the stars, its momentum is transferred to them and they attain, on average, a velocity in the direction of the subhalo's motion. Clearly, a velocity cut in the region close to the subhalo improves the signal from this wide distribution.

Accurate proper motions are required when measuring the Z-component of velocity. Table 5.1 shows that for stars within 10 kpc, the change in the stars' Z speed is $\Delta v_Z = 0.1$–15 kms^{-1}, dependent upon magnitude — accurate compared with the distance uncertainties at 10 kpc. The isolation of a spatial region requires good estimates of the stellar distances, and this will again be the main source of uncertainty. However, if subhalos are able to scatter stars to high speed, the number of bright stars observable at large distance will also be a factor.

A population with a Maxwellian velocity distribution contains stars with speeds above the escape speed for the system. These stars will evaporate from the system and can mimic the subhalo scattering if the subhalo, due to the uncertainty in stellar locations, cannot be localised to a particular region (escaping stars are distributed uniformly, whereas the subhalo produces localised heating). Once these stars have escaped, this region of the velocity distribution is re-populated over a relaxation time via two-body interactions. Binney and Tremaine (1987) estimate that for a system with one-dimensional velocity dispersion, σ, and a Maxwellian velocity distribution, the escape speed is $\overline{v_e^2} = 4\overline{v^2} = 12\sigma^2$ and that ~ 0.7 per cent of stars in the system have at least this speed. Hence, in a cylinder of, for example, 30 pc radius and 250 pc depth, there are $\sim 0.007 \times 10^{10} \times V/V_T \sim 300$ high-speed stars, where $N = 10^{10}$ is the total number of stars in the Galaxy and V/V_T is the volume fraction of the disk in the cylinder. Hence, in a region of this size, in excess of 300 stars would need to be heated by a subhalo and then observed to be distinguished from stars in the high-speed tail of the distribution function. This is another form of thresholding. To be confident of the detection of a subhalo, the number of heated stars observed, $N_{\rm stars}$, needs to be greater than the number in the high-speed tail,

$$N_{\rm stars} > 0.0014 r_{\rm pc}^2 \Delta d_{\rm pc}, \tag{5.18}$$

where r is the cylinder's radius, and Δd is the distance uncertainty, both expressed in parsecs. Note that evaporating stars will escape in random

directions, not necessarily with a large velocity component in the direction of the subhalo's motion (here the Z axis), and therefore expression (5.18) is a safe lower limit to the number that need to be observed.

Figure 5.16 displays the Z component velocity distribution function (in the observer's frame) for stars scattered from a $10^9 M_\odot$ (top left), a $5{\times}10^8 M_\odot$ (top right), and $10^8 M_\odot$ (bottom) subhalo, within 30 pc (XZ) of their centre, and at a line-of-sight distance of 30, 50 and 75 pc (Y, due to distance uncertainties). Clearly, the $10^9 M_\odot$ subhalo distributes the stars the most

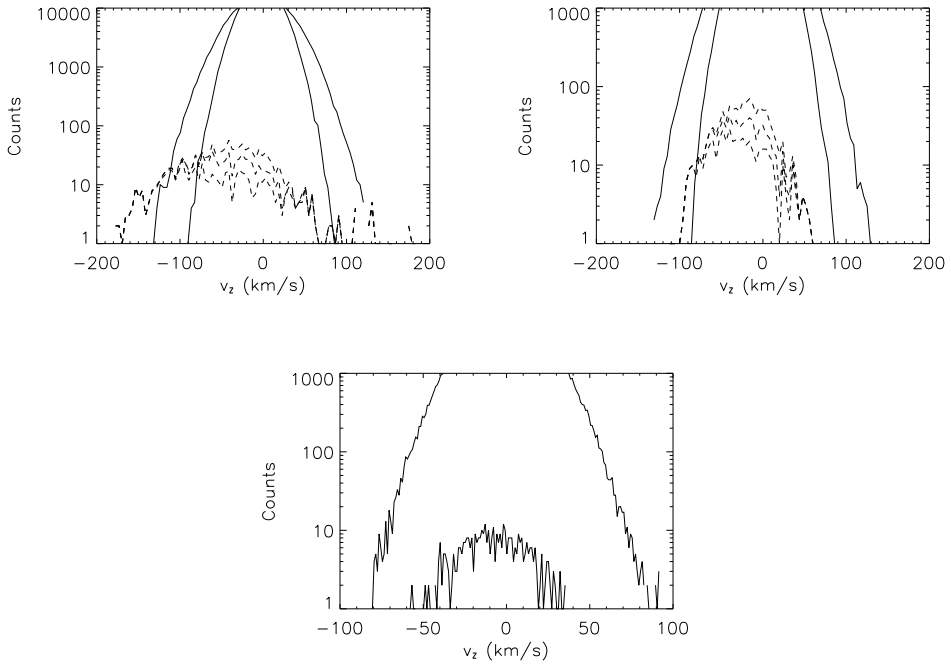

Figure 5.16: (Top left) Z component of the velocity distribution function of stars (observer's frame) for a $10^9 M_\odot$ subhalo. Curves are for stars within a cylinder 30 pc in radius (XZ) and 30, 50 and 75 pc (dashed, lie on top of each other) line-of-sight from the subhalo. Also shown are the original distribution function (solid narrow) and an example distribution function where $\sigma = 1.5\sigma_0$ (solid broad, heating due to molecular cloud scattering). (Top right) Same except for $5{\times}10^8 M_\odot$ subhalo. (Bottom) Same except for a $10^8 M_\odot$ subhalo.

efficiently in velocity space. The threshold velocity dispersion, $\sigma = 1.5\sigma_0$, due to scattering off massive molecular clouds (Section 5.5), is also shown for comparison. Only the $10^9 M_\odot$ subhalo is able to heat stars more efficiently

than molecular clouds, while the effect of a $5{\times}10^8 M_\odot$ subhalo can be confused with heating by molecular clouds. The $10^8 M_\odot$ subhalo is unable to heat stars beyond the Maxwellian distribution with $\sigma = 20$ kms^{-1}.

I will now concentrate on the two more massive subhalos and their observability over the high-speed tail of the distribution. As the uncertainty in the distance to the subhalo increases, the number of stars in the high-speed tail will increase and eventually exceed the number that are heated by the subhalo itself.

For a range of distance uncertainties, the number of stars with speeds in excess of the molecular cloud threshold (proper motion, $|v_Z| > 100$ kms^{-1}) and the number of stars in the high-speed velocity tail in the same region are calculated, according to the results from Binney and Tremaine (1987) and Equation (5.18). This places a lower limit on the number of stars that need to be measured to ensure the heating is caused by the subhalo. Figure 5.17 shows the total number of simulated high-speed stars in a region as a function of distance uncertainty compared with the number of stars in the high-speed tail of the DF. The $5 \times 10^8 M_\odot$ subhalo can be detected with a distance uncertainty up to 500 pc, since this is where the two curves cross, and the $10^9 M_\odot$, up to 2 kpc, before there are more stars in the high-speed tail of the DF.

It remains now to compare these uncertainties with the GAIA predictions of Table 5.1 to find the maximum distance the subhalo can be from the observer before the uncertainties are too large. These results are shown in Table 5.5. These distances are larger than those found for the spatial

Mass	Max. Uncert.	Max. Dist.
$M_\odot$	pc	kpc
$5{\times}10^8$	500	5
10^9	2000	8

Table 5.5: Largest distance a subhalo can be from the observer before the uncertainties in the distances to stars predicted for the GAIA satellite, exceed the maximum uncertainty allowable. At larger distance, there are too many heated stars to distinguish between a subhalo heating and the high-speed tail of the Maxwellian velocity distribution.

domain and the velocity domain is therefore more useful for the detection of subhalos — the fraction of the disk available for subhalos to be found and therefore the likelihood of detection, is larger.

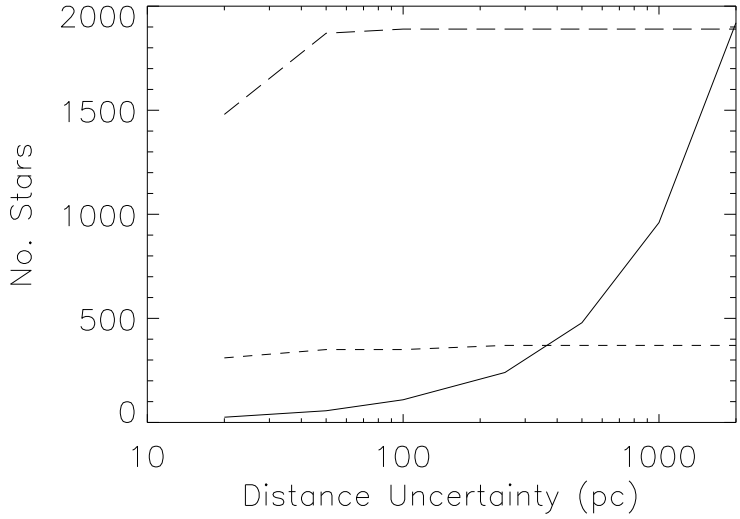

Figure 5.17: Number of stars with $|v_Z| > 100 kms^{-1}$ as a function of uncertainty in distance centred on the subhalo for the $5 \times 10^8 M_\odot$ (short-dashed) and $M = 10^9 M_\odot$ (long-dashed) subhalo. Also shown are the number of evaporating stars in the same cylindrical region (solid lines). The maximum uncertainty for the $5 \times 10^8 M_\odot$ ($M = 10^9 M_\odot$) subhalo is 500pc (2kpc) before the subhalo is indistinguishable from the background of high speed stars.

5.11.1 Phase-space signature

Although there are sufficient high-speed tail stars in a cylinder of depth 2 kpc to exceed the number of stars heated by a 10^9 $M_\odot$ subhalo, only a small percentage (0.3%) of stars in a Maxwellian distribution are more than 3σ from the mean. Hence, if the subhalo can heat stars to a higher speed than expected for a Maxwellian distribution, they may be distinguished from background stars. This can be investigated by plotting the $Z - v_Z$ phase-space distribution and adding the effects of heating by molecular clouds, the GAIA distance uncertainties and the GAIA proper motion uncertainties in turn.

Figure 5.18 displays the phase-space stellar distributions for the 10^9 $M_\odot$ (left column) and $5 \times 10^8 M_\odot$ (right column) subhalo. The contours for each plot are [1, 10, 100, 1000, 10000] stars per 100 pc kms^{-1}. The top row shows the density of stars at the end of the simulation with the Z velocity

dispersion set to the background value of $\sigma = 20\text{kms}^{-1}$ and for stars within 500 pc (projected) of the subhalo. Both the subhalos show heating of the stars here.

The second row adds heating due to molecular clouds, here modelled by adding stars with $\sigma = 30\text{kms}^{-1}$ (note that uniform heating across the disk would not occur as shown here — this plot is intended to show the magnitude of the effect and so the heating is plotted uniformly). The heating due to the $5{\times}10^8 M_\odot$ subhalo is masked by this molecular cloud heating (also seen in Figure 5.16).

The final row shows the results for a 10^9 $M_\odot$ subhalo placed at 20 kpc from the Sun where the following effects have been added: (i) 90 per cent of the stars at the subhalo distance have been removed since only the brightest are now observable by GAIA, (ii) the molecular cloud heating with $\sigma = 30\text{kms}^{-1}$ is included (with a larger column through the disk at a distance of 20 kpc, the probability of molecular cloud heating increases), and (iii) the proper motion measurements (v_Z) of stars at the subhalo location are Gaussian smeared to $\Delta v_Z = 30\text{kms}^{-1}$, in accordance with the GAIA predictions from Table 5.1. Hence, the combination of these effects almost masks the subhalo heating signal (a small excess of stars at the known location of the subhalo is still visible here). For distances less than 20 kpc, the subhalo signal becomes stronger as the GAIA measurements improve.

These results suggest the velocity domain is more useful than the spatial to isolate subhalos moving through the Galactic disk. The disk volume fraction within 5–8 kpc of the Sun is 10–20 per cent. This still requires $\sim$100–300 subhalos of sufficient mass to expect one to be passing through this region now. For a $5{\times}10^8 M_\odot$ subhalo, this figure is still an order of magnitude too high. For a 10^9 $M_\odot$ subhalo at 20 kpc, the subhalo distance cannot be determined, the proper motion uncertainty is large ($\sim 30\text{kms}^{-1}$) and only a small fraction of stars are bright enough for observation. Unfortunately, there is a $\sim$10 per cent chance of a subhalo with such high mass being within the Milky-Way disk at any one time. Therefore, although a 10^9 $M_\odot$ subhalo may still be observable at a distance of 20 kpc, there are too few to expect one to be observed.

5.12 Discussion & conclusions

If massive black holes threaded the disk, these would have an observable effect with GAIA, but the extended nature of true subhalos makes detecting this effect an extremely difficult task, primarily due to GAIA uncertainties combined with the expected small number of massive subhalos close to the Sun in the disk (∼10 per cent chance of a 10^9 $M_\odot$ subhalo being within 20 kpc of the Sun and within the disk). Confusion plays a lesser role in reducing any potential signal.

The velocity domain was found to produce more prominent signatures than the spatial domain, due to the subhalos' efficiency at scattering stars to very high speeds. In the spatial domain, a $5\times10^8 M_\odot$ subhalo would need to move within 2 kpc of the Sun for detection, and a $10^9 M_\odot$ subhalo within 5 kpc. In the velocity domain, where proper motions are well measured by GAIA, they would be observable to ∼5 kpc and ∼20 kpc, respectively. In both cases the limiting factor is the GAIA distance determination uncertainty, and the lack of very bright stars ($M_V < 0$) in the Galaxy.

The results presented above are also likely to be the best case scenario. Assuming the subhalos remain spherically symmetric during all transits overestimates their dynamical influence since the majority of the mass remains in a compact region. Subhalos are rapidly stripped by tidal interactions into long streams (see for example, Majewski et al. 2003), reducing their sphere of influence as they are stretched into a lower density stream.

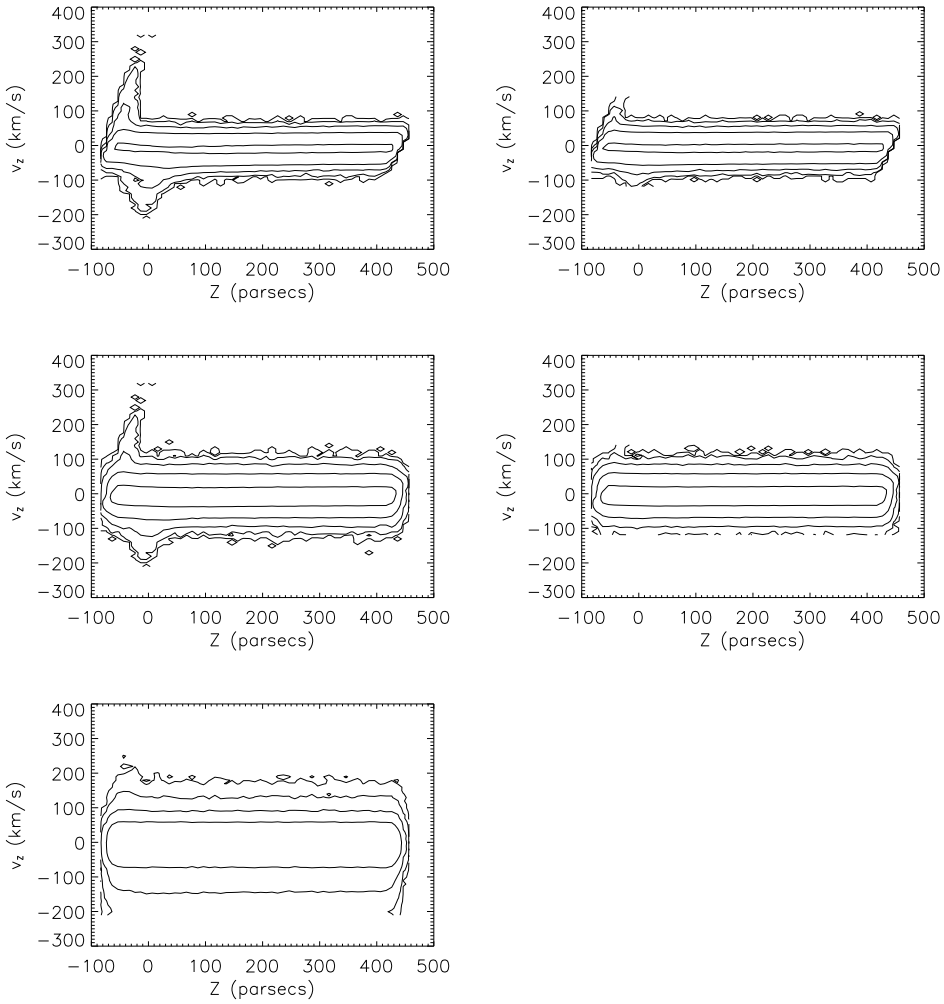

Figure 5.18: Contour plots of $Z - v_Z$ phase space for stars in the disk at the simulation end. The left (right) column shows results for the 10^9 $M_\odot$ ($5{\times}10^8 M_\odot$) subhalo. The rows show: (top) contours for background stellar velocity dispersion, $\sigma = 20\mathrm{kms}^{-1}$ and stars within 500 pc (projected) of the subhalo location; (centre) inclusion of molecular cloud heating modelled as heating of disk to have $\sigma = 30\mathrm{kms}^{-1}$; (bottom) subhalo placed at a distance of 20 kpc where the proper motion uncertainty is $\Delta v_Z = 30\mathrm{kms}^{-1}$, only $\sim$10 per cent of stars are bright enough to be observed and the probability of molecular cloud heating is high. All plots have contours of [1, 10, 100, 1000, 10000] stars per 100 pc kms^{-1}.

CHAPTER 6

Collapsed and Extended CDM Halos in Softened N-body Gravity

The statistical mechanics of N cold dark matter (CDM) particles interacting via a softened gravitational potential is reviewed in the microcanonical ensemble and mean-field limit. A phase diagram for the system is computed as a function of the total energy E and gravitational softening length ϵ. For softened systems, two stable phases exist: a collapsed phase, whose radial density profile $\rho(r)$ is a central Dirac cusp, and an extended phase, for which $\rho(r)$ has a central core and $\rho(r) \sim r^{-2.2}$ at large r. It is shown that many N-body simulations of CDM halos in the literature inadvertently sample the collapsed phase only, even though this phase is unstable when there is zero softening. Consequently, there is no obvious reason to expect agreement between simulated and observed profiles unless the gravitational potential is appreciably softened in nature.

6.1 Introduction

Cold dark matter (CDM) theory successfully describes many aspects of the formation of large-scale structure in the universe (Peebles 1982; Davis et al. 1985). However, mismatches do exist between its predictions and observations, such as the cusp-core controversy, missing satellites (Klypin et al. 1999; Moore et al. 1999a) and the angular momentum (Navarro and Benz 1991; Thacker and Couchman 2001) problems. In particular, the cusp-core issue has provoked much debate. CDM simulations consistently yield density profiles with steeper inner slopes (power-law exponent between -1 and -1.5) than observational studies which have found a range of slopes, including constant density cores in dark matter dominated low surface brightness galaxies (de Blok et al. 2001b) and shallow slopes in clusters with gravitationally lensed arcs (Sand et al. 2004). These results, among others, have initiated discussion about the role of baryons in softening simulated cores (Athanassoula 2004; Shen and Sellwood 2004) and the observational effects that may mask cusps in low surface brightness galaxies (de Blok et al. 2001b; Swaters et al. 2003). Recent N-body results demonstrate that, at the current resolution of simulations, the central power-law exponent does not converge to a universal value (Navarro et al. 2004), but may be becoming shallower closer to the centre.

In numerical simulations, a softened gravitational potential is used to prevent the macro-particles (10^5–$10^7 M_\odot$) from experiencing artificially strong two-body interactions (Navarro et al. 1996,for example). The softening length, ϵ, is chosen to maximise the resolution while suppressing two-body effects over the simulation running time. In view of the ongoing disagreement regarding the form of $\rho(r)$, it is important to clarify *analytically*, by a code-independent argument, whether the choice of ϵ affects the physics of the system and hence $\rho(r)$. In this work, the framework of statistical mechanics is employed (Padmanabhan 1990), drawing upon recent results on phase transitions in N-body systems with attractive power-law potentials (Ispolatov and Cohen 2001; de Vega and Sánchez 2002). Self-gravitating particles behave qualitatively differently to many other statistical systems because gravity is an unscreened, long-range force. They are best examined within the microcanonical ensemble, where the energy and number of particles are fixed and phases with negative specific heat are allowed. The

results of the classical theory of self-gravitating, N-body systems are applied to demonstrate the effects of introducing a short distance cutoff in numerical simulations (in particular the effect on stability).

The study of the thermal stability of self-gravitating systems has a long history. Lynden-Bell and Wood (1968) showed that spherical systems of point particles in a box with reflecting walls are gravitationally unstable below a critical temperature, collapsing catastrophically to a central point. Aronson and Hansen (1972) generalised this work to a spherical system of N classical hard spheres in contact with a heat bath, showing the gravothermal instability to be a general feature of self-gravitating systems held at a constant temperature. Hertel and Thirring (1971), investigating point fermions obeying the Pauli Exclusion Principle, showed that a *stable* low temperature phase can exist if the gravitational potential is softened, transforming the gravothermal instability to a phase transition to the low temperature phase. In this chapter, these results are extended and used to reinterpret some of the ambiguous results of numerical simulations of CDM halos discussed above. A detailed comparison with preceding analytic work is presented in Section 6.3.2.

Section 2 briefly reviews the formalism for treating N self-gravitating collisionless particles statistically. In Section 3, the formalism is applied to compute $\rho(r)$ analytically as a function of E, the total energy, and ϵ. The result is a thermodynamic phase diagram that contains both collapsed and extended halos. In Section 4, published N-body simulations are located on the phase diagram and show they are biased exclusively towards the collapsed phase. This phase is unstable for $\epsilon = 0$, suggesting that collapsed halos are an artificial by-product of the softened potential; there is no obvious reason to expect agreement between simulated and observed profiles unless the gravitational potential is appreciably softened in nature.

This work is not intended to reproduce realistic CDM halos with non-zero angular momentum and hierarchical clustering, but rather to demonstrate in a code-independent manner how the softening used in N-body simulations may artificially alter the density profiles found.

6.2 Statistical mechanics of N self-gravitating particles

6.2.1 Density of states in the microcanonical ensemble

The properties (e.g. energy, entropy) and collective behaviour (e.g. gravothermal catastrophe) of a self-gravitating gas of DM particles in thermodynamic equilibrium take different values when computed in different statistical ensembles because the long-range nature of the gravitational potential renders the system inseparable from its environment (Padmanabhan 1990; Ispolatov and Cohen 2001; de Vega and Sánchez 2002). This work follows previous studies by considering the self-gravitating gas in the microcanonical ensemble (MCE), whose features are constant energy, volume and particle number. Particles do not evaporate from the system over time and the walls of the container are perfectly reflecting. The MCE is more appropriate than the canonical ensemble (CE) for three reasons: (i) it is unclear how to construct an external heat bath for a long-range potential, required by the CE, because the system interferes with the environment (Huang 1987); (ii) states with negative specific heat are inaccessible in the CE (Padmanabhan 1990); and (iii) the equilibrium density profile in the violently relaxed (Smoluchowski) limit is the singular isothermal sphere in the CE, contrary to observations (Sire and Chavanis 2002).

The density of states, $g(E)$, is the volume of the $(6N-1)$-dimensional surface of constant energy E in phase space $(\mathbf{x}_1, ..., \mathbf{x}_N, \mathbf{p}_1, ..., \mathbf{p}_N)$, where $(\mathbf{x}_i, \mathbf{p}_i)$ are the co-ordinates and momenta of the i-th particle. At any one moment, the system sits at one point in the $6N$-dimensional phase space. One has,

$$g(E) = \frac{1}{N!} \int \delta \left[E - \sum_{i=1}^{N} \frac{p_i^2}{2m} - \sum_{i \neq j}^{N} V(\mathbf{x}_i, \mathbf{x}_j) \right] d^{3N}p d^{3N}x, \qquad (6.1)$$

where the first and second summations give the kinetic and potential energy, and the integral is over phase space volume. The gravitational potential, V, is given by $V = -Gm^2|\mathbf{x}_i - \mathbf{x}_j|^{-1}$ for particles of equal mass m, or if the potential is artificially softened with characteristic length ζ, by $V = -Gm^2[(\mathbf{x}_i - \mathbf{x}_j)^2 + \zeta^2]^{-1/2}$.

The thermodynamic entropy (up to a constant) S and the temperature T of the system are defined in terms of $g(E)$:

$$S(E) = k_B \ln g(E), \tag{6.2}$$

$$\beta(E) = \frac{1}{k_B T} = \frac{\partial S(E)}{\partial E}. \tag{6.3}$$

These quantities are hard to interpret if assigned to a system far from equilibrium. Note that $g(E)$ diverges for ζ=0 and $N > 2$; any two particles can be brought arbitrarily close together, liberating an infinite amount of potential energy, so that the co-ordinate space integral diverges (Padmanabhan 1990). This is a serious problem because it is impossible to achieve thermodynamic equilibrium if $g(E)$ diverges; the system does not have time to sample the infinite number of possible microstates with equal probability (Chabanol et al. 2000). If the dark matter particles are fermionic, the Pauli Exclusion Principle prevents this problem. However, the fraction of the phase space volume sampled by N mildly relativistic CDM particles in a time t, given by $(ct/R)^{3N}(\zeta c^2/2GmN^{4/3})^{3N/2}$, is exceedingly small for most proposed CDM particles, e.g. $\zeta^2/m \sim 8{\times}10^{-(29-26)} m^2/GeV$ for self-interacting dark matter (Spergel and Steinhardt 2000).

6.2.2 Integral equations for $\rho(r)$ in the mean-field limit

The density of states is evaluated in the continuum (mean-field) limit by integrating over momentum and then expressing the remaining configurations as a functional integral over possible density profiles $\rho(x)$ (de Vega and Sánchez 2002; Ispolatov and Cohen 2001),

$$g(E) = \int D\rho \int_{-\infty}^{+\infty} \frac{d\gamma}{2\pi i} \int_{-\infty}^{+\infty} \frac{d\beta}{2\pi i} \exp[N s(\rho, \xi, \gamma, \beta)], \tag{6.4}$$

where the effective dimensionless action

$$\begin{aligned} s(\rho, \xi, \gamma, \beta) &= \beta\xi + \frac{\beta}{2} \int\int \frac{\rho(\mathbf{x}_1)\rho(\mathbf{x}_2)}{|\mathbf{x}_1 - \mathbf{x}_2|}\, d^3\mathbf{x}_1 d^3\mathbf{x}_2 \\ &+ \gamma \int \rho(\mathbf{x}) d^3\mathbf{x} - \gamma - \frac{3}{2}\ln\beta - \int \rho(\mathbf{x}) \ln \rho(\mathbf{x})\, d^3\mathbf{x} \end{aligned} \tag{6.5}$$

and dimensionless energy

$$\xi = ER/GM^2 \tag{6.6}$$

are quantities defined in Ispolatov and Cohen (2001). In (6.4) and (6.5), and throughout the remainder of this paper, the density profile and co-ordinates $\mathbf{x}$ are written as dimensionless quantities, relative to the total mass $M = Nm$ and outer radius R of the system, with $x = \mathbf{x}/R$ and $\epsilon = \zeta/R$.

Upon evaluating the functional integral by a saddle point method (which involves extremising the action), (6.4) reduces to three coupled integral equations describing the density profile $\rho(x)$, the central density ρ_0 and the inverse temperature $\beta = 1/k_B T$. For a Newtonian potential, one has

$$\rho(x) = \rho_0 \exp\left[\frac{2\pi\beta}{x}\int_0^1 \rho(x_1)x_1(|x+x_1| - |x-x_1|)\,dx_1\right], \tag{6.7}$$

$$\frac{1}{\rho_0} = \int_0^1 4\pi x_2^2 dx_2 \exp\left[\frac{2\pi\beta}{x_2}\int_0^1 \rho(x_1)x_1(|x_2+x_1| - |x_2-x_1|)\,dx_1\right] \tag{6.8}$$

$$\frac{3}{2\beta} = \xi + 4\pi^2\int_0^1\int_0^1 \rho(x_1)\rho(x_2)x_1x_2(|x_1+x_2| - |x_1-x_2|)\,dx_1dx_2. \tag{6.9}$$

Note the factor $4\pi x_2^2$ in (6.8) was omitted due to a typographical error by Ispolatov and Cohen (2001). The solutions to these equations describe the density profile, entropy and temperature of an equilibrium system for a given energy. To obtain analogous equations for the softened potential, we note (by analogy) that they are of order $O(\eta^2\epsilon, \eta\epsilon^2)$ in the CE, where $\eta = Gm^2N/RT$ in the CE is a proxy for ξ^{-1} in the MCE. Note that the classical thermodynamic limit (N/V constant as $N, V \to \infty$) does not apply for gravitating systems, but are finite if proportional to $N/V^{1/3}$ as $N, V \to \infty$.

6.3 Radial density profile of a CDM halo

Equations (6.7)–(6.9) are solved for the radial density profile $\rho(x)$ by the following iterative relaxation scheme (Ispolatov and Cohen 2001): given the current iterate of the profile, $\rho^{(i)}(x)$, apply (6.9), (6.8) and (6.7) to compute $\beta^{(i+1)}$, $\rho_0^{(i+1)}$ and $\rho^*(x)$ in that order, then apply $\rho^{(i+1)}(x) = \sigma\rho^*(x) + (1-\sigma)\rho^{(i)}(x)$ until the convergence criterion

$$4\pi \int_0^1 |\rho^{(i+1)}(x) - \rho^{(i)}(x)| x^2 \, dx < \delta, \tag{6.10}$$

is satisfied. Typically, $\delta = 10^{-6}$ and $0.01 \leq \sigma \leq 1$ ($\delta \ll \sigma$) are adopted in this work. The softening can be introduced into this scheme in two ways: (i) as a nonzero lower limit of integration in the integrals in (6.7)–(6.9); and (ii) in the potential, $V = -Gm^2[(\mathbf{x}_i - \mathbf{x}_j)^2 + \epsilon^2]^{-1/2}$. Both approaches were tested and found to produce qualitatively similar behaviour; the latter is concentrated upon in this work as it is more closely allied to N-body simulations.

6.3.1 Stable versus unstable phases: $\epsilon = 0$

With no softening present in the gravitational potential, a stable solution of (6.7)–(6.9) formally exists above a cutoff energy $\xi > \xi_c \simeq -0.335$. The density profile of the halo exhibits a flat central core, with $d\rho/dx \to 0$ as $x \to 0$, and near-isothermal wings, with $\rho(x) \propto x^{-\alpha}$ ($\alpha \simeq 2.2$) as $x \to \infty$, as illustrated in Figure 6.1. This agrees with the solution for secondary infall onto a spherical perturbation (Bertschinger 1985) and behaves asymptotically like the spherical, thermally conducting polytrope (Lynden-Bell and Eggleton 1980) and infinite-dimensional Brownian gas (Sire and Chavanis 2002).

For $\xi < \xi_c$, a formal solution of (6.7)–(6.9) does not exist. The entropy and temperature jump discontinuously below this cutoff energy as shown in Figure 6.2. This is the well-known gravothermal catastrophe (Antonov 1962). Note that for $\xi = -1/4$, the singular isothermal sphere $\rho(x) = (4\pi x^2)^{-1}$, $\rho_0 = (4\pi e^2)^{-1}$ and $\beta = 2$ is always a solution of (6.7)–(6.9), as can be verified analytically, but it is not stable and so the iterative procedure never converges to it, but rather to Figure 6.1. Figure 6.2 displays the entropy and inverse temperature in the stable extended phase.

6.3.2 Collapsed versus extended phases: $\epsilon \neq 0$

If the gravitational potential is softened, a stable phase exists for all values of ξ. For $\xi > \xi_c^{(+)} \simeq 0$, the halo is extended as in Figure 6.1 with a flat core and near-isothermal envelope, $\rho(x) \propto x^{-2.2}$. However, for $\xi < \xi_c$, the halo is collapsed. Figure 6.3 displays the density profile of such a collapsed halo for $\epsilon = 10^{-4}$ (note that both axes are logarithmic). The halo has a

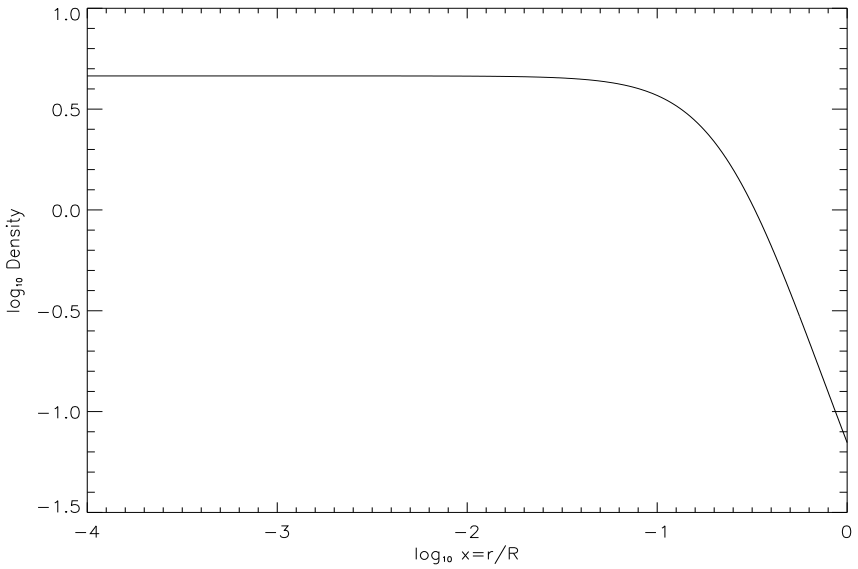

Figure 6.1: Equilibrium radial density profile for a system with $\xi > \xi_c$ and $\epsilon = 0$. The profile is similar to a softened isothermal sphere, but with $\rho(x) \propto x^{-2.2}$ as $x \to 1$.

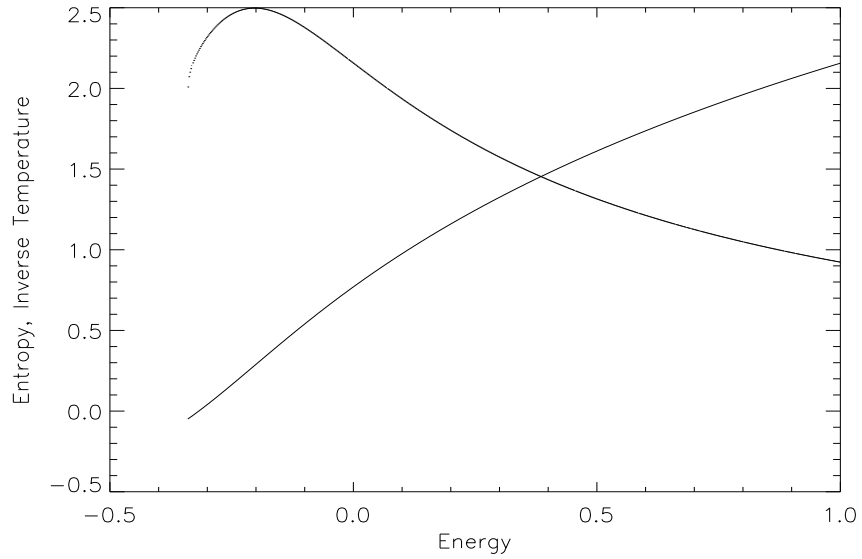

Figure 6.2: Dimensionless entropy (monotonically increasing) and inverse temperature (peaked curve) as a function of energy for $\xi > \xi_c$ when the gravitational potential is not softened. Below $\xi_c \simeq -0.335$ no stable solution exists.

steep Dirac peak ("cusp") at $x = 0$: $\rho(x)$ is flat for $x \lesssim \epsilon$, decreases as a large inverse power of x for $x \gtrsim \epsilon$ and flattens for $x \to 1$. For intermediate energies in the range $\xi_c \leq \xi \leq \xi_c^{(+)}$, the system is bistable: the halo can be either extended or collapsed depending on the initial conditions and the route to equilibrium. Figure 6.4, a plot of entropy and temperature as a function of energy, illustrates this hysteretic behaviour. $S(\xi)$ and $\beta(\xi)$ jump discontinuously at both $\xi_c^{(+)}$ and ξ_c. If ξ enters the intermediate range from below, the halo remains collapsed until ξ exceeds $\xi_c^{(+)}$. Alternatively, if ξ enters from above, the halo remains extended until ξ is reduced below ξ_c.

The critical energy ξ_c, and the collapsed and extended profiles obtained, are consistent with previous analyses (Antonov 1962; Aronson and Hansen 1972; Padmanabhan 1990). For example, Aronson and Hansen (1972) find a phase transition at $\xi \simeq -0.3$, consistent with the value found here $\xi_c \simeq -0.335$, and a critical reciprocal temperature at the transition in the range $\beta_c = 1.2 - 1.6$ for $\epsilon = 10^{-20}$, consistent with $\beta \sim 2$ in this paper ($\epsilon = 10^{-4}$). A more precise comparison is prohibited by the adoption of the CE rather than the MCE in most previous work. The van der Waals model proposed by Padmanabhan (1990) is an exception; it is examined in detail in the following section. The phenomenon of bistability was overlooked until the work of Ispolatov and Cohen (2001).

The behaviour of the system depends somewhat on the choice of the relaxation parameter σ, defined at the start of this section. Table 6.1 displays the minimum softening length for which the system makes the transition to a stable collapsed phase, for a given value of σ. The phase transition from the extended to the collapsed phase is increasingly delicate for decreasing softening: for larger values of σ the system is less likely to reach the critical point where the phase transition occurs and therefore remains in the extended phase. Although this is a numerical effect, it potentially reflects the relative likelihoods of the possible routes that the real system can take to equilibrium.

It is conceivable that for all $\epsilon>0$ a collapsed stable phase can exist — although it is highly unlikely in nature — but cannot be probed by this numerical route. When $\epsilon = 0$ (pure gravity), the density of states is formally infinite and a collapsed phase is unlikely to exist. In this work we are merely interested in showing the artificial behaviour of the system introduced by macroscopic softenings of the gravitational potential, and not investigating

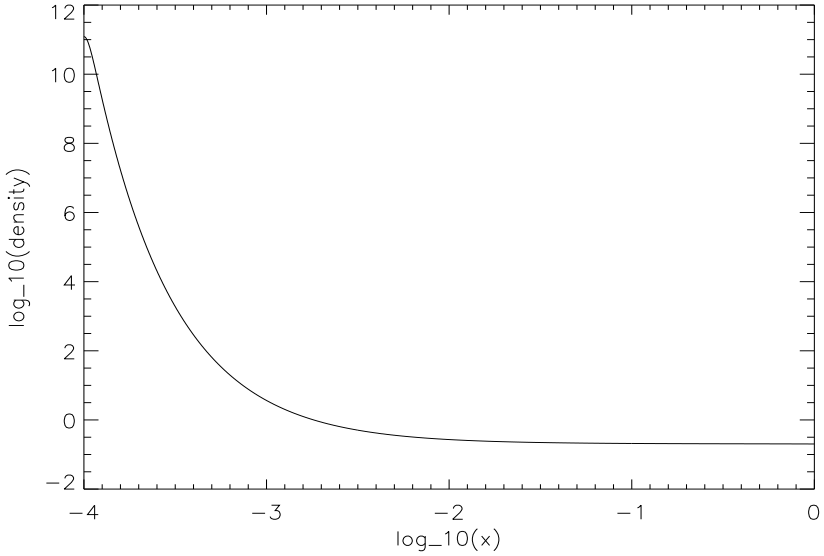

Figure 6.3: Radial density profile for the collapsed phase of a potential with softening $\epsilon = 10^{-4}$.

σ	ϵ_{min}
0.01	10^{-14}
0.03	10^{-10}
0.05	10^{-6}
0.1	10^{-2}

Table 6.1: Minimum softening, ϵ_{min}, for which a stable collapsed solution is found for a given relaxation parameter σ.

the effects of microscopic softenings (e.g. interaction cross-sections).

6.3.3 van der Waals equation of state

An alternative, phenomenological way to model a CDM halo interacting via a softened gravitational potential is to solve the Lane-Emden equation for a nonideal, isothermal gas obeying a van der Waals equation of state, $P \propto \rho T(1-\rho/\rho_{\rm m})^{-1}$, where P denotes the pressure and $\rho_{\rm m}$ is the maximum density allowed by hard-sphere packing of the CDM particles (Aronson and Hansen 1972; Padmanabhan 1990). The analogy with a softened gravitational potential implies $\rho_{\rm m} \sim m\epsilon^{-3}$, although it is clear from the outset that this analogy is inexact; the hard-core, van der Waals potential effectively

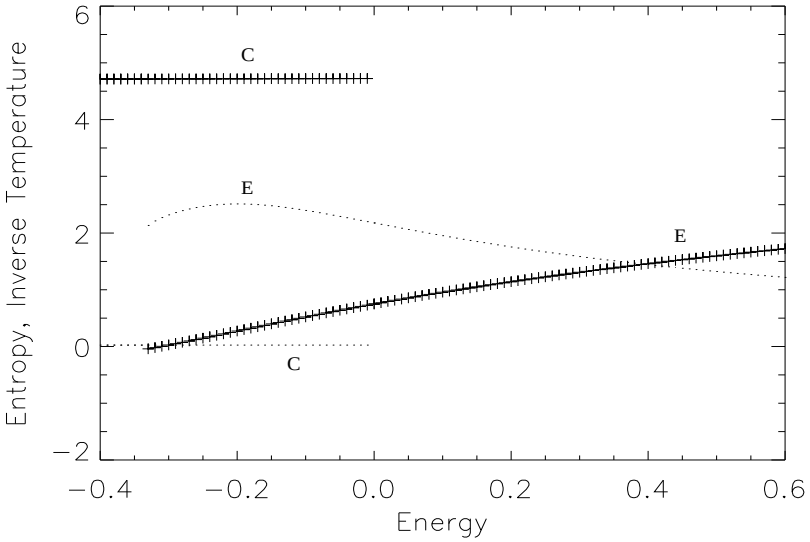

Figure 6.4: Dimensionless entropy (thick curve) and inverse temperature (thin) versus energy. The collapsed and extended phases are labelled C and E respectively. Both quantities display discontinuous jumps at the phase transitions at $\xi_c \simeq -0.335$ and $\xi_c^{(+)} \simeq 0.0$. If the energy is increased from below ξ_c, the system remains in the collapsed phase until $\xi = \xi_c^{(+)}$, when it jumps to the extended phase. If the energy is reduced from above $\xi_c^{(+)}$, the system remains in the extended phase until $\xi = \xi_c$ when it jumps to the collapsed phase.

excludes a volume $\sim \epsilon^3$ around each particle, whereas softened gravity suppresses the mutual acceleration of particles separated by a distance ϵ without preventing them from 'coasting' even closer together. The solutions of (6.7)–(6.9) are compared with the van der Waals model by integrating the nonideal Lane-Emden equation

$$\frac{1}{r^2}\frac{d}{dr}\left[\frac{r^2}{\rho}\frac{d}{dr}\left(\frac{\rho T}{1-\rho/\rho_{\rm m}}\right)\right] = -4\pi G\rho \tag{6.11}$$

from $r = R_1$ to $r = R$, obtaining

$$\frac{1}{\rho(R)}\left.\frac{d\rho}{dr}\right|_R - \frac{R_1^2}{R^2\rho(R_1)[1-\rho(R_1)/\rho_{\rm m}]^2}\left.\frac{d\rho}{dr}\right|_{R_1} = -\beta M_1/M \ , \tag{6.12}$$

where M_1 denotes the mass enclosed in the volume $R_1 \leq r \leq R$. [$\rho(R) \ll \rho_{\rm m}$ is used to simplify (6.12).] The quantities $\rho(R)$, $\rho(R_1)$, their derivatives, M_1, and β can be extracted from our numerically computed profiles, which satisfy (6.7)–(6.9), in order to find $\rho_{\rm m}$ as a function of ξ and ϵ and hence compare with the results of Aronson and Hansen (1972) and Padmanabhan (1990). The inner integration limit R_1 must be positioned carefully near the inflection point of the central Dirac peak, e.g. at $r = 10^{-3.8}$ in Figure 6.3, in order to avoid the innermost grid cells, where the numerical solution is noisiest, while ensuring that $\rho(R_1)/\rho_{\rm m}$ is not too small, to avoid roundoff error when solving (6.12) for $\rho_{\rm m}$.

In Figure 6.5, the density of states is compared with the van der Waals models by plotting $1/\beta$ versus ξ for both models in the MCE. The open triangles indicate solutions of (6.11) for $10^{-4} \leq a = M/4\pi\rho_{\rm m}R^3 \leq 10^{-2}$. The boxes and asterisks indicate solutions of (6.7)–(6.9) for $\epsilon = 10^{-4}$ and 10^{-3} respectively, with a tolerance of $\delta = 10^{-8}$. (it has been verified that the results are unchanged for $10^{-6} \leq \delta \leq 10^{-8}$.) Applying the procedure in the previous paragraph to compute $\rho_{\rm m}$, $\log a = -10.1$ and -9.00 is found for the boxes and asterisks respectively. For $\xi > \xi_c$, the two models are in accord, as expected; the halo is extended, so the softening (and the precise value of a) are not important in the dilute regime $\rho \ll \rho_{\rm m}$. For $\xi < \xi_c$, the two models differ appreciably. The density of states calculation predicts less variation of T with E than the van der Waals model, for a given value of a. The trend is confirmed, apparent in Figure 4.11 of Padmanabhan (1990), that T increases with $|a|$ when $\xi < \xi_c$ is fixed. However, the trend is confirmed in the range $-10 \lesssim \log a \lesssim -9$, which does not overlap with the range $-4 \leq \log a \leq -2$ investigated by Padmanabhan (1990). The effective value of $\rho_{\rm m}$ predicted by the density of states calculation is systematically greater than anticipated in van der Waals models published previously.

6.3.4 Phase diagram on $\xi - \epsilon$ plane

A phase diagram for the system can be produced by plotting the power-law exponent of the density profile as a function of ξ and ϵ. The logarithmic slope of the density profile is defined as

$$p(x) = \frac{d\ln[\rho(x)]}{d\ln x}. \tag{6.13}$$

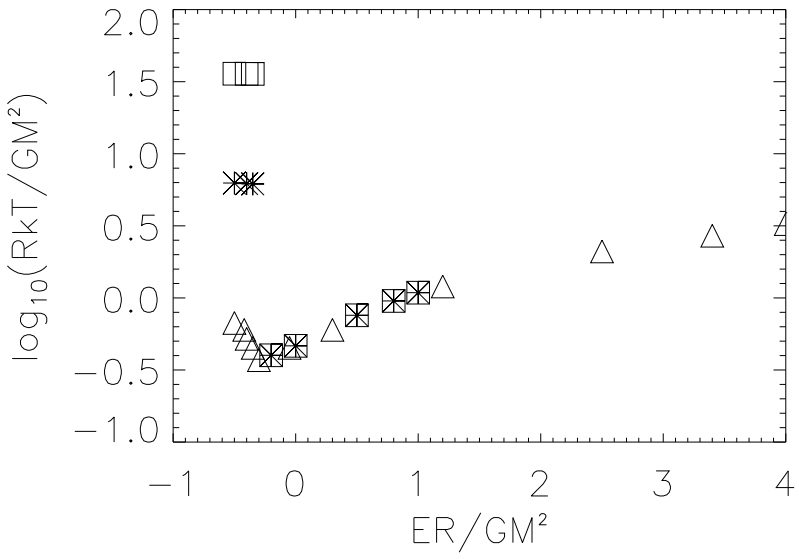

Figure 6.5: Temperature T as a function of total mechanical energy E for a range of softening lengths ϵ. The open squares and asterisks denote CDM halos with $\epsilon = 10^{-4}$ and 10^{-3} respectively, modelled by the density of states formalism (6.7)–(6.9). These halos correspond to $\log a = -10.1$ and -9.00 in the van der Waals formalism. The open triangles denote CDM halos with $-4 \leq \log a \leq -2$, modelled by the van der Waals formalism (Padmanabhan 1990). For any given E in the plotted range, T is the same for all values $-4 \leq \log a \leq -2$; moreover, these a values are systematically greater than the predictions of the density of states formalism.

The logarithmic slope is evaluated in the inner halo at $x = \epsilon$, and also at the box edge, $x = 1$, to consistently characterise the two phases. Figures 6.6 and 6.7 display these phase diagrams for σ=0.01 (note that varying the value of σ does not affect the results noticeably). The phase transition occurs where the contours are bunched at $\xi \simeq -0.335$. For $\epsilon \lesssim 10^{-2}$, $p(\epsilon)$ is large (Dirac cusp) and $p(1)$ is almost zero (flat envelope) in the collapsed phase. For $\epsilon \gtrsim 10^{-2}$, the system does not undergo a phase transition. The entropy and temperature are continuous for all ξ and the profile is extended.

Interestingly, the central Dirac peak steepens as ϵ decreases, in the collapsed phase. Figure 6.8 plots $p(x)$ as a function of logarithmic radius for $10^{-5} \leq \epsilon \leq 10^{-2}$ and at a fixed energy $\xi = -0.5$. The location and amplitude of the maximum of $p(x)$ is a strong function of ϵ, with $p(x) \to 0$

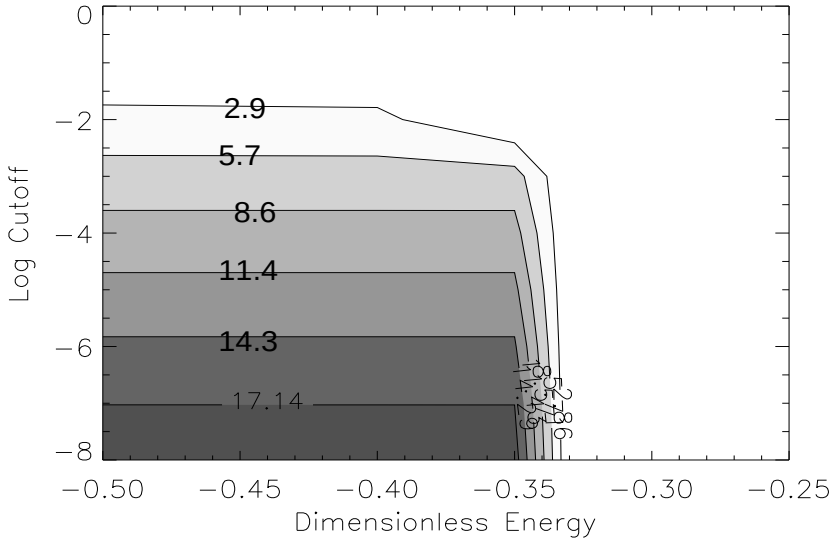

Figure 6.6: Contour plot of the logarithmic slope , $|p|$, of the density profile in its inner, $x = \epsilon$, region, as a function of energy, ξ. The phase transition is clear at $\xi \sim -0.335$ for $\epsilon \lesssim 10^{-2}$. The slope, $|p(\epsilon)|$ steepens as ϵ is reduced. For $\epsilon \gtrsim 10^{-2}$ the system no longer collapses. The outer profile is flat in the collapsed regime.

as $x \rightarrow 0, 1$ for collapsed halos. The classical NFW profile (Navarro et al. 1996) and the profile of the extended phase at $\xi > \xi_c$ are also plotted for comparison. Clearly the NFW profile does not resemble either the collapsed or extended phase profiles. We are unable to explain unambiguously why the NFW profile is not reproduced, but remind the reader that our analysis neglects several effects, such as hierarchical clustering, non-zero angular momentum, and cosmological expansion, which are present in full N-body simulations. Hence, there is no reason to expect agreement since we are highlighting potential flaws, although necessary, in the design of the simulations, and not comparing the subsequent output.

The dynamic range of numerical studies generally extends from a few times ϵ to the virial radius. In this range, from Figure 6.8, $p(x)$ is strongly affected by the softening length used.

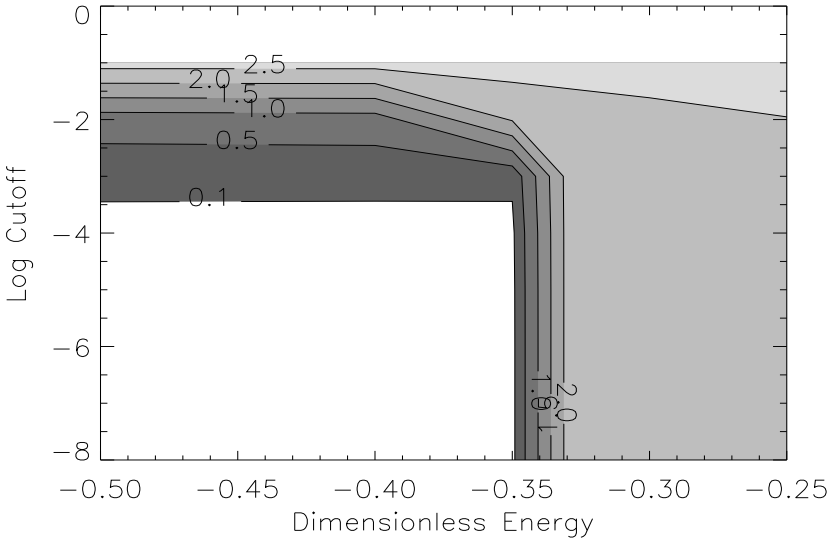

Figure 6.7: Contour plot of the logarithmic slope , $|p|$, of the density profile in its outer, $x = 1$ (b), region, as a function of energy, ξ. The phase transition is clear at $\xi \sim -0.335$ for $\epsilon \lesssim 10^{-2}$. The slope, $|p(\epsilon)|$ steepens as ϵ is reduced. For $\epsilon \gtrsim 10^{-2}$ the system no longer collapses. The outer profile is flat in the collapsed regime.

6.3.5 Cosmological expansion

The calculations are performed in a static background spacetime. In the central parts of the halo, where most of the attention is focussed, CDM particles are tightly bound and effectively decoupled from the cosmological expansion. Consequently, the phase transition at ξ_c is essentially unaffected, as long as the central volume where the cosmological expansion can be neglected is still large enough to encompass the 'core-halo' structure (centre-to-edge density contrast $\gtrsim 709$) required for the gravothermal catastrophe to occur (Lynden-Bell and Wood 1968). From this perspective, a static background metric is a good approximation.

In the outer halo, CDM particles are loosely bound and $\rho(x)$ may be determined partly by the expansion and certain specific cosmological parameters. For example, there exists a mapping between the linear and evolved two-point correlation functions of halos which implies power-law density profiles with exponent $-3(n+4)/(n+5)$, where n is the index of the power spectrum of initial fluctuations (Hamilton et al. 1991; Padman-

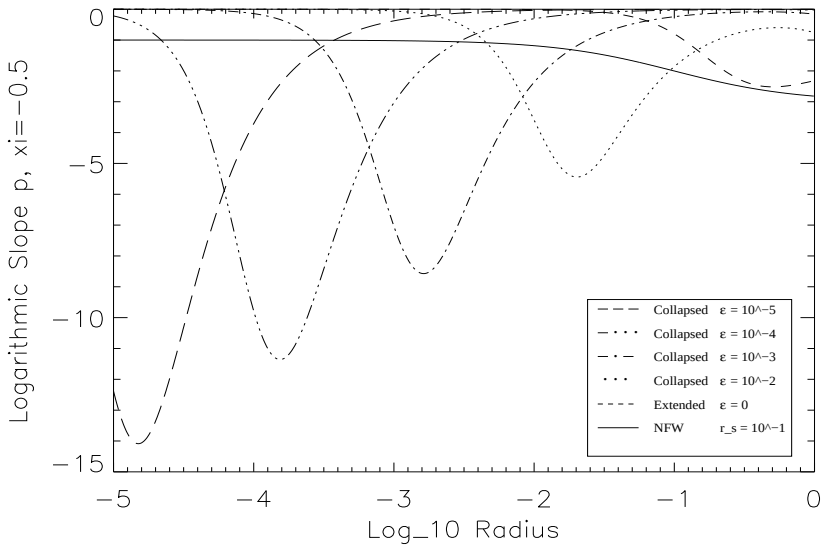

Figure 6.8: Logarithmic slope, p as a function of logarithmic radius for $\xi = -0.5$ and $\epsilon = 10^{-5}$ (long dash), 10^{-4} (dash-dot-dot-dot), 10^{-3} (dash-dot) and 10^{-2} (dotted). The slope is a maximum of x slightly above ϵ. Also plotted is an NFW profile (solid) and an extended phase profile (short dash, $\xi = -0.3$).

abhan and Engineer 1998). By the same token, simulations suggest that the dependence of the shape of the profile on initial cosmological parameters is weak; this empirical result holds for SCDM ($\Omega_M = 1.0$), LCDM ($\Omega_M = 0.3, \Omega_\Lambda = 0.7$) and open ($\Omega_M = 0.3$) cosmogonies, as well as a wide mixture of hot and cold dark matter components (Huss et al. 1999b). Note that the origin of the NFW scale radius observed in simulated halos, r_s, is not explained by the (self-similar) Padmanabhan and Engineer (1998) mapping. However, the total power spectrum, $P(k)$, is proportional to the product of the Fourier transformed halo profile and the power spectrum of the distribution of halo centres, $P_{\rm cent}(k)$ (Padmanabhan 2002), implying $\rho(x) \propto x^{-1}$ at large k [deep minima of the gravitational potential, V, with $P_{\rm cent}(k) \propto P_V(k)$], and $\rho(x) \propto x^{-3}$ at small k [quasi-linear regime, $P_{\rm cent}(k) \propto P(k)$] (Padmanabhan 2002).

Huss et al. (1999a) demonstrated empirically that cosmological expansion does influence $\rho(x)$, but that it is one of several relevant factors. They simulated a halo with all tangential components of the gravitational force

artificially set to zero, reproducing the spherical infall solution with a power-law exponent of ~ -2.2 and no break in slope (Bertschinger 1985). They also showed that r_s is not determined solely by expansion, found evidence for the importance of angular momentum in the system, and concluded that the unbroken power-law profiles of van Albada (1982) in the absence of expansion were inadequately resolved for the purpose of testing the existence of r_s. Of course, the scale radius (and hence the concentration parameter) of a halo does depend critically on its formation epoch: r_s is fixed by the overdensity, δ_c, which is, in turn, a function of the collapse redshift (Navarro et al. 1997).

6.4 Comparison with the design of numerical simulations of CDM halos

The key result from Section 6.3 from the perspective of N-body simulations is that any simulation with $\epsilon \neq 0$ can produce stable halos for energies $\xi < \xi_c$ that do not support stable halos in true ($\epsilon = 0$) gravity. Furthermore, these stable $\epsilon \neq 0$ halos are collapsed, whereas stable $\epsilon = 0$ halos are extended. In this section it is shown that many published N-body results inadvertently sample the collapsed regime only. We confine this work to studies that report the specific values of ξ and ϵ explored.

6.4.1 Softening length

Simulations have been performed over a range of N and with a range of resolutions in an attempt to place bounds on the optimum softening length (Ghigna et al. 2000; Splinter et al. 1998; Moore et al. 1998). van Kampen (2000) argued that the choice $\epsilon \approx 0.5 r_{1/2} N^{-1/3}$, where $r_{1/2}$ is the half-mass radius of the system, strikes a balance between too short a relaxation time (ϵ too small) and excessive particle clustering (ϵ too large). Similarly, Athanassoula et al. (2000) find an optimal length $\epsilon = 0.32 N^{-0.27}$ for a $\gamma = 0$ Dehnen sphere. These different criteria define a range of ϵ within which most modern simulations are performed. The softening length in high resolution simulations is 1–5kpc for galaxy-sized halos (Reed et al. 2003), corresponding to $\epsilon \sim 10^{-4}$ if R is taken to be the virial radius. The studies investigated below occupy the range $10^{-4} < \epsilon < 10^{-2}$.

6.4.2 Total energy of a halo

The total energy of a simulated halo is rarely quoted in published studies. We therefore calculate ξ from the quoted mass, size and concentration parameter, $c = r_s/r_{200}$, where r_s is the characteristic radius of the halo and $r_{200} = R$ is the radius at which the halo density has dropped to 200 times the background. For a classical NFW halo, the kinetic energy, K, is given by (Mo et al. 1998),

$$K_{NFW} = \frac{GM^2}{2R} f(c_{NFW}), \tag{6.14}$$

$$f(c_{NFW}) = \frac{c}{2} \frac{1 - 1/(1+c)^2 - 2\ln(1+c)/(1+c)}{[c/(1+c) - \ln(1+c)]^2}, \tag{6.15}$$

assuming circular orbits. The potential energy is (Binney and Tremaine 1987,Eqn 2P-1)

$$U_{NFW} = -\frac{G}{2} h(c), \tag{6.16}$$

$$h(c) = \int_0^1 x^{-2} [(1+cx)^{-1} - 1 + \ln(1+cx)]^2 \, dx, \tag{6.17}$$

assuming spherical symmetry.

Similarly, the energy of the halo profile found by Moore et al. (1999b) can be calculated, and is found to be,

$$K_M = \frac{GM^2}{4R} \left[1 + \frac{f(c_M)}{\ln^2(1 + c^{3/2})} \right], \tag{6.18}$$

$$f(c_M) = \int_0^1 \frac{\ln^2(1 + c_M^{3/2} x^{3/2})}{x^2} \, dx, \tag{6.19}$$

$$U_M = -\frac{GM^2}{2R} \frac{f(c_M)}{\ln^2(1 + c^{3/2})} \tag{6.20}$$

Due to the assumptions inherent in the calculation of both K and U, the total energy, E, is calculated in three ways: $E^{(a)} = -K$, $E^{(b)} = U/2$ and $E^{(c)} = K + U$. The first two methods utilise the virial theorem. The dimensionless energy, ξ, is calculated using $\xi = ER/GM^2$. Of the assumptions made, that of circular orbits is the most questionable. $\xi^{(b)}$ is therefore taken to be the most reliable measure of the energy, as the assumption of

Study	M ($10^{12} M_\odot$)	r_{200} (kpc)	c	$\xi^{(a)}$	$\xi^{(b)}$	$\xi^{(c)}$	ϵ	Comment	Reference
NFW	2.9	172	17.54	-0.76	-0.52	-0.28	0.01		1
	22.7	733	15.38	-0.73	-0.48	-0.23	0.01		1
Huss	500	1360	6.3	-0.55	-0.29	-0.03	0.0037	CDM run	2
Moore	430	1950	4	-0.57	-0.32	-0.07	0.0005	cluster	3
Reed	0.188	119	28	-0.93	-0.68	-0.43	0.0020	dwf1	4
	40	705	12.5	-0.68	-0.43	-0.18	0.0009	grp1	4
Hayashi	2.2	212.7	5.3	-0.52	-0.27	-0.02	0.0021	$G3/256^3$	5

Table 6.2: Recent N-body simulations of CDM halos. The mass M, size r_{200}, concentration parameter, c, and softening length, ϵ, are measured from the output. Equations (6.14)–(6.20) are used to calculate the halo energy in three ways, $\xi^{(a)}$, $\xi^{(b)}$ and $\xi^{(c)}$. All calculations assume an NFW profile, except for Moore et al. (1999b) which uses the Moore profile. (1) Navarro et al. (1996); (2) Huss et al. (1999a); (3) Moore et al. (1999b); (4) Reed et al. (2003); (5) Hayashi et al. (2003)

spherical symmetry is not unreasonable.

6.4.3 Position on the phase diagram

Using these expressions, one can take recent N-body studies in order to determine where simulations lie on the phase diagram. This can be performed for a range of halo masses: from dwarf galaxy ($\sim 10^{10} M_\odot$) to cluster size ($\sim 10^{14} M_\odot$). Results have been chosen from several recent and seminal works that have performed N-body simulations of dark matter halos in a ΛCDM cosmogony. From the output parameters including c, ξ and ϵ (normalised by r_{200}) are calculated. Table 6.2 summarises the critical information. In the final column, comments are made identifying the specific halos chosen from the studies. The three methods for calculating the energy produce very different results.

In Figure 6.9, the most reliable energies, $\xi^{(b)}$, and softening values for these studies are placed over the phase diagram of Figure 6.6(a). Studies lie either exclusively in the collapsed phase regime, or in the bistable region, where stable solutions exist for both collapsed and extended phases.

The two energy calculation methods produce different constraints on the range of concentration parameters producing halos lying in either the collapsed or extended phases. Any NFW profile with the energy calculated via K must lie in the collapsed regime. Energies calculated via U, however, can exist in the extended phase if $c_{NFW} \lesssim 8$, which correspond to more massive halos. Similarly, the Moore calculation shows empirically $\xi_M^{(a)} < -3/8$ for all $c > 0$ and is therefore in the collapsed regime exclusively. When

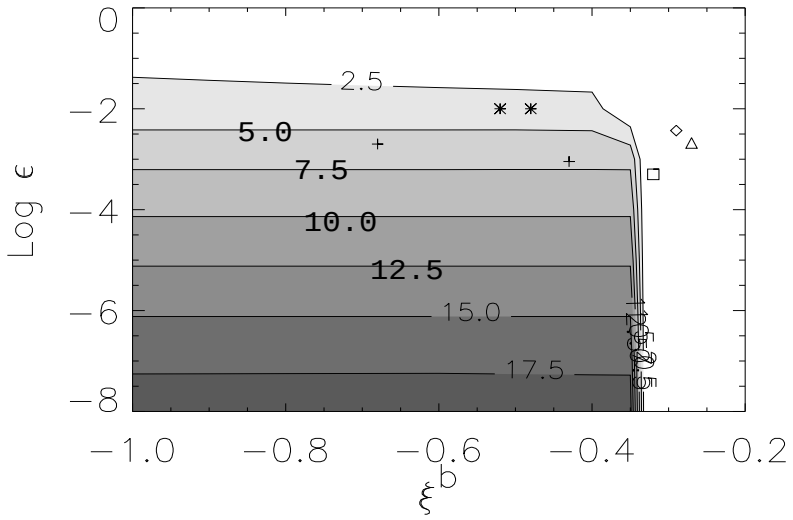

Figure 6.9: Energy, $\xi^{(b)}$, and ϵ of published N-body CDM halos overlaid on a contour plot of $p(\epsilon)$, as summarised in Table 6.2. The asterisks, plus signs, triangle, box and diamond denote the results of Navarro et al. (1996), Reed et al. (2003), Hayashi et al. (2003), Moore et al. (1999b) and Huss et al. (1999a) respectively.

calculated using the potential energy, $c_M \lesssim 4$ for the possibility of extended halos. Hence, if calculated via the kinetic energy, both profiles always have $\xi^{(a)} < \xi_c$ and lie in the collapsed regime exclusively. Calculated the alternative way, small concentration parameters allow the halos to be in either phase (bistable energy region) depending on the calculation history.

Without the assumption of virialisation, the energies calculated via $E = K + U$ are, in general, less negative. However, similar to the other methods, all energies, $\xi^{(c)}$, lie in either the collapsed or the bistable regions. Many studies lie in the collapsed regime exclusively.

6.5 Conclusions

The equilibrium configurations of N self-gravitating collisionless particles, interacting via a softened gravitational potential, in the MCE and mean-field limit have been investigated. Below a critical energy, $\xi_c \simeq -0.335$, a system with $\epsilon \neq 0$ exists in a stable, collapsed phase. This phase is

unstable for pure gravity ($\epsilon = 0$). Above another critical energy $\xi_c^{(+)} \simeq 0$, both softened and unsoftened systems exist in an stable, extended phase. In the intermediate region $\xi_c < \xi < \xi_c^{(+)}$, both the collapsed and extended phases are accessible; the detailed route to equilibrium determines which one is picked out. The density profiles for the extended and collapsed phases are qualitatively different. The extended profile has a flat core and near-isothermal outer envelope. The collapsed profile is a centrally condensed Dirac peak, whose logarithmic slope depends on ϵ.

The results are compared with the construction of published N-body simulations by using the softening parameter, ϵ, size, r_{200}, and concentration parameter, c, to place simulated halos on the ξ-ϵ phase diagram. It is found that many published simulations inadvertently sample the collapsed phase only, even though this phase is unstable for pure gravity and arguably irrelevant astrophysically.

The reader is reminded that several effects are neglected that are important in real CDM halos, such as hierarchical clustering, nonzero angular momentum, and cosmological expansion. In addition, real halos are not fully relaxed. The results elucidate some of the artificial behaviour that a softened potential can introduce; they are not a substitute for a full N-body calculation. We do not intend to compare profiles with those produced by simulations, but merely highlight that the design of simulations, although necessary, may be flawed.

CHAPTER 7

Summary and Conclusions

Dark matter is an enigmatic substance that comprises 85–90 per cent of the mass of universe. Despite its importance for understanding the formation of structure, it is undetected and poorly understood. This thesis aimed to shed light on the structure of dark matter in galaxies, where it can be studied via its gravitational influence on baryons and photons.

7.1 Mass distribution of 2237+0305

The gravitational lensing galaxy 2237+0305 is an excellent laboratory for studying the structure of its dark matter halo since there is a range of complementary, high-quality data available describing its major mass components. In this work, a combination of lensing, photometric and kinematic data was used to constrain the mass distribution in the major mass components of 2237+0305 — the bulge, disk, dark matter halo and bar. Given that it is a complicated late-type galaxy, further kinematic information was required in the lensed image region to break the remaining degeneracies between models for the dark matter halo.

High resolution Keck echelle data were used to measure the inner rotation curve and velocity dispersion profile along the galactic major and minor axes. The Nad absorption line was used as the kinematic tracer since it does not appear to be contaminated by other spectral features. Neither the Mgb or FeI lines produced consistent results, most likely due to contamination from the quasar and other galactic absorption features in their echelle order. No emission lines were observed in the galaxy spectrum.

Addition of this information provided a much improved model for the galaxy, with early results suggesting a softened spherical density distribution similar to that found by Bertschinger (1985) for secondary infall onto a spherical perturbation is preferred for the dark matter halo. All solutions favoured models with submaximal disks ($v_{\rm disk}/v_{\rm total} \sim 50\%$). No statistically acceptable solutions were found due to the simple kinematic model used for the bulge and dark matter components, however the best-fitting solutions were found to have reduced $\chi^2 \sim 2$–5. The inclusion of bar orbits and a more robust estimate of the contribution of the dark matter to the kinematics would tighten the result.

The confirmation of a softened density profile for the dark matter halo with further modelling will add to observational evidence suggesting the results from N-body simulations are not reproducing the true structure of halos (de Blok et al. 2001b). Either the baryons play an important role in the softening of the centres of dark matter halos, there is a problem with the simulations (Trott and Melatos 2005), or a problem with the observations (Swaters et al. 2003). The addition of kinematic data in this galaxy removes some of the necessary dependence on parametric models because the slope

is constrained over a radius range greater than that probed by the point images of the quasar, and more parameters can be modelled with the extra degrees of freedom. The galaxy 2237+0305 remains the best modelled galaxy displaying quasar lensing.

7.2 Detecting substructure in the Galaxy

The dark matter distribution within our own Galaxy can be probed by observation of its gravitational effect on baryonic structures. The interaction of dark matter subhalos with disk stars as the subhalo passes through the Galactic disk was modelled, to search for and quantify observable stellar phase-space signatures.

The subhalos were modelled with mass, size and density distributions consistent with those from semi-analytic models of substructures within Milky Way-like galaxies. Simulations were performed of the gravitational influence of a subhalo passing through the disk of our Galaxy on the phase-space positions of disk stars. The next generation satellite GAIA and its predicted uncertainties in measured parameters was used to determine if it could detect the signatures of subhalos in phase space. Estimates from the literature were also obtained for the magnitude of other phase space effects in the disk that could mimic a subhalo passage, such as heating of stars by molecular clouds and stellar clumping due to spiral arms and star formation regions.

In both the spatial and velocity domains, only very massive subhalos ($M \gtrsim 10^9 M_\odot$) were found to be detectable given the poor distance determinations for stars beyond a few kiloparsecs from the sun and due to the lack of observable stars at large distance. The predictions for the mass function of dark matter substructure require the threshold mass to be lower than $\sim 2\times10^8 M_\odot$ for there to be at least one subhalo in the disk at all times. GAIA will not therefore have sufficient resolution in key parameters (such as distance determination), or adequate sensitivity, to detect the passage of a dark matter subhalo through the disk unless a massive ($M \gtrsim 10^9 M_\odot$) subhalo lies fortuitously in the disk now ($P \lesssim 10\%$).

7.3 Properties of collisionless N-body systems in softened potentials

The structure of a self-gravitating system of collisionless particles was investigated using a statistical mechanical framework to compare results with those found by N-body simulations of collisionless dark matter particles. In particular, the effect of softening the gravitational potential at short distance, ϵ, on the density distribution in the system was investigated. As found in previous work, the system is able to exist in a stable phase at lower energies ($\xi_c < -0.335$) in a softened system than in a system with pure $1/r$ gravity. The introduction of a softening parameter allows a phase transition to a low temperature stable phase where most of the particles reside in the system's centre. Without the softening, the system is unstable at these low energies and no solution can be found. For $\xi > \xi_c$ the pure gravity solution ($\epsilon = 0$) exhibits a density profile that has a flat core ($\rho \sim r^0$) and outer logarithmic slope consistent with earlier results for secondary infall onto a spherical perturbation ($\rho \sim r^{-2.2}$, Bertschinger 1985).

The energies of halos from N-body simulations performed by other groups and presented in the literature were compared with the energy ranges for the stable and unstable phases, and found that many simulations may be probing an energy regime only physically allowable because a softening is used in their computation. The lack of published values for the final energies of these simulations required their calculation to be performed using different standard methods and other known parameters (e.g. system size and mass). Further work will calculate the energy of these simulated halos directly by summing over individual particle energies and comparing the results with the theory presented here. If the introduction of a softening length does allow the N-body systems to enter an unphysical phase, simulations are producing density profiles that do not represent nature, and may prove to be the resolution of the cusp-core controversy.

The results were performed in a box with a static background and no angular momentum. A calculation that could be compared directly with the results from N-body simulations would need to include both cosmological expansion and angular momentum as these affect the shape of the final density profile (Huss et al. 1999a).

Future work could employ the framework of de Vega and Siebert (2002)

who construct, using a similar argument to that presented here, the equilibrium density profiles for two collisionless particle populations with different mass. Although their relative masses are 50–60 orders of magnitude apart, the equilibrium configuration of dark matter particles residing with stars would be an interesting calculation.

7.4 Conclusions

The eventual discovery and understanding of the properties, distribution and formation of dark matter remains one of astrophysics' holy grails. With the amount of effort being placed in determining its distribution in the universe, and the more recent effort to detect it directly (e.g. the DAMA experiment, Belli et al. 1999) and indirectly (self-annihilation radiation from the Galactic centre, e.g. Boehm et al. 2004), this feat should be achieved in the decades to come.

Galaxies are the best understood systems that contain dark matter concentrations, and the bulk of future work should be concentrated on them. Lens systems, such as 2237+0305, offer the best hope in this regard due to the larger amount information available about them. Among lens systems, such good laboratories are rare however, since most systems are early-type galaxies at significant redshift. There are a handful of other excellent candidate lenses for a similar study (e.g. B1600+434, a z= 0.41 late-type lens), but most suffer from confusion, such as from nearby perturbers. We are still discovering new lenses with new properties not yet observed in known systems (e.g. wide angle lenses with image separations >10 arcsec, SDSS J1004+4112, Inada and Oguri 2004), and the larger number, the greater diversity and the continual improvement of techniques to study them, will build-up a more comprehensive picture of the distribution of dark matter in galaxies than one can obtain from a single nearby system. In addition, the work on systems with extended images is reaching a point where it can make a huge contribution to our understanding, due to the greater amount of information available. Until recently, the complex algorithms required to adequately model these systems has not been available.

The resolution of the 'cusp-core' controversy will most likely lie in the full use of baryonic physics in simulations of galaxy formation. Many of the assumptions used in the calculations producing the angular momentum

problem (e.g. that the angular momentum distributions of the dark matter and the baryons are the same) will likely be shown to be flawed through a proper simulation, and the 'cusp-core' controversy may also be borne out in this manner. The recent work of Hayashi et al. (2004a) comparing galaxy kinematics directly with the output of simulations is also a step in the right direction. One also must be careful to not compare the shape of dark matter halos in regions that do not converge in the simulations.

Nonetheless, observationalists have been very careful to use high quality data when making assertions about the shape of the dark matter halo, and the results of Chapter 6 should serve as a general warning about the applicability of the simulations altogether. Greater transparency in the design and output of N-body simulations (e.g. kinetic and potential energies of the halo) would help the rest of the community to better appreciate and understand them, and remove some of the mystique between the observational and simulation communities, thereby furthering the field and contributing to our understanding of the universe in which we live.

Bibliography

E. Agol, B. Jones, and O. Blaes. Keck Mid-Infrared Imaging of QSO 2237+0305. *ApJ*, 545:657–663, December 2000.

V. A. Antonov. Unknown. *Vest. Leningrad Univ.*, 7:135, 1962.

E. B. Aronson and C. J. Hansen. Thermal Equilibrium States of a Classical System with Gravitation. *ApJ*, 177:145–+, October 1972.

E. Athanassoula. Bars and the connection between dark and visible matter. In *IAU Symposium 225*, pages 255–+, July 2004.

E. Athanassoula, E. Fady, J. C. Lambert, and A. Bosma. Optimal softening for force calculations in collisionless N-body simulations. *MNRAS*, 314: 475–488, May 2000.

D. G. Barnes, R. L. Webster, R. W. Schmidt, and A. Hughes. Imaging HI in the lensing galaxy 2237+0305. *MNRAS*, 309:641–650, November 1999.

J. E. Barnes and L. Hernquist. Dynamics of interacting galaxies. *Ann. Rev. Astron. & Astrophys.*, 30:705–742, 1992.

P. Belli, R. Bernabei, C. J. Dai, W. di Nicolantonio, L. K. Ding, G. Ignesti, A. Incicchitti, H. H. Kuang, J. M. Ma, F. Montecchia, and D. Prosperi. Direct Search for Dark Matter Particles Deep Underground. In *AIP Conf. Proc. 476: 3K cosmology*, pages 65–+, 1999.

C. L. Bennett, M. Halpern, G. Hinshaw, N. Jarosik, A. Kogut, M. Limon, S. S. Meyer, L. Page, D. N. Spergel, G. S. Tucker, E. Wollack, E. L. Wright, C. Barnes, M. R. Greason, R. S. Hill, E. Komatsu, M. R. Nolta, N. Odegard, H. V. Peiris, L. Verde, and J. L. Weiland. First-Year Wilkinson Microwave Anisotropy Probe (WMAP) Observations: Preliminary Maps and Basic Results. *ApJS*, 148:1–27, September 2003.

A. J. Benson, C. G. Lacey, C. M. Baugh, S. Cole, and C. S. Frenk. The effects of photoionization on galaxy formation - I. Model and results at z=0. *MNRAS*, 333:156–176, June 2002.

A. J. Benson, C. G. Lacey, C. S. Frenk, C. M. Baugh, and S. Cole. Heating of galactic discs by infalling satellites. *MNRAS*, 351:1215–1236, July 2004.

G. Bertin, L. Ciotti, and M. Del Principe. Weak homology of elliptical galaxies. *Astron. & Astrophys.*, 386:149–168, April 2002.

E. Bertschinger. Self-similar secondary infall and accretion in an Einstein-de Sitter universe. *ApJS*, 58:39–65, may 1985.

M. S. Bessell. UBVRI passbands. *PASP*, 102:1181–1199, October 1990.

J. Binney. On the rotation of elliptical galaxies. *MNRAS*, 183:501–514, May 1978.

J. Binney and S. Tremaine. *Galactic Dynamics*. Princeton, NJ, Princeton University Press, 1987.

G. R. Blumenthal, S. M. Faber, R. Flores, and J. R. Primack. Contraction of dark matter galactic halos due to baryonic infall. *ApJ*, 301:27–34, February 1986.

C. Boehm, D. Hooper, J. Silk, M. Casse, and J. Paul. MeV Dark Matter: Has It Been Detected? *Physical Review Letters*, 92(10):101301–+, March 2004.

S. Boissier and N. Prantzos. Chemo-spectrophotometric evolution of spiral galaxies - II. Main properties of present-day disc galaxies. *MNRAS*, 312: 398–416, February 2000.

A. D. Bolatto, J. D. Simon, A. Leroy, and L. Blitz. The Density Profile of the Dark Matter Halo of NGC 4605. *ApJ*, 565:238–243, January 2002.

R. Bottema. The Stellar Kinematics of Galactic Disks. *Astron. & Astrophys.*, 275:16–+, August 1993.

R. Bottema. The maximum rotation of a galactic disc. *Astron. & Astrophys.*, 328:517–525, December 1997.

J. S. Bullock, A. V. Kravtsov, and D. H. Weinberg. Reionization and the Abundance of Galactic Satellites. *ApJ*, 539:517–521, August 2000.

C. M. Carollo, M. Stiavelli, P. T. de Zeeuw, M. Seigar, and H. Dejonghe. Hubble Space Telescope Optical-Near-Infrared Colors of Nearby $R^{1/4}$ and Exponential Bulges. *ApJ*, 546:216–222, January 2001.

B. W. Carroll and D. A. Ostlie. *An introduction to modern astrophysics.* Reading, MA: Addison-Wesley, —c1996, 1996.

M.-L. Chabanol, F. Corson, and Y. Pomeau. Statistical mechanics of point particles with a gravitational interaction. *Europhysics Letters*, 50:148–154, apr 2000.

S. Chandrasekhar. Dynamical Friction. I. General Considerations: the Coefficient of Dynamical Friction. *ApJ*, 97:255–+, March 1943.

G. Chartas, V. Gupta, G. Garmire, C. Jones, E. E. Falco, I. I. Shapiro, and F. Tavecchio. Constraining H_0 from Chandra Observations of Q0957+561. *ApJ*, 565:96–104, January 2002.

E. Chereul, M. Crézé, and O. Bienaymé. The distribution of nearby stars in phase space mapped by Hipparcos. Clustering and streaming among A-F type stars. *Astron. & Astrophys. Suppl. Ser.*, 135:5–28, February 1999.

S. Cole, C. G. Lacey, C. M. Baugh, and C. S. Frenk. Hierarchical galaxy formation. *MNRAS*, 319:168–204, November 2000.

S. Courteau and H. Rix. Maximal Disks and the Tully-Fisher Relation. *ApJ*, 513:561–571, March 1999.

A. N. Cox. *Allen's astrophysical quantities.* Allen's astrophysical quantities, 4th ed. Publisher: New York: AIP Press; Springer, 2000. Editedy by Arthur N. Cox. ISBN: 0387987460, 2000.

P. Crane, R. Albrecht, C. Barbieri, J. C. Blades, A. Bokensenberg, J. M. Deharveng, M. J. Disney, P. Jakobsen, T. M. Kamperman, I. R. King, F. Macchetto, C. D. Mackay, F. Paresce, G. Weigelt, D. Baxter, P. Greenfield, R. Jedrzejewski, A. Nota, and W. B. Sparks. First results from the Faint Object Camera - Images of the gravitational lens system G2237 + 0305. *ApJL*, 369:L59–L61, March 1991.

M. Davis, G. Efstathiou, C. S. Frenk, and S. D. M. White. The evolution of large-scale structure in a universe dominated by cold dark matter. *ApJ*, 292:371–394, may 1985.

W. J. G. de Blok, S. S. McGaugh, A. Bosma, and V. C. Rubin. Mass Density Profiles of Low Surface Brightness Galaxies. *ApJL*, 552:L23–L26, May 2001a.

W. J. G. de Blok, S. S. McGaugh, and V. C. Rubin. High-Resolution Rotation Curves of Low Surface Brightness Galaxies. II. Mass Models. *AJ*, 122:2396–2427, nov 2001b.

R. de Grijs and R. F. Peletier. The shape of galaxy disks: how the scale height increases with galactocentric distance. *Astron. & Astrophys.*, 320: L21–L24, April 1997.

G. de Vaucouleurs. Recherches sur les Nebuleuses Extragalactiques. *Annales d'Astrophysique*, 11:247–+, January 1948.

G. de Vaucouleurs. General Physical Properties of External Galaxies. *Handbuch der Physik*, 53:311–+, 1959.

H. J. de Vega and N. Sánchez. Statistical mechanics of the self-gravitating gas: I. Thermodynamic limit and phase diagrams. *Nuclear Physics B*, 625:409–459, mar 2002.

H. J. de Vega and J. A. Siebert. Statistical mechanics of the self-gravitating gas with two or more kinds of particles. *Phys. Rev. E*, 66(1):016112–+, July 2002.

W. Dehnen and J. Binney. Mass models of the Milky Way. *MNRAS*, 294: 429–+, March 1998.

J. Dubinski. The effect of dissipation on the shapes of dark halos. *ApJ*, 431: 617–624, August 1994.

J. Dubinski and R. G. Carlberg. The structure of cold dark matter halos. *ApJ*, 378:496–503, September 1991.

A. S. Eddington. The distribution of stars in globular clusters. *MNRAS*, 76:572–585, May 1916.

G. Efstathiou, M. Davis, S. D. M. White, and C. S. Frenk. Numerical techniques for large cosmological N-body simulations. *ApJS*, 57:241–260, February 1985.

G. Efstathiou, C. S. Frenk, S. D. M. White, and M. Davis. Gravitational clustering from scale-free initial conditions. *MNRAS*, 235:715–748, December 1988.

1. Esa. The Hipparcos and Tycho Catalogues (ESA 1997). *VizieR Online Data Catalog*, 1239:0–+, February 1997.

S. M. Faber and J. S. Gallagher. Masses and mass-to-light ratios of galaxies. *Ann. Rev. Astron. & Astrophys.*, 17:135–187, 1979.

J. A. Fillmore. Observable properties of oblate spheroids. *AJ*, 91:1096–1107, May 1986.

C. B. Foltz, P. C. Hewett, R. L. Webster, and G. F. Lewis. The central velocity dispersion of the lensing galaxy in the quadruple lens system Q2237 + 0305. *ApJL*, 386:L43–L45, February 1992.

M. Fukugita, C. J. Hogan, and P. J. E. Peebles. The Cosmic Baryon Budget. *ApJ*, 503:518–+, August 1998.

M. Fukugita and E. L. Turner. Gravitational lensing frequencies - Galaxy cross-sections and selection effects. *MNRAS*, 253:99–106, November 1991.

S. Ghigna, B. Moore, F. Governato, G. Lake, T. Quinn, and J. Stadel. Density Profiles and Substructure of Dark Matter Halos: Converging Results at Ultra-High Numerical Resolution. *ApJ*, 544:616–628, dec 2000.

R. Giovanelli, M. P. Haynes, L. N. da Costa, W. Freudling, J. J. Salzer, and G. Wegner. The Tully-Fisher Relation and H 0. *ApJL*, 477:L1+, March 1997.

A. J. S. Hamilton, P. Kumar, E. Lu, and A. Matthews. Reconstructing the primordial spectrum of fluctuations of the universe from the observed nonlinear clustering of galaxies. *ApJL*, 374:L1–L4, June 1991.

E. Hayashi, J. F. Navarro, A. Jenkins, C. S. Frenk, Power, S. D. M. White, V. Springel, J. Stadel, C. Quinn, T. R., and J. Wadsley. Disk Galaxy Rotation Curves in Triaxial CDM Halos. *astro-ph/0408132*, 2004a.

E. Hayashi, J. F. Navarro, C. Power, A. Jenkins, C. S. Frenk, S. D. M. White, V. Springel, J. Stadel, and T. R. Quinn. The inner structure of ΛCDM haloes - II. Halo mass profiles and low surface brightness galaxy rotation curves. *MNRAS*, 355:794–812, December 2004b.

E. Hayashi, J. F. Navarro, J. E. Taylor, J. Stadel, and T. Quinn. The Structural Evolution of Substructure. *ApJ*, 584:541–558, February 2003.

P. Hertel and W. Thirring. *Commun. Math. Phys.*, 24:22, 1971.

D. W. Hogg. Distance Measures in Cosmology. *astro-ph/9905116*, 1999.

J. Holmberg and C. Flynn. The local density of matter mapped by Hipparcos. *MNRAS*, 313:209–216, April 2000.

K. Huang. *Statistical Mechanics*, volume 2nd Ed. John Wiley & Sons, 1987.

J. Huchra, M. Gorenstein, S. Kent, I. Shapiro, G. Smith, E. Horine, and R. Perley. 2237 + 0305 - A new and unusual gravitational lens. *AJ*, 90: 691–696, May 1985.

A. Huss, B. Jain, and M. Steinmetz. How Universal Are the Density Profiles of Dark Halos? *ApJ*, 517:64–69, may 1999a.

A. Huss, B. Jain, and M. Steinmetz. The formation and evolution of clusters of galaxies in different cosmogonies. *MNRAS*, 308:1011–1031, October 1999b.

R. Ibata, G. F. Lewis, M. Irwin, E. Totten, and T. Quinn. Great Circle Tidal Streams: Evidence for a Nearly Spherical Massive Dark Halo around the Milky Way. *ApJ*, 551:294–311, April 2001.

N. Inada and M. Oguri. The discovery of the largest separation gravitationally lensed quasar. *Astronomical Herald*, 97:415–424, July 2004.

M. J. Irwin, R. L. Webster, P. C. Hewett, R. T. Corrigan, and R. I. Jedrzejewski. Photometric variations in the Q2237 + 0305 system - First detection of a microlensing event. *AJ*, 98:1989–1994, December 1989.

I. Ispolatov and E. G. D. Cohen. Phase transitions in systems with $1/r^{\alpha}$ attractive interactions. *Phys. Rev. E*, 64(5):056103–+, nov 2001.

N. Katz. Dissipationless collapse in an expanding universe. *ApJ*, 368:325–336, February 1991.

C. R. Keeton. A Catalog of Mass Models for Gravitational Lensing. *astro-ph/0102341*, 2001.

R. C. Kennicutt. The integrated spectra of nearby galaxies - General properties and emission-line spectra. *ApJ*, 388:310–327, April 1992.

S. M. Kent and E. E. Falco. A model for the gravitational lens system 2237+0305. *AJ*, 96:1570–1574, November 1988.

A. Klypin, A. V. Kravtsov, O. Valenzuela, and F. Prada. Where Are the Missing Galactic Satellites? *ApJ*, 522:82–92, sep 1999.

C. S. Kochanek. The Saas Fee Lectures on Strong Gravitational Lensing. *astro-ph/0407232*, 2004.

C. S. Kochanek, P. Schneider, and J. Wambsganss. *The Saas Fee Lectures on Strong Gravitational Lensing*. Springer-Verlag: Berlin, 2004.

L. V. E. Koopmans and T. Treu. The Stellar Velocity Dispersion of the Lens Galaxy in MG 2016+112 at z=1.004. *ApJL*, 568:L5–L8, March 2002.

L. V. E. Koopmans, T. Treu, C. D. Fassnacht, R. D. Blandford, and G. Surpi. The Hubble Constant from the Gravitational Lens B1608+656. *ApJ*, 599: 70–85, 2003.

R. Kormann, P. Schneider, and M. Bartelmann. Isothermal elliptical gravitational lens models. *Astron. & Astrophys.*, 284:285–299, April 1994.

T. Kranz, A. Slyz, and H.-W. Rix. The Submaximal Disk of NGC 4254. In *ASP Conf. Ser. 230: Galaxy Disks and Disk Galaxies*, pages 559–560, 2001.

M. Kregel. Structure and Kinematics of Edge-on Galaxy Disks. *PhD Thesis, Rijksuniversiteit Groningen*, 2003.

M. López-Corredoira, A. Cabrera-Lavers, O. E. Gerhard, and F. Garzón. Evidence for a deficit of young and old stars in the Milky Way inner in-plane disc. *Astron. & Astrophys.*, 421:953–967, July 2004.

C. G. Lacey. The influence of massive gas clouds on stellar velocity dispersions in galactic discs. *MNRAS*, 208:687–707, June 1984.

J. Lehar, G. I. Langston, A. Silber, C. R. Lawrence, and B. F. Burke. A gravitationally-lensed ring in MG 1549 + 3047. *AJ*, 105:847–852, March 1993.

G. F. Lewis, M. J. Irwin, P. C. Hewett, and C. B. Foltz. Microlensing-induced spectral variability in Q 2237+0305. *MNRAS*, 295:573–+, April 1998.

G. B. Lima Neto, D. Gerbal, and I. Márquez. The specific entropy of elliptical galaxies: an explanation for profile-shape distance indicators? *MNRAS*, 309:481–495, October 1999.

L. Lindegren and M. A. C. Perryman. GAIA: Global astrometric interferometer for astrophysics. *Astron. & Astrophys. Suppl. Ser.*, 116:579–595, May 1996.

E. L. Lokas, G. A. Mamon, and F. Prada. Dark matter distribution in the Draco dwarf from velocity moments. *astro-ph/0411694*, 2004.

D. Lynden-Bell and P. P. Eggleton. On the consequences of the gravothermal catastrophe. *MNRAS*, 191:483–498, may 1980.

D. Lynden-Bell and R. Wood. The gravo-thermal catastrophe in isothermal spheres and the onset of red-giant structure for stellar systems. *MNRAS*, 138:495–+, 1968.

S. R. Majewski, M. F. Skrutskie, M. D. Weinberg, and J. C. Ostheimer. A Two Micron All Sky Survey View of the Sagittarius Dwarf Galaxy. I. Morphology of the Sagittarius Core and Tidal Arms. *ApJ*, 599:1082–1115, December 2003.

A. H. Maller, L. Simard, P. Guhathakurta, J. Hjorth, A. O. Jaunsen, R. A. Flores, and J. R. Primack. Breaking the Disk/Halo Degeneracy with Gravitational Lensing. *ApJ*, 533:194–202, April 2000.

R. A. Mendez and R. Guzman. Starcounts in the flanking fields of the Hubble Deep Field. The faint end of the disc stellar luminosity function and its scale-height. *Astron. & Astrophys.*, 333:106–116, May 1998.

J. Miralda-Escude. The correlation function of galaxy ellipticities produced by gravitational lensing. *ApJ*, 380:1–8, October 1991.

H. J. Mo, S. Mao, and S. D. M. White. The formation of galactic discs. *MNRAS*, 295:319–336, apr 1998.

B. Moore, S. Ghigna, F. Governato, G. Lake, T. Quinn, J. Stadel, and P. Tozzi. Dark Matter Substructure within Galactic Halos. *ApJL*, 524: L19–L22, oct 1999a.

B. Moore, F. Governato, T. Quinn, J. Stadel, and G. Lake. Resolving the Structure of Cold Dark Matter Halos. *ApJL*, 499:L5+, may 1998.

B. Moore, T. Quinn, F. Governato, J. Stadel, and G. Lake. Cold collapse and the core catastrophe. *MNRAS*, 310:1147–1152, dec 1999b.

J. A. Muñoz, C. S. Kochanek, and C. R. Keeton. Cusped Mass Models of Gravitational Lenses. *ApJ*, 558:657–665, September 2001.

W. A. Mulder. Dynamical friction on extended objects. *Astron. & Astrophys.*, 117:9–16, January 1983.

R. Narayan and M. Bartelmann. Gravitational lensing. In *Formation of Structure in the Universe*, pages 360–+, 1999.

J. F. Navarro and W. Benz. Dynamics of cooling gas in galactic dark halos. *ApJ*, 380:320–329, oct 1991.

J. F. Navarro, C. S. Frenk, and S. D. M. White. The Structure of Cold Dark Matter Halos. *ApJ*, 462:563–+, may 1996.

J. F. Navarro, C. S. Frenk, and S. D. M. White. A Universal Density Profile from Hierarchical Clustering. *ApJ*, 490:493–+, December 1997.

J. F. Navarro, E. Hayashi, C. Power, A. R. Jenkins, C. S. Frenk, S. D. M. White, V. Springel, J. Stadel, and T. R. Quinn. The inner structure of ΛCDM haloes - III. Universality and asymptotic slopes. *MNRAS*, 349: 1039–1051, April 2004.

T. Padmanabhan. Statistical mechanics of gravitating systems. *Phys. Rep.*, 188:285–362, April 1990.

T. Padmanabhan. Statistical Mechanics of Gravitating Systems in Static and Cosmological Backgrounds. *Lecture Notes in Physics, Berlin Springer Verlag*, 602:165–207, 2002.

T. Padmanabhan and S. Engineer. Nonlinear Gravitational Clustering: Dreams of a Paradigm. *ApJ*, 493:509–+, January 1998.

P. J. E. Peebles. Large-scale background temperature and mass fluctuations due to scale-invariant primeval perturbations. *ApJL*, 263:L1–L5, December 1982.

P. J. E. Peebles. Dark matter and the origin of galaxies and globular star clusters. *ApJ*, 277:470–477, February 1984.

W. H. Press, S. A. Teukolsky, W. T. Vetterling, and B. P. Flannery. *Numerical recipes in C. The art of scientific computing.* Cambridge: University Press, —c1992, 2nd ed., 1992.

J. Primack. The origin and distribution of angular momentum in galaxies. *astro-ph/0312547*, 2003.

R. Racine. Fifth image and photometric variability in 2237 + 0305 ('Einstein Cross'). *AJ*, 102:454–460, August 1991.

M. Rauch, W. L. W. Sargent, T. A. Barlow, and R. A. Simcoe. Small-Scale Structure at High Redshift. IV. Low-Ionization Gas Intersecting Three Lines of Sight to Q2237+0305. *ApJ*, 576:45–60, September 2002.

D. Reed, F. Governato, L. Verde, J. Gardner, T. Quinn, J. Stadel, D. Merritt, and G. Lake. Evolution of the Density Profiles of Dark Matter Haloes. *astro-ph/0312544*, 2003.

H. Rix, D. P. Schneider, and J. N. Bahcall. Hubble Space Telescope Wide Field Camera imaging of the gravitational lens 2237 + 0305. *AJ*, 104: 959–967, September 1992.

V. Rubin, J. Burley, A. Kiasatpoor, B. Klock, G. Pease, E. Rutscheidt, and C. Smith. Galactic Space Motions of O-B5 Stars within 3 KPC of the Sun. *AJ*, 67:281–+, June 1962.

V. C. Rubin, N. Thonnard, and W. K. Ford. Extended rotation curves of high-luminosity spiral galaxies. IV - Systematic dynamical properties, SA through SC. *ApJL*, 225:L107–L111, November 1978.

P. D. Sackett. Does the Milky Way Have a Maximal Disk? *ApJ*, 483:103–+, July 1997.

P. Salucci. The constant-density region of the dark haloes of spiral galaxies. *MNRAS*, 320:L1–L5, January 2001.

P. Salucci and A. Burkert. Dark Matter Scaling Relations. *ApJL*, 537: L9–L12, July 2000.

D. J. Sand, T. Treu, G. P. Smith, and R. S. Ellis. The Dark Matter Distribution in the Central Regions of Galaxy Clusters: Implications for Cold Dark Matter. *ApJ*, 604:88–107, March 2004.

R. Schmidt, R. L. Webster, and G. F. Lewis. Weighing a galaxy bar in the lens Q2237 + 0305. *MNRAS*, 295:488–+, April 1998.

R. W. Schmidt. The Effect of the Bar in the Gravitational Lens System 2237+0305. *Masters Thesis*, pages 2–+, 1996.

D. P. Schneider, E. L. Turner, J. E. Gunn, J. N. Hewitt, M. Schmidt, and C. R. Lawrence. Erratum: High-Resolution CCD Imaging and Derived Gravitational Lens Models of 2237+0305 (A.J. 95, 1619 (1988). *AJ*, 96: 1755–+, November 1988.

P. Schneider, J. Ehlers, and E. E. Falco. *Gravitational Lenses*. Gravitational Lenses, XIV, 560 pp. 112 figs.. Springer-Verlag Berlin Heidelberg New York. Also Astronomy and Astrophysics Library, 1992.

J. A. Sellwood. Bar instability and rotation curves. *Astron. & Astrophys.*, 99:362–374, June 1981.

J. A. Sellwood. Bars and Dark Matter Halo Cores. *ApJ*, 587:638–648, April 2003.

J. L. Sérsic. *Atlas de galaxias australes*. Cordoba, Argentina: Observatorio Astronomico, 1968, 1968.

J. Shen and J. A. Sellwood. The Destruction of Bars by Central Mass Concentrations. *ApJ*, 604:614–631, April 2004.

J. D. Simon, A. D. Bolatto, A. Leroy, and L. Blitz. High-Resolution Measurements of the Dark Matter Halo of NGC 2976: Evidence for a Shallow Density Profile. *ApJ*, 596:957–981, October 2003.

C. Sire and P. Chavanis. Thermodynamics and collapse of self-gravitating Brownian particles in D dimensions. *Phys. Rev. E*, 66(4):046133–+, October 2002.

N. Slonim, R. Somerville, N. Tishby, and O. Lahav. Objective classification of galaxy spectra using the information bottleneck method. *MNRAS*, 323: 270–284, May 2001.

J. Sommer-Larsen and A. Dolgov. Formation of Disk Galaxies: Warm Dark Matter and the Angular Momentum Problem. *ApJ*, 551:608–623, April 2001.

W. B. Sparks, C. M. Carollo, and F. Macchetto. Detection of Neutral Gas in the Central Galaxy of the Centaurus Cluster. *ApJ*, 486:253–+, September 1997.

D. N. Spergel and P. J. Steinhardt. Observational Evidence for Self-Interacting Cold Dark Matter. *Physical Review Letters*, 84:3760–3763, April 2000.

R. J. Splinter, A. L. Melott, S. F. Shandarin, and Y. Suto. Fundamental Discreteness Limitations of Cosmological N-Body Clustering Simulations. *ApJ*, 497:38–+, April 1998.

V. Springel, S. D. M. White, G. Tormen, and G. Kauffmann. Populating a cluster of galaxies - I. Results at [formmu2]z=0. *MNRAS*, 328:726–750, December 2001.

K. Subramanian and S. A. Cowling. On local conditions for multiple imaging by bounded, smooth gravitational lenses. *MNRAS*, 219:333–346, March 1986.

R. A. Swaters, B. F. Madore, F. C. van den Bosch, and M. Balcells. The Central Mass Distribution in Dwarf and Low Surface Brightness Galaxies. *ApJ*, 583:732–751, February 2003.

D. Syer, S. Mao, and H. J. Mo. Global stability and the mass-to-light ratio of galactic disks. In *Dynamics of Galaxies and Galactic Nuclei, An International Workshop of the SFB 328 "Evolution of Galaxies" held at the ITA November 03 - 05, 1997, Editors: Wolfgang J. Duschl and Christian Einsel, p. 103.*, pages 103–+, July 1998.

J. E. Taylor and A. Babul. The Dynamics of Sinking Satellites around Disk Galaxies: A Poor Man's Alternative to High-Resolution Numerical Simulations. *ApJ*, 559:716–735, October 2001.

R. J. Thacker and H. M. P. Couchman. Star Formation, Supernova Feedback, and the Angular Momentum Problem in Numerical Cold Dark Matter Cosmogony: Halfway There? *ApJL*, 555:L17–L20, July 2001.

A. Toomre. Theories of spiral structure. *Ann. Rev. Astron. & Astrophys.*, 15:437–478, 1977.

S. Tremaine, D. O. Richstone, Y. Byun, A. Dressler, S. M. Faber, C. Grillmair, J. Kormendy, and T. R. Lauer. A family of models for spherical stellar systems. *AJ*, 107:634–644, February 1994.

T. Treu and L. V. E. Koopmans. The internal structure of the lens PG1115+080: breaking degeneracies in the value of the Hubble constant. *MNRAS*, 337:L6–L10, December 2002.

C. M. Trott and A. Melatos. Collapsed and Extended Cold Dark Matter Halos in Softened N-Body Gravity. *ApJ*, 618:38–45, January 2005.

C. M. Trott and R. L. Webster. Dissecting a galaxy: mass distribution of 2237+0305. *MNRAS*, 334:621–630, August 2002.

C. M. Trott and R. L. Webster. Determining the Properties of Galaxy 2237+0305 using Gravitational Lensing. In *IAU Symposium*, pages 109–+, July 2004.

R. B. Tully and J. R. Fisher. A new method of determining distances to galaxies. *Astron. & Astrophys.*, 54:661–673, February 1977.

J. A. Tyson, R. A. Wenk, and F. Valdes. Detection of systematic gravitational lens galaxy image alignments - Mapping dark matter in galaxy clusters. *ApJL*, 349:L1–L4, January 1990.

T. S. van Albada. Dissipationless galaxy formation and the R to the 1/4-power law. *MNRAS*, 201:939–955, December 1982.

R. P. van der Marel. Velocity Profiles of Galaxies with Claimed Black-Holes - Part Three - Observations and Models for M87. *MNRAS*, 270:271–+, September 1994.

E. van Kampen. Overmerging in N-body simulations. *astro-ph/0002027*, 2000.

M. Vitvitska, A. A. Klypin, A. V. Kravtsov, R. H. Wechsler, J. R. Primack, and J. S. Bullock. The Origin of Angular Momentum in Dark Matter Halos. *ApJ*, 581:799–809, December 2002.

J. Wambsganss and B. Paczynski. Parameter degeneracy in models of the quadruple lens system Q2237+0305. *AJ*, 108:1156–1162, October 1994.

J. Wambsganss, P. Schneider, and B. Paczynski. Interpretation of the microlensing event in QSO 2237 + 0305. *ApJL*, 358:L33–L36, August 1990.

R. B. Wayth, M. O'Dowd, and R. L. Webster. A microlensing measurement of the size of the Broad-Line Region in the lensed QSO 2237+0305. *MNRAS, submitted*, 2004a.

R. B. Wayth, S. J. Warren, G. F. Lewis, and P. C. Hewett. The Lens and Source of the Optical Einstein Ring Gravitational Lens ER 0047-2808. *MNRAS, submitted*, 2004b.

M. D. Weinberg and N. Katz. Bar-driven Dark Halo Evolution: A Resolution of the Cusp-Core Controversy. *ApJ*, 580:627–633, December 2002.

B. J. Weiner, J. A. Sellwood, and T. B. Williams. The Disk and Dark Halo Mass of the Barred Galaxy NGC 4123. II. Fluid-Dynamical Models. *ApJ*, 546:931–951, January 2001.

S. D. M. White, C. S. Frenk, M. Davis, and G. Efstathiou. Clusters, filaments, and voids in a universe dominated by cold dark matter. *ApJ*, 313: 505–516, February 1987.

R. Wielen. The diffusion of stellar orbits derived from the observed age-dependence of the velocity dispersion. *Astron. & Astrophys.*, 60:263–275, September 1977.

R. A. Windhorst, D. Burstein, D. F. Mathis, L. W. Neuschaefer, F. Bertola, L. M. Buson, D. C. Koo, K. Matthews, P. D. Barthel, and K. C. Chambers. The discovery of a young radio galaxy at Z = 2.390 - Probing initial star formation at Z less than approximately 3.0. *ApJ*, 380:362–383, October 1991.

H. J. Witt and S. Mao. Probing the structure of lensing galaxies with quadruple lenses: the effect of 'external' shear. *MNRAS*, 291:211–218, October 1997.

O. Wucknitz. Degeneracies and scaling relations in general power-law models for gravitational lenses. *MNRAS*, 332:951–961, June 2002.

J. S. B. Wyithe. The shallow slope of the $z \sim 6$ quasar luminosity function: limits from the lack of multiple-image gravitational lenses. *MNRAS*, 351: 1266–1276, July 2004.

J. S. B. Wyithe, E. Agol, and C. J. Fluke. The size of the mid-IR emission region of a quasar inferred from microlensed images of Q2237+0305. *MNRAS*, 331:1041–1052, April 2002.

H. K. C. Yee. High-resolution imaging of the gravitational lens system candidate 2237+030. *AJ*, 95:1331–1339, May 1988.

A. R. Zentner and J. S. Bullock. Halo Substructure and the Power Spectrum. *ApJ*, 598:49–72, November 2003.

APPENDIX A

Gauss-Hermite Pixel Fitting

The Gauss-Hermite Pixel Fitting software is introduced and the mathematical framework underpinning it presented. The procedures for preparing the stellar templates and galaxy spectra are discussed and the parameters chosen in the fitting are explained and justified.

A.1 Gauss-Hermite Pixel Fitting Software

To compare the absorption lines in the galaxy spectra with appropriately broadened and shifted lines in the stellar template spectra, careful and accurate characterisation of the line profiles and reliable continuum subtraction are required, with this aim in mind. The mathematical approach taken by van der Marel (1994) and implemented in his Gauss-Hermite Pixel Fitting Software will be summarised.

A model for the galaxy spectrum is constructed as a sum of the broadened and shifted stellar template, and a continuum background. The continuum is characterised by Legendre polynomials, and the velocity profiles of the absorption lines by a Gauss-Hermite series (of which the Gaussian is the first order solution). These choices of functional forms characterise the galaxy spectra with sufficient accuracy. A χ^2 statistic is used to quantify the difference between the model and observed galaxy spectra, as a function of the number of free parameters such as the velocity dispersion and velocity offset.

If $G(x)$ and $S(x)$ are the galaxy and stellar template spectra, respectively, as a function of logarithmic wavelength ($x = \ln \lambda$), a model galaxy spectrum can be written as,

$$G_{\rm model}(x) = a \left\{ [B \circ S_\gamma](x) + \sum_{l=1}^{L} b_l P_l(x) \right\}, \tag{A.1}$$

where $\circ$ denotes a convolution, $P_l(x)$ are Legendre polynomials, and γ is called the 'line strength',

$$S_\gamma(x) \equiv \gamma S(x) + (1 - \gamma), \tag{A.2}$$

and allows for different equivalent widths of the galaxy and stellar spectra.

The form of B, the broadening function that includes the Gauss-Hermite series, will now be described. The velocity profile is expanded as a Gauss-Hermite series, where the first order solution is a Gaussian profile, and higher order terms introduce non-Gaussianity, such as flattening or steepening of the line peak. This expansion can be expressed as,

$$B(x) = B(v/c) = \frac{c}{\sigma}\alpha(w)\left[1 + \sum_{j=3}^{N} h_j H_j(w)\right], \tag{A.3}$$

where

$$w \equiv (v - V)/\sigma, \tag{A.4}$$

$$\alpha(w) = \frac{1}{\sqrt{2\pi}} \exp\left(-w^2/2\right), \tag{A.5}$$

contain the velocity shift, V, and the velocity dispersion, σ. Here, $\alpha(w)$ is a Gaussian and $H_j(w)$ are the Hermite polynomials. The software minimises over these parameters for the coefficients h_3–h_6 ($N = 6$), and for v and σ.

A.2 Software Functions

There are several additional steps that need to be undertaken to compare the galaxy with stellar template spectra. Firstly, the template spectra need to be smeared and chopped to have the same resolution (Å/pixel, observations were made with differing slit widths as shown in Table 3.1) and size as the galaxy spectra. The procedure **preptemp** then broadens the template spectra to a user-specified range of velocity dispersions, producing a two dimensional file.

The galaxy spectra are prepared with the procedure **prepgal**, which has a number of roles. The spatial scale of the spectrum is assigned (row number corresponding to galactic radius) and the user is prompted for the range of radii (rows) to be used in the fitting. Similarly, the procedure rebins the spectrum spatially to meet a user-defined signal-to-noise ratio, or bin width. A mask file is constructed containing the wavelength range to be used in fitting, and the location of any bad pixels. The sky spectrum is averaged and placed in the first row of the galaxy spectrum to remove any strong sky lines that were incompletely subtracted during the initial data reduction. The procedure prompts for a 2D noise spectrum, so as the noise can be evaluated independently at each pixel (these noise values are used in the final χ^2 calculation). The noise map is calculated as the variance,

$$v = \left(\sum_{i=1}^{2} |f_i|^2 + |s_i|^2 + \mathrm{rn} \right)^{1/2} \tag{A.6}$$

where f_i and s_i are the flux and sky maps for each image (as discussed above, two observations were taken for each of the major and minor axes), and rn denotes the readnoise. In these observations, rn = 2.3 e^-/pixel, however the Poisson noise of the signal and sky maps far exceed this value.

The final fitting procedure, **pixfitgau**, takes the output of the two preparatory programs and iteratively performs the χ^2 minimisation over parameters. The user specifies the maximum order of Legendre polynomials for continuum fitting, and the procedure outputs the best-fitting velocity offset and velocity dispersion, with their uncertainties, at each radial bin, and the χ^2. This procedure fits only Gaussian profiles to the absorption lines. Gauss-Hermite expansion can be used subsequently for more accurate results, if required. The Gauss-Hermite series will not be used because line shapes are not required, and a basic kinematic analysis is desired.

Hence, there are a number of user specified parameters that can be varied to find the best solution — the wavelength range, Legendre polynomial order, choice of stellar template, signal-to-noise or size of radial bins.

A.3 Spectral Templates

The stellar templates comprise eight stellar types, ranging from G0III to K5III — red giant stars that contribute the majority of the light in early-type galactic components. A small slit width ($0.3''$) was used for the stellar observations to maximise spectral resolution so that they could be used for many different slit widths.

For these spectra to be compared correctly with the galactic spectra, they need to be Gaussian smeared to the galactic spectra resolution. The quoted resolution of the ESI instrument in Echelle mode is $\sigma = 11.89\mathrm{kms}^{-1}$ (slit width = $0.3''$) and $36.1\mathrm{kms}^{-1}$ ($\Delta x = 1.25''$). The IRAF task **gauss** is used to smear the stellar template to the correct resolution by convolving the spectra with a Gaussian distribution. Since the convolution of two Gaussian distributions with variances σ_1^2 and σ_2^2 gives $\sigma^2 = \sigma_1^2 + \sigma_2^2$, the template needs to be smeared by $(36.1^2 - 11.89^2)^{1/2} = 34.09\mathrm{kms}^{-1}$, which corresponds to $34.09\mathrm{kms}^{-1}/11.4\mathrm{kms}^{-1}\mathrm{pixel}^{-1} = 2.9$ pixels. After smearing, the templates

were redshifted to coincide with the previously measured recessional velocity of the galaxy. This ensures the correct shift of each wavelength, although is not critical for a low redshift system such as 2237+0305 (z=0.039 used). The spectra were then truncated to contain the same number of pixels and wavelength range as the galactic spectra. Templates were prepared to compare with Orders 5 and 6, which include the absorption features Mgb, FeI and Nad — of interest for my analysis.

The templates for Orders 5 and 6 are now ready to be prepared by **preptemp**. Both orders were prepared such that the velocity dispersions will be trialed over the range $\sigma = 40 - 900\text{kms}^{-1}$ with $\Delta\sigma = 5\text{kms}^{-1}$. This is an arbitrarily large range as the measurements of Foltz et al. (1992) found a central dispersion of $\sigma = 215 \pm 30\text{kms}^{-1}$, however it is useful to ensure the software is working correctly. The resolution, $\Delta\sigma = 5\text{kms}^{-1}$, was chosen to be accurate enough for the expected uncertainties in the dispersion ($\sim$10s kms^{-1}). Figure A.1 shows a surface representation of an output two dimensional stellar template. As the broadening dispersion is increased from 40kms^{-1} to 900 kms^{-1}, the spectral features are smoothed out, and the spectrum becomes mostly featureless. The velocity dispersion of the galaxy lies somewhere in this range.

A.4 Preparation of the Galaxy Spectrum

The galaxy spectra are prepared similarly. The central rows (22–100) are chosen to be fitted (outer rows show no signal) corresponding to $r = [-6.7, 6.1]''$ where the central row (68) is estimated using the peak in the spectra. Increasing the radial range is found to have little effect on the results, since the signal-to-noise ratio reduces beyond $r\sim3''$.

The two orders contain incompletely subtracted sky lines which need to be taken into account in the fitting. In my case, the best approach for this is to restrict the wavelength range of the fitting routine to include the absorption features, but exclude the bad pixels. Conversely, choosing too narrow a range can lead to larger errors in the results (it is important there is enough information for the continuum to be properly characterised). For both orders, a median range has been chosen and is shown in Figure A.2. The ranges encompass the main absorption features and the surrounding continua.

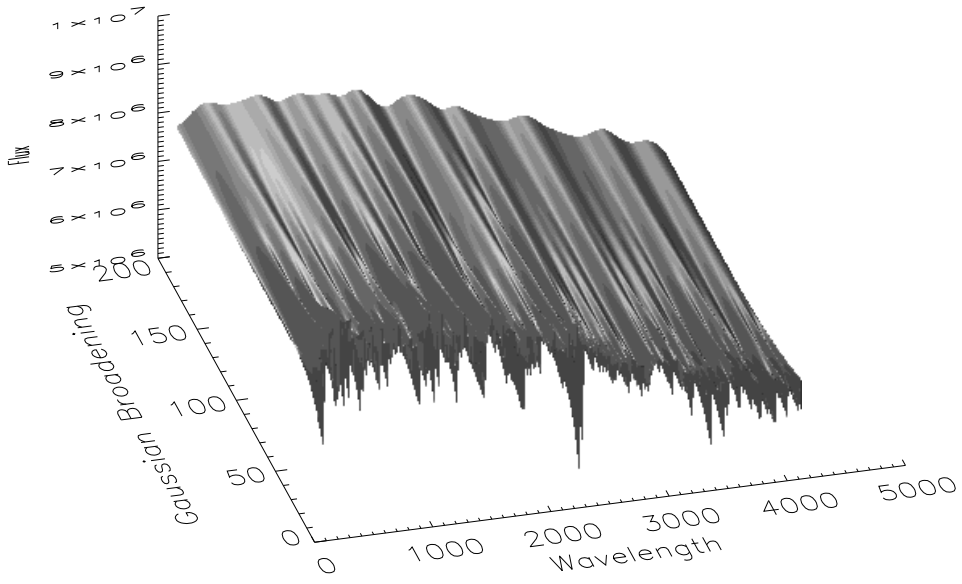

Figure A.1: Surface representation of the smeared, two dimensional stellar template spectrum. As the Gaussian Broadening dispersion is increased (y-axis), the spectral features are smoothed out.

Finally, the radial rows were rebinned to meet a minimum signal-to-noise ratio of 5. This figure is varied later for comparison, but the dynamical results are found to be robust to its variance.

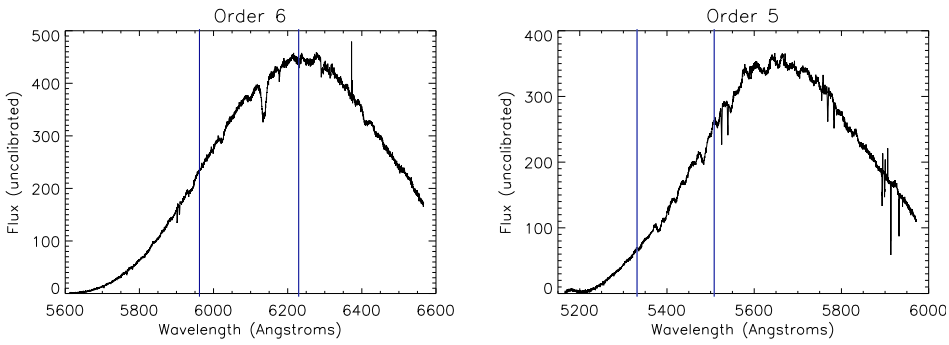

Figure A.2: Wavelength range chosen for each order for velocity dispersion fitting. The choice allows for the range around the absorption features, but omits regions with inaccurate sky subtraction.

APPENDIX B

Anisotropic Line-of-Sight Velocity Dispersion

The two-dimensional integral, Equation (4.12), can be reduced to a one-dimensional numerical integral by changing the order of integration and performing the integration over r,

$$\begin{aligned}\sigma^2_{\rm los}(R) &= \frac{2G}{\Upsilon I(R)} \int_R^\infty \frac{r^{1-2\beta_a}}{\sqrt{r^2-R^2}} \qquad (B.1)\\ &\quad \times \left(1-\beta_a \frac{R^2}{r^2}\right) \int_r^\infty x^{2\beta_a-2} \rho(x) M(x)\, dx dr \\ &= \frac{2G}{\Upsilon I(R)} \int_R^\infty x^{2\beta_a-2} \rho(x) M(x) \int_R^x \frac{r^{1-2\beta_a}}{\sqrt{r^2-R^2}} \qquad (B.2)\\ &\quad \times \left(1-\beta_a \frac{R^2}{r^2}\right) dr dx.\end{aligned}$$

The inner integral with respect to r can be calculated as a hypergeometric function,

$$\begin{aligned}&\int_R^x \frac{r^{1-2\beta_a}}{\sqrt{r^2-R^2}}\, dr - \beta_a R^2 \int_R^x \frac{r^{-1-2\beta_a}}{\sqrt{r^2-R^2}}\, dr \qquad (B.3)\\ = &\int_0^x \frac{r^{1-2\beta_a}}{\sqrt{r^2-R^2}}\, dr - \int_0^R \frac{r^{1-2\beta_a}}{\sqrt{r^2-R^2}}\, dr + \beta_a R^2 \int_0^R \frac{r^{-1-2\beta_a}}{\sqrt{r^2-R^2}}\, dr \\ &-\beta_a R^2 \int_0^x \frac{r^{-1-2\beta_a}}{\sqrt{r^2-R^2}}\, dr. \qquad (B.4)\end{aligned}$$

The integral representation of the hypergeometric function is given by,

$$ {}_2F_1(a,b;c;z) = \frac{\Gamma(c)}{\Gamma(b)\Gamma(c-b)} \int_0^1 \frac{t^{b-1}(1-t)^{c-b-1}}{(1-tz)^a}\, dt, \tag{B.5} $$

where Γ is the Gamma Function. Making the following substitutions in Equation (B.1),

$$ r = 1/\sqrt{t}, \qquad dr = -dt/2t^{3/2}, \tag{B.6} $$

the expression (B.4) becomes,

$$ \begin{aligned} & - \frac{1}{2}\int_0^{1/x^2} \frac{t^{\beta_a-3/2}}{(1-tR^2)^{1/2}}\, dt + \frac{1}{2}\int_0^{1/R^2} \frac{t^{\beta_a-3/2}}{(1-tR^2)^{1/2}}\, dt \\ & + \frac{\beta_a R^2}{2}\int_0^{1/x^2} \frac{t^{\beta_a-1/2}}{(1-tR^2)^{1/2}}\, dt - \frac{\beta_a R^2}{2}\int_0^{1/R^2} \frac{t^{\beta_a-1/2}}{(1-tR^2)^{1/2}}\, dt \\ = & - \frac{x^{1-2\beta_a}}{2}\int_0^1 \frac{s^{\beta_a-3/2}}{(1-sR^2/x^2)^{1/2}}\, ds + \frac{R^{1-2\beta_a}}{2}\int_0^1 \frac{s^{\beta_a-3/2}}{(1-s)^{1/2}}\, ds \\ & + \frac{\beta_a R^2 x^{-1-2\beta_a}}{2}\int_0^1 \frac{s^{\beta_a-1/2}}{(1-sR^2/x^2)^{1/2}}\, ds - \frac{\beta_a R^2 R^{-1-2\beta_a}}{2}\int_0^1 \frac{s^{\beta_a-1/2}}{(1-s)^{1/2}}\, ds \end{aligned} \tag{B.7} $$

where the upper integration limits have been scaled to unity in the second equality. Identifying the parameters in the integrands with those in the hypergeometric function, (B.5), the line-of-sight velocity dispersion for arbitrary constant β_a can be written as,

$$ \begin{aligned} \sigma^2_{\rm los}(R) = \frac{G}{\Upsilon I(R)} \int_R^\infty & x^{2\beta_a-2}\rho(x)M(x)\times \\ & \frac{\Gamma(\beta_a-1/2)}{\Gamma(\beta_a+1/2)}\left[R^{1-2\beta_a}\,{}_2F_1\left(\frac{1}{2},\beta_a-\frac{1}{2};\beta_a+\frac{1}{2};1\right)\right] \\ & - \frac{\Gamma(\beta_a-1/2)}{\Gamma(\beta_a+1/2)}\left[x^{1-2\beta_a}\,{}_2F_1\left(\frac{1}{2},\beta_a-\frac{1}{2};\beta_a+\frac{1}{2};\frac{R^2}{x^2}\right)\right] \\ & + \beta_a R^2\frac{\Gamma(\beta_a+1/2)}{\Gamma(\beta_a+3/2)}\left[x^{-2\beta_a-1}\,{}_2F_1\left(\frac{1}{2},\beta_a+\frac{1}{2};\beta_a+\frac{3}{2};\frac{R^2}{x^2}\right)\right] \\ & - \beta_a R^2\frac{\Gamma(\beta_a+1/2)}{\Gamma(\beta_a+3/2)}\left[R^{-2\beta_a-1}\,{}_2F_1\left(\frac{1}{2},\beta_a+\frac{1}{2};\beta_a+\frac{3}{2};1\right)\right] dx. \end{aligned} \tag{B.8} $$

One can see from the powers of x and R in β_a that the result is dimensionally consistent. To verify this result, we can input $\beta_a = 0$ (isotropy), to recover

the isotropic solution;

$$\sigma^2_{\rm los}(R,\beta_a=0) = \frac{G}{\Upsilon I(R)}\int_R^\infty x^{-2}\rho(x)M(x) \tag{B.9}$$
$$\times \quad \frac{\Gamma(-1/2)}{\Gamma(1/2)}\left(R\,{}_2F_1\left(\frac{1}{2},-\frac{1}{2};\frac{1}{2};1\right) - x\,{}_2F_1\left(\frac{1}{2},-\frac{1}{2};\frac{1}{2};\frac{R^2}{x^2}\right)\right)\,dx$$
$$= \quad \frac{G}{\Upsilon I(R)}\int_R^\infty x^{-2}\rho(x)M(x)(-2)\left(0 - x\sqrt{1-\frac{R^2}{x^2}}\right)\,dx$$
$$= \quad \frac{2G}{\Upsilon I(R)}\int_R^\infty x^{-2}\rho(x)M(x)\sqrt{x^2-R^2}\,dx,$$

where we have used the following identities of the hypergeometric function,

$${}_2F_1(a,b;c;z) = (1-z)^{c-a-b}\,{}_2F_1(c-a,c-b;c;z), \tag{B.10}$$
$${}_2F_1(a,b;c;1) = \frac{\Gamma(c)\Gamma(c-a-b)}{\Gamma(c-a)\Gamma(c-b)}, \tag{B.11}$$
$$a=1/2, \quad b=-1/2, \quad c=1/2, \tag{B.12}$$

and which returns the isotropic solution (Tremaine et al. 1994).